Characterisation of Small, Close-Approaching Near-Earth Asteroids

Petro Janse van Rensburg
(JNSPET016)

South African Astronomical Observatory
Cape Town
South Africa

Thesis presented for the partial fulfillment of the requirements for the degree of Master of Science (MSc) in Astrophysics and Space Science

Department of Astronomy
University of Cape Town

Supervisors: Dr. Nicolas Erasmus and Prof. Matthew A. Bershady

March 2021

Abstract

Near-Earth Asteroids (NEAs) are a population of asteroids in a steady state, constantly being replenished with asteroids from the main belt. NEAs have orbits that come close to or cross the Earth's orbit and therefore some could have impacting trajectories and pose a threat. Small NEAs (diameter $< 300\,\mathrm{m}$) pose a greater threat compared to large NEAs because they are more abundant and can cause significant damage on impact. The characteristics of small NEAs can give an indication of the most likely properties of potential future impactors. Even though in recent years the number of discovery and characterisation programmes of NEAs have increased, the characterisation of the small NEA population still lags behind because they can only be observed with 1-m class telescopes when they pass close to the Earth and become bright enough.

Presented here in this MSc thesis are 20 NEAs that were successfully observed and characterised with the South African Astronomical Observatory (SAAO) 40-inch telescope and the Sutherland High-Speed Optical Camera. Out of the 20 NEAs, 14 had diameters $< 300\,\mathrm{m}$ ($\mathrm{H} > 21$). Characterisation involved assigning taxonomic probabilities to each NEA based on spectra from the Bus-DeMeo classification scheme and thereby inferring its most probable composition, as well as using a Lomb-Scargle periodogram to extract the rotation period from multi-band photometry. The taxonomic probabilities were determined with the colours $\mathrm{g}'-\mathrm{r}'$ and $\mathrm{r}'-\mathrm{i}'$, in combination with a machine learning (ML) algorithm trained on synthetic colours from observed spectra obtained from literature. The taxonomies considered were the S-, C-, and X-complexes, and the D-, Q-, and V-types.

In this thesis, the taxonomic probabilities are reported for all of the targets. A distinct taxonomic class was assigned to 15 NEAs that had a probability >50% in a specific taxonomy. New taxonomic classes are reported for 11 of the targets. A notable result of this study is the confirmation of the prediction that the most common meteorite, ordinary chondrites, are due to S-complex *and* Q-type asteroids. The fraction of meteorite falls due to ordinary chondrites are similar to the combined fraction of S-complex and Q-type asteroids in this study (∼80%). This confirmation was only possible by including the Q-type asteroids in the classification and being able to differentiate between the C-complex and Q-type asteroids with two colours and a ML approach. A rotation period was extracted for nine NEAs that were observed for long enough to resolve a light curve period. The remaining targets had only partial or flat light curves and no period could be resolved from the periodogram. Reported here are also three small NEAs with $\mathrm{H} > 22$ magnitude which were found to have rotation periods smaller than the 2.2 hour spin barrier and could be rigid pieces of rock instead of rubble piles.

Acknowledgements

I would like to acknowledge the funders of this project: the National Research Foundation (NRF) and the University of Cape Town (UCT). The funding from the NRF was provided through the National Astrophysics and Space Science Programme (NASSP) and the South African Astronomical Observatory (SAAO). The funding from UCT was provided through the Myer Levinson (EMDIN) Scholar award.

A special note of thanks to my supervisors, Dr. Nicolas Erasmus and Prof. Matthew Bershady. Thank you for the opportunity to pursue a research project in this field, especially because of the limited research on asteroids in South Africa. Thank you for the constant support, help and encouragement.

The observations in this project would not have been possible without training from Nic to observe with the SAAO 40-inch telescope and the Sutherland High-Speed Optical Camera. Thank you also to PhD student Anja Genade and Dr. Amanda Sickafoose for their help with the early observations, as well as the continuous support from Dr. Stephen Potter and the SAAO telescope support staff during the observations (especially the remote ones).

I would also like to express my gratitude towards the developer of the photometry pipeline used in this project, Dr. Michael Mommert. Thank you for guiding me through adding transformation equations into the pipeline. Thank you also to Iriwaan Simon from the SAAO IT department who helped me to install and execute the pipeline in a Docker container and to S. Navarro-Meza for providing the classified spectra used as training data in the machine learning algorithm.

Thank you to the UCT Astronomy Department and the SAAO for the provision of a "writing circle", administrated by Prof. Kate le Roux. Thank you to Prof. le Roux and my fellow writing circle students for all of the feedback on my writing, I greatly appreciate it. To my fellow UCT and SAAO students, thank you for the conversations, help and laughter during the completion of this thesis. Lastly, thank you to my family for their constant love, support and encouragement.

Plagiarism Declaration

I know that plagiarism is wrong. Plagiarism is to use someone else's work as one's own. This thesis represents my own work and contributions from the works of others have been acknowledged, cited and referenced.

Petro Janse van Rensburg
March 2021

Table of Contents

1 | Introduction

Our Solar System formed approximately 4.6 billion years ago (Bouvier and Wadhwa, 2010). In the current known structure, the Sun is at the centre and the eight planets and millions of other objects are in orbit around it. These other objects include, but are not limited to, dwarf planets, asteroids, comets and centaurs. The four small, terrestrial planets (Mercury, Venus, Earth and Mars) orbit the Sun in the inner region of the Solar System and the four giant planets (Jupiter, Saturn, Uranus and Neptune) orbit in the outer region. Between the orbits of Mars and Jupiter, at a distance between ∼2 AU and ∼4 AU from the Sun, is the main asteroid belt which contains more than 90% of the asteroids already discovered. To date, there are more than 900 000 Main-Belt Asteroids or MBAs. Closer to the Earth, over 24 000 of the known asteroids are located in orbits that come near or cross the Earth's orbit and are called Near-Earth Asteroids or NEAs.

Because of their close proximity, NEAs are Solar System objects that can interact directly and affect life on Earth both positively and negatively. The Earth has been subject to impacts from NEAs since the very beginning of its existence. Some theories suggest that in the first billion years of Earth's existence, NEAs and comets delivered ingredients like carbon and water that could have initiated life on Earth (e.g., Morbidelli et al., 2000; Bancelin et al., 2017). Even though NEAs could have provided the building blocks out of which life formed, they were also responsible for destroying multiple early life forms, including dinosaurs (Alvarez et al., 1980). More than 90% of asteroids this size (> 1 km in diameter) that could cause global destruction have already been discovered and are only predicted to impact the Earth once every few million years (Stokes et al., 2017). Small NEAs (< 1 km in diameter) pose a greater immediate threat to Earth because they are more abundant and statistically impact the Earth more frequently, compared to large NEAs, based on a power-law distribution of frequency versus size (Perna et al., 2015; Stokes et al., 2017). The majority (>95%) of NEAs already discovered have diameters < 1 km. These NEAs can still cause significant local or regional damage. This was seen in the recent Chelyabinsk event when a ∼20 m NEA exploded in the atmosphere near Chelyabinsk, Russia, causing damage to buildings and injuring many people (Brown et al., 2013). Asteroids of this size impact the Earth once every few hundred years (Stokes et al., 2017).

Since small NEAs can also pose a threat to life on Earth, a current goal is to discover 90% of asteroids larger than 140 m in diameter (Stokes et al., 2017). In particular, the discovery of NEAs with estimated diameters < 300 m has increased significantly in the last decade with the use of discovery programs such as the Catalina Sky Survey[1], the Panoramic Survey Telescope and Rapid Response System[2] (Pan-STARRS; Flewelling et al., 2020) and the Asteroid Terrestrial-impact Last Alert Sys-

[1] https://catalina.lpl.arizona.edu/
[2] https://panstarrs.stsci.edu/

tem[3] (ATLAS; Tonry et al., 2018). Even though more small NEAs are being discovered, the physical properties of these asteroids are still not well studied. Physical properties include, for example, the rotation period and the taxonomic type. In the past, most detailed studies focused on NEAs with diameters larger than 1 km because these asteroids are bright enough to study with Earth-based telescopes even when they are several AU from the Earth. Small asteroids only become bright enough to study with ground-based observations near or at their close-approach date. This means they can only be studied for a few days or weeks before they move away from the Earth and cannot be observed again for many months or even years. For this reason, the characterisation rate of small NEAs lags behind the discovery rate. Characterisation of small NEAs has only increased in recent years with studies such as Mommert et al. (2016), Erasmus et al. (2017), Perna et al. (2018) and Navarro-Meza et al. (2019), but the characteristics of the small NEA population can still be better refined.

Knowing the characteristics of NEAs are especially important in models that evaluate what will happen if an NEA is on a collision course with the Earth. This was shown in recent studies by Perna et al. (2015), Stokes et al. (2017), Mathias et al. (2017) and Reddy et al. (2019) which assessed atmospheric entry, impact risk, as well as mitigation strategies. Studying the characteristics of the small NEA population as a whole can give an indication of the most likely properties of a potential future impactor and therefore mitigation techniques can be developed appropriate for these asteroids. In a more detailed study, Reddy et al. (2019) performed a planetary defense exercise where they tracked, characterised and modelled an impact risk assessment for a $\sim$10 m hypothetical potential impactor (2012 TC4). This is a real NEA that made a close approach to the Earth in 2017 at a distance of only 0.13 lunar distances (LD), but the study hypothetically assumed that it was on a collision course with the Earth. Reddy et al. (2019) showed that the size and composition of a potential impactor can be used to estimate the impact zone size. In the case of a small impactor, the respective area could be evacuated, but in the case of a large impactor, a deflection technique might also be attempted. The composition and rotation period could make one technique more effective than another.

NEAs are not only potential impactors, they can also provide valuable information into the formation of the Solar System. Asteroids are thought to be the remnants of planetary formation. Knowing the compositional distribution of asteroids in the main-belt can help us understand the processes involved when the Solar System formed billions of years ago. NEAs can provide valuable information into the Solar System formation models since they have been ejected from the main asteroid belt and come close enough to the Earth to study with ground-based telescopes. The most accepted models suggest that the NEA population is in a steady state. NEAs have short dynamical lifetimes of only a few million years before they collide with the Sun, a planet or are ejected from the Solar System (Bottke et al., 2002), but the population is constantly being replenished from asteroids in the main belt. MBAs are heated by the Sun and as they re-radiate the heat away, a small thrust results in them slowly moving closer or further from the Sun. This is known as the Yarkovsky effect (Vokrouhlický et al., 2015). As the MBAs move in semi-major axis, they experience resonant forces with planets like Jupiter and Saturn which transport them into near-Earth orbits (Morbidelli and Vokrouhlický, 2003; Granvik et al., 2017).

There are multiple models aiming to understand how the Solar System formed and evolved to how we observe it today. In some Solar System formation models, it is suggested that MBAs formed near

[3] https://atlas.fallingstar.com/

where they are currently situated (e.g., Gradie and Tedesco, 1982). Other models such as the Nice model (e.g., Morbidelli et al., 2005, 2007) and the Grand Tack model (Walsh et al., 2011) suggest that the asteroids formed in a primordial asteroid belt further away from its current location and were displaced into the current main asteroid belt region after planetary migration of Jupiter and Saturn. There is also a discrepancy between the observed compositional distribution of asteroids in the main belt and the results of the models. Understanding the compositional structure of asteroids in the main belt can provide valuable information into refining these Solar System formation models (Demeo and Carry, 2014).

The close proximity of NEAs also make them attractive objects to visit with spacecraft for space mining attempts or to study scientifically. If the missions are timed correctly, NEAs can be reached with far less fuel expenditure compared to other Solar System bodies which is important if one wants profit from the mining of NEAs. It is speculated that these asteroids contain valuable elements such as water, platinum and gold (Elvis, 2012). Knowing the physical properties of mission-accessible close-approaching NEAs is vital for target selection, success, and feasibility of these missions. An example of a scientific mission is the National Aeronautics and Space Administration's (NASA's) OSIRIS-REx mission (Lauretta et al., 2017) which targeted the NEA 101955 Bennu (1999 RQ36). Bennu was chosen because it is thought to be an example of the very primitive asteroids that had a role in the Solar System formation, including the delivery of ingredients that could have initiated life on Earth. The spacecraft launched in 2016 to study the NEA in detail, including successfully collecting a sample from the surface on 20 October 2020. Bennu has a diameter of approximately 490 m and is considered a potentially hazardous asteroid because it has an Earth Minimum Orbit Intersection Distance (MOID) less than 0.05 AU (19.5 LD) and an absolute magnitude less than 22 magnitude. It has a rotation period of 4.3 hours and is also classified as a B-type asteroid which means it is mostly carbon-based. These properties were determined from ground-based observations and confirmed with the space mission results (Lauretta et al., 2019).

This MSc thesis describes the observation and characterisation of 14 small (diameter < 300 m) and 6 large (diameter > 300 m) known or newly discovered NEAs during their close approach to the Earth using a 1-m class telescope at the South African Astronomical Observatory (SAAO). Characterisation includes extracting the rotation period as well as assigning taxonomic probabilities to the NEA based on spectra from the Bus-DeMeo classification scheme (DeMeo et al., 2009) and multi-band photometry. The results of this study are compared to and combined with results from other NEA surveys to provide valuable information into Solar System formation models, as well as the most likely properties of potential future impactors and mission-accessible targets.

The rest of this chapter includes a discussion on important asteroid terminology, background on the orbital classes of NEAs, as well as a discussion on the taxonomy and rotational properties of NEAs. In Chapter 2 the details of the observations, photometric extraction and data analysis are described. This includes how taxonomic probabilities were assigned to the targets based on spectra from the Bus-DeMeo classification scheme and the method of searching for rotation periods. The light curves, taxonomy and rotation periods are shown and discussed in Chapter 3 and the thesis is concluded in Chapter 4.

1.1 Terminology

Most asteroids have an irregular shape, but their size (diameter; d) can be estimated from the absolute magnitude (H) and an assumed visual geometric albedo (p_V) following equation 1.1 (Harris and Harris, 1997).

$$d = \frac{1329}{\sqrt{p_V}} 10^{-\mathrm{H}/5} \tag{1.1}$$

The absolute magnitude is the magnitude of an asteroid if it was hypothetically placed at 1 AU from the Sun and the Earth and at zero phase angle. The visual geometric albedo refers to the ratio of the visual brightness of an object at zero phase angle with respect to the brightness of a hypothetical disk that reflects all light and scatters it equally in all directions.

In this project, the diameter of the NEAs were obtained from NASA's Jet Propulsion Laboratory (JPL) Center for Near-Earth Object Studies (CNEOS)[4]. It is given as a diameter-range, calculated by using the measured absolute magnitude and estimated albedo values of 0.25 and 0.05.

1.2 Orbital classes of NEAs

NEAs were defined by Shoemaker et al. (1979) and are situated at a perihelion distance $q < 1.3$ AU. The perihelion distance is the distance at which the asteroid is closest to the Sun in its orbit and is given by $q = a(1 - e)$, where a is the semi-major axis and e the eccentricity of the orbit. Similarly, the aphelion distance (Q) is the distance at which the asteroid is furthest from the Sun and is given by $Q = a(1 + e)$. NEAs are also divided into four main orbital classes based on their semi-major axis, perihelion distance and aphelion distance:

- **Atiras** have orbits inside the Earth's orbit with $a < 1.0$ AU and $Q < 0.983$ AU.
- **Amors** have orbits completely outside of the Earth's orbit, with most of them crossing Mars' orbit. They are situated at $a > 1.0$ AU and $1.017 < q < 1.3$ AU.
- **Apollos** and **Atens** have orbits that cross the Earth's orbit. Apollos are situated at $a > 1.0$ AU and $q < 1.017$ AU and Atens are situated at $a < 1.0$ AU and $Q > 0.983$ AU.

At the time of writing, out of all the known NEAs, approximately 55% are Apollos, 37% are Amors, 7% are Atens and the remaining 1% are Atiras.

1.3 Taxonomic classes and the classification of NEAs

Asteroids consist of rock and regolith that reflect light from the Sun. The reflectance spectra of asteroids can be measured with Earth-based observations and it shows various broad absorption features indicative of the minerals present on the asteroid surface. The absorption features and shape of the continuum are used to divide asteroids into many different taxonomic classes. Instead of performing

[4] https://cneos.jpl.nasa.gov/

spectroscopy on moving targets, in some cases, photometry performed at a few key wavelengths using broadband filters is sufficient to differentiate between different taxonomic classes. This technique was also applied in this study.

There are various classification schemes that have been developed as new asteroid spectroscopy and photometry surveys have become available. The most popular early classification scheme was the Tholen taxonomy developed by Tholen (1984). It was based on reflectance photometry of 589 minor planets from the Eight-Color Asteroid Survey (ECAS; Zellner et al., 1985), spanning eight bands (0.34 to 1.04 μm), as well as albedo measurements. The Tholen taxonomy has 14 taxonomic classes, each indicated by a letter. The subsequent taxonomic schemes were all extensions of the Tholen classification.

The Bus taxonomy was developed by Bus and Binzel (2002) from more than 1000 reflectance spectra of MBAs in the Small Main-Belt Spectroscopic Survey (SMASS; Xu et al., 1995; Bus and Binzel, 2002). SMASS covered a wavelength range between approximately 0.4 μm and 1 μm. Bus extended the Tholen taxonomy to 26 classes by including classes that are a combination of two other classes. In 2009, DeMeo et al. extended the Bus taxonomy by including reflectance spectra in the infrared. This is referred to as the Bus-DeMeo classification scheme and is the scheme used in this project. The Bus-DeMeo taxonomy is based on reflectance spectra of 371 asteroids covering a wavelength range between 0.45 μm and 2.45 μm. These classification schemes have also been further developed by Carvano et al. (2010) and Demeo and Carry (2013) based on photometry of over 100 000 asteroids in the Sloan Digital Sky Survey Moving Object Catalog (SDSS, MOC; Ivezić et al., 2001). Photometry in the SDSS MOC includes the bands u′, g′, r′, i′ and z′, covering a wavelength range of 0.3 to 1.0 μm.

The Bus-DeMeo classification scheme is mainly divided into three complexes and 24 classes:

- S-complex which includes the classes S, Sa, Sq, Sr and Sv.
- C-complex which includes the classes C, Cb, Cg, Cgh and Ch.
- X-complex which includes the classes X, Xc, Xe and Xk.
- Other classes: A, B, D, K, L, O, Q, R, T and V.

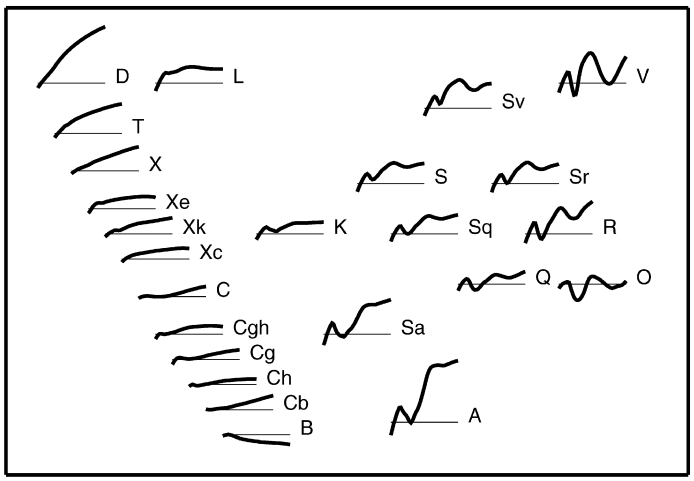

Figure 1.1: A key-chart from DeMeo et al. (2009) showing the average reflectance spectra of the 24 classes in the Bus-DeMeo classification scheme. The spectra span a wavelength range of 0.45 μm to 2.45 μm.

The average reflectance spectra of each class can be seen in Figure 1.1. In this project only the S-, C- and X-complexes, and D-, Q- and V-types were considered because these can be distinguished from one another by measuring the spectral slope in the visible wavelength range through broad-band photometry at several key wavelengths. S-complex, Q-type and V-type asteroids are all primarily defined by two absorption features at 1 μm and 2 μm corresponding to the rock-forming minerals olivine and pyroxene. Both olivine and pyroxene are silicate minerals and contain therefore silicon and oxygen, in combination with magnesium, iron or calcium.

V-type asteroids have stronger absorption features, compared to the features of S-complex or Q-type asteroids and the 1 μm feature is narrower. Q-type asteroids are considered "unweathered", and S-type asteroids as "weathered" Q-type asteroids, i.e., the surface of a Q-type asteroid has been changed due to, for example, the solar wind, cosmic rays or micrometeorite impacts (Binzel et al., 2015). Due to this space weathering, an S-complex spectrum has a redder slope compared to a Q-type spectrum and it also has weaker absorption features. C- and X-complex asteroids have very similar spectra with no strong absorption features. They are primarily only differentiated by the X-complex spectra having a slightly redder slope compared to the C-complex spectra. C-complex asteroids have been linked to carbonaceous chondrite meteorites, which means they are mostly made of carbon. X-complex asteroids are composed of a whole range of minerals including pyroxene, iron and organic-rich material. The spectra of D-type asteroids have a very red spectral slope, but their mineralogical makeup is still uncertain. It has been suggested that D-type asteroids are composed of organic-rich material (Gradie and Veverka, 1980) or silicates and carbon (Emery and Brown, 2004).

NEAs are mainly classified as S- or C-complex asteroids but X-complex, Q-, V- and D-type NEAs have also been observed. This result includes the small NEA population as has been seen in various studies such as Mommert et al. (2016), Carry et al. (2016), Erasmus et al. (2017), Ieva et al. (2018), Perna et al. (2018), Navarro-Meza et al. (2019) and Binzel et al. (2019). The majority of NEAs are classified as S-complex asteroids. Mommert et al. (2016) found that ∼45% of the asteroids in their sample belonged to the S-complex, independent of the size. Erasmus et al. (2017), Perna et al. (2018) and Navarro-Meza et al. (2019) all confirmed this result from data where most of the NEAs had an absolute magnitude less than 20 (corresponding to a diameter of less than ∼300 m using an assumed albedo of 0.2). Ieva et al. (2018) and Binzel et al. (2019) found slightly higher S-complex proportions of ∼60% and ∼50% respectively. In most of the studies, the C-complex and X-complex proportions are between 10% and 20%, except in the studies by Mommert et al. (2016) and Navarro-Meza et al. (2019) who listed ∼40% of their NEA populations as part of the C-complex. Mommert et al. (2016), Carry et al. (2016), Ieva et al. (2018), Perna et al. (2018) and Binzel et al. (2019) also included D- and V-type classifications in their study. In all of these studies, less than 10% of the NEA populations are classified as D- or V-type asteroids.

All of the taxonomic types that are observed in the NEA population agrees with the taxonomies observed in the inner main asteroid belt. This provides evidence for the models suggesting that NEAs originate from the inner main belt (Demeo and Carry, 2013, 2014; Carry et al., 2016). There is, however, a discrepancy between the amount of C-complex and Q-type asteroids observed in near-Earth orbits and in the inner main belt. C-complex asteroids are much more abundant in the main belt. The discrepancy in C-complex asteroids could be because of an observational bias favouring brighter, higher albedo asteroids (Binzel et al., 2015). Contrary to the C-complex asteroids, there are much more observed Q-type NEAs compared to MBAs (Binzel et al., 2015). Multiple studies found that ∼10% of their NEA populations are Q-type asteroids (Carry et al., 2016; Perna et al., 2018; Binzel et al., 2019). The discrepancy in Q-type asteroids could be because they have a fresh, unweathered surface, and Carry et al. (2016) and Binzel et al. (2019) showed that Q-type asteroids could have been resurfaced because of close encounters with the Earth and Venus. In addition, Q-type asteroids could also have been recently ejected from the main belt due to a collision and the Yarkovsky effect. Since they were recently ejected, they would not be significantly weathered.

The presence of Q-type asteroids in the NEA population also helped in the understanding of the discrepancy between the most observed NEAs (S-complex) and the most common meteorites (ordinary chondrites) (Binzel et al., 2015). S-complex NEAs comprise about half of the NEA population, but more than 80% of meteorite falls are ordinary chondrites (Wetherill and Chapman, 1988). In addition, the spectra of S-complex asteroids are redder compared to that of ordinary chondrites, but the spectra of Q-type asteroids, which have a fresh, resurfaced surface, agrees with ordinary chondrite spectra. Binzel et al. (2015) suggested that ordinary chondrites are not only due to Q-type asteroids, but also due to S-complex asteroids that are basically made of the same material as ordinary chondrites and Q-type asteroids, but they undergo space weathering.

1.4 Light curves and rotation periods

The light curve of a target shows the reflected sunlight (brightness) as a function of time. Asteroids will have different light curves depending on its shape and albedo. For example, a very extended object will have a light curve with a large amplitude as it rotates on its axis and sunlight reflects off of larger and smaller exposed areas. A more spherical object with a uniform surface albedo will have a relatively flat light curve. The light curve can also be used to extract the rotation period of the asteroid, which is the time it takes for an asteroid to rotate once on its axis. In addition, some asteroids are tumbling or some are gravitationally bound to another asteroid (i.e., binary).

The light curve amplitude can be an indication of how the albedo or surface varies and it can also be used to calculate the axial ratio (a/b). For an asteroid with a triaxial ellipsoid shape, the axial ratio can be calculated by using equation 1.2, where Δm is the amplitude (Burbine, 2017).

$$\frac{a}{b} = 10^{\Delta m/2.5\,\mathrm{mag}} \qquad (1.2)$$

Figure 1.2 shows the distribution of rotation period (or frequency) versus diameter of more than 8000 asteroids, including NEAs and MBAs, in the Asteroid Light Curve Database[5] (LCDB; Warner et al., 2009). A spin barrier at ~2.2 hours, which is explained by the assumption that most asteroids are rubble piles, can clearly be seen (Pravec and Harris, 2000). If the asteroid is a rubble pile and it spins faster than 2.2 hours, it will fly apart due to the outward centripetal

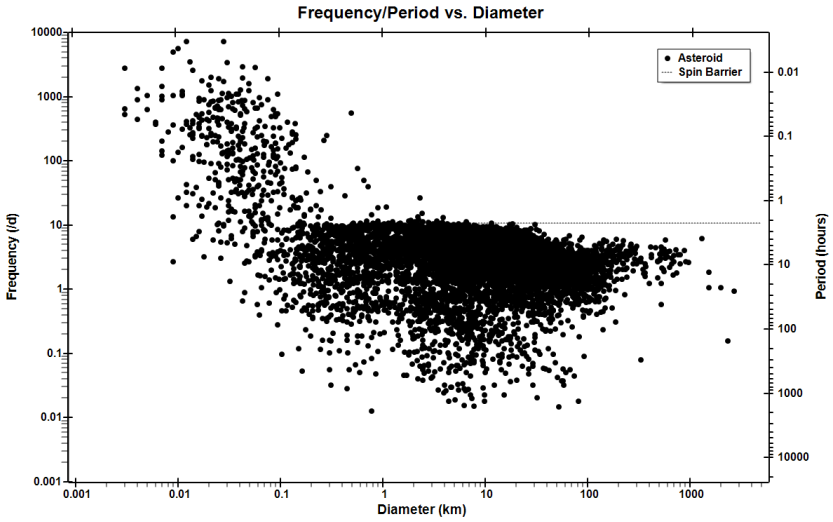

Figure 1.2: Shown is the rotation period (or frequency) as a function of diameter for over 8000 asteroids in the LCDB (Warner et al., 2009). The figure was obtained from the LCDB. A spin barrier can clearly be seen at around 2.2 hours. Asteroids with diameters $\lesssim$ 200 m mostly have rotation periods faster than the spin barrier.

[5] http://alcdef.org/

force. However, the plot also shows that some asteroids with diameters $\lesssim 200\,\mathrm{m}$ can have rotation periods faster than the spin barrier. These asteroids are probably not rubble piles but are rather rigid pieces of rock. Asteroids with diameters less than 300 m (the size range studied in this project) have rotation periods less than about 10 hours. This result was also confirmed by Thirouin et al. (2018) for objects in the Mission Accessible Near-Earth Object Survey (MANOS). All of the objects in MANOS had diameters less than 300 m. Very small NEAs with diameters of only a few tens of metres can be extremely rapidly rotating. Thirouin et al. (2018) found the fastest rotator: 2017 QG18, a $\sim$11 m Apollo NEA, with a rotation period of 11.9 seconds. Some small NEAs are also tumbling as discovered by both Warner et al. (2009) and Thirouin et al. (2018). Tumbling asteroids are asteroids with non-principal-axis (NPA) rotation which means they do not rotate around one of the principal axes. In general, these asteroids do not return to the same starting position after one rotation, but instead they rotate and precess around more than one axis (Harris, 1994; Pravec et al., 2005).

2 | Observational Methods and Data Analysis

2.1 Observing strategy and procedure

Observations for this project were performed with the SAAO 40-inch telescope and the Sutherland High-Speed Optical Camera (SHOC; Coppejans et al., 2013). The 40-inch telescope is located in Sutherland, South Africa, but does not require the observer to travel to Sutherland since it can also be remotely operated from Cape Town (or in principle from anywhere in the world). It has a primary mirror of 40 inches (101.6 cm) in diameter and a Cassegrain design with a focal-ratio of f/16.

The telescope has observing limits which is shown in Figure 2.1. The red regions indicate the positions on the sky where the telescope cannot observe. Importantly for this project are the declination (DEC) limits which are approximately 20° and −80°. This meant that only targets with declinations between 20° and −80° during their close approach to Earth could be observed. These limits, however, were also advantageous because many NEA characterisation and discovery programs that perform immediate follow-up observations are located in the northern hemisphere and are unlikely to be able to observe further south than −30°. For example, one of the targets (2019 CT4) had a DEC rate of -2716 arcsec/hour during its observations (see Table 2.1). If it was discovered in the northern hemisphere at 0°, it would already be at −36° within 2 days and immediate follow-up observations from the northern hemisphere would not be

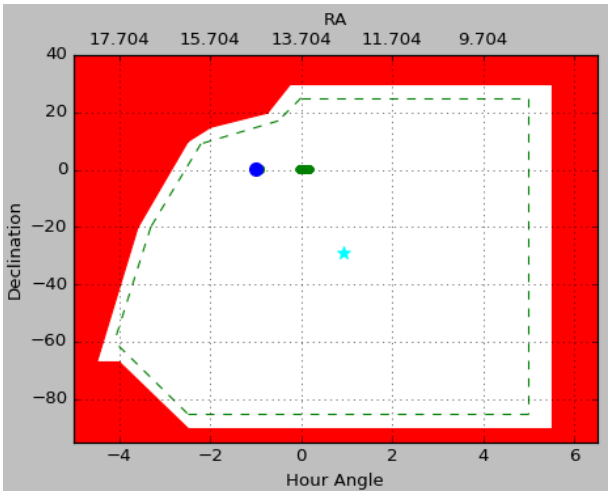

Figure 2.1: The observing limits of the 40-inch telescope[6], with Hour Angle on the horizontal axis and Declination (DEC) on the vertical axis. The Right Ascension (RA) is also shown on the horizontal axis, but since it is specific to the local sidereal time, the range is more important and not the actual values shown. The telescope cannot point to any position on the sky shown in red. The dashed lines show the pointing limits when the telescope is operated through the Telescope Control Software (TCS). A user can only point to positions in between the red and the dashed lines from the observing floor. While observing, the blue circle indicates the current position of the telescope, the green circles show the most recent movement of the telescope and the cyan star indicates the input co-ordinates in the TCS i.e., the co-ordinates the observer would like to point at next.

[6] https://topswiki.saao.ac.za/index.php/40%22_/_1.0m

possible. In addition, some NEAs are discovered when they are in the northern sky but only make their close approach and become bright enough to characterise a couple of days or weeks later, which by then some have moved to the southern sky. This means that this project would provide southern sky coverage for NEA characterisation.

The 40-inch telescope has a filter box with two filter wheels. The available filters are Bessel *U B V R I*, SDSS u′ g′ r′ i′ z′, Hα, O[III] and a clear filter. In this project, the SDSS g′-, r′- and i′-filter were used and their transmission curves are shown in Figure 2.2. Two instruments are available with the 40-inch telescope for photometric measurements: SAAO CCD Camera (STE3/STE4) and SHOC. These two instruments cannot be mounted at the same time and an instrumentation change is required to switch between the two camera systems. The instrument is mounted at the Cassegrain focus, below the filter box.

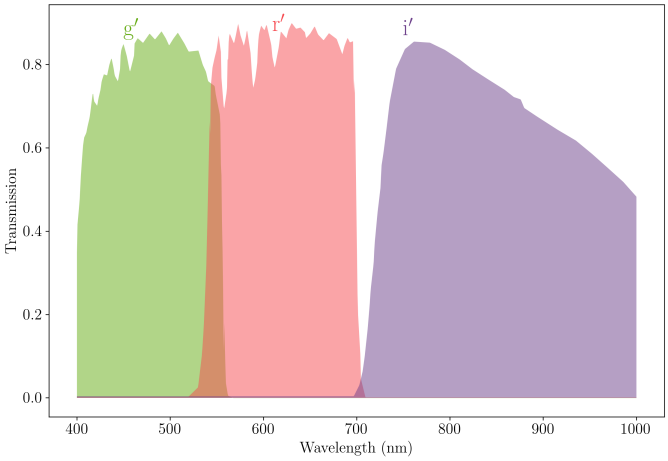

Figure 2.2: Shown are the transmission curves for the three SDSS filters on the 40-inch telescope. The transmission is shown in green for the g′-filter, red for the r′-filter and purple for the i′-filter. The quantum efficiency of SHOC (see Figure 2.3) is not included in the transmission.

There are two identical SHOC instruments[7]: SHOC 1 (or shocnawe) and SHOC 2 (or shocndisbelief) that can be mounted on either the SAAO 40-inch, 74-inch or the new 1-m telescope Lesedi. Each SHOC instrument consists of an Andor iXon camera, control computer, and Global Positioning System (GPS). With their high-speed photometry down to ∼100 ms resolution and accurately-triggered frames (via the GPS), the instruments were specifically commissioned for stellar occultation observations of centaurs or trans-Neptunian objects like Pluto (Coppejans et al., 2013). For example, the data from a stellar occultation with SHOC, in addition to 11 other stellar occultation data sets from other telescopes, were used to study the rings of the centaur (10199) Chariklo (Bérard et al., 2017). The SHOC instruments are also successfully used by astronomers for other transient science that require slower but still relatively fast ($\leq$ 10 s) time-resolved photometry, such as cataclysmic variables (e.g., Woudt

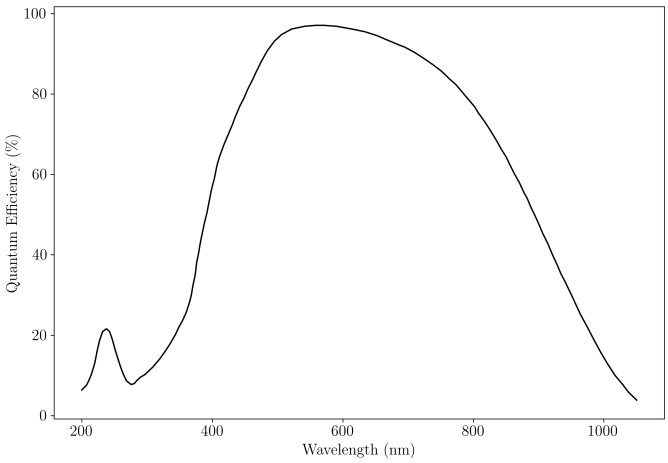

Figure 2.3: The quantum efficiency of the SHOC CCD as a function of the wavelength, obtained from the Andor iXon specification sheet[8].

[7] https://topswiki.saao.ac.za/index.php/SHOC
[8] https://shoc.saao.ac.za/Documents/Ixon.L888SS.pdf

et al., 2012; Paterson et al., 2019), as well as rapidly oscillating Ap stars (e.g., Holdsworth et al., 2019).

The CCD of SHOC has an imaging area of 1024×1024 pixels. On the 40-inch telescope, that corresponds to a field-of-view (FoV) of 2.85×2.85 arcmin^2 and a platescale of 0.167 arcsec/pixel for 1×1 binning. The quantum efficiency of the CCD is shown in Figure 2.3. The CCD can also be cooled to -70°C below ambient, by means of a combination of a thermo-electric cooler and fan-fed airflow, but by default is set to -50°C below ambient. This temperature results in a low dark current ($< 0.001\, e^-\text{pixel}^{-1}\text{s}^{-1}$). SHOC is controlled through a web-based graphical user interface (GUI), where the user can select filters, use GPS timing or adjust various camera settings. These settings include changing the exposure time, binning, read-out rate, preamplifier gain, as well as the number of images in a cube (kinetic series). The SHOC GUI also allows the user to automatically acquire data through scripting which, for example, allows a user to cycle filters continuously during an observation. This scripting feature was especially useful in this project where hundreds of exposures were taken during each target's observation, with a filter change after each exposure.

As explained in Chapter 1, small NEAs are usually only observable near or on their close approach to the Earth, i.e., when they are at their brightest. This MSc project initially started with a small pilot study to determine if the combination of the 40-inch telescope and SHOC was suitable to observe and characterise these NEAs. The success of the pilot study is discussed later in this section. Because these NEAs are only observable for a few days or weeks, target selection was also vital in this study. A new set of targets could be available to observe on every observation night, therefore target selection had to be performed at the beginning of each night. This is explained in more detail in Section 2.2.

Each target in this project, including the pilot study, was observed using the SDSS g′, r′ and i′ filters in the sequence r′-g′-r′-i′, using the scripting function on the SHOC web-based control software. This filter sequence was repeated multiple times for each target. Different filters were used so that the colours g′−r′ and r′−i′ could be calculated in order to determine the taxonomy of the targets. This is explained in more detail in Section 2.5. For all of the observations, the 1 MHz conventional mode of SHOC, with a preamplifier gain of 1.7 e^-/ADU were used, as well as 4×4 binning giving a plate scale of 0.668 arcsec/pixel.

If one observes objects that only move sidereally through the sky or if one has a large FoV, the best strategy would be to track the stars with the telescope so that they stay constant and asteroids move through the FoV. However, small NEAs are not only the brightest during their close approach to the Earth, they also have the fastest sky rates. Given this fast sky motion and the relatively small FoV of SHOC on the 40-inch, it was decided to use non-sidereal tracking and short exposure times such that the target remained a point source and roughly centred in the FoV during the observation period. The maximum exposure time before the stars will appear streaked was calculated through equation 2.1 by using the seeing and the rate that the target was moving through the sky (RA and DEC rates).

$$\text{Exposure time} = \frac{\text{seeing}}{\sqrt{(\text{RA rate})^2 + (\text{DEC rate})^2}} \tag{2.1}$$

The RA and DEC rates of each target during the observation period were obtained from NASA's JPL Horizons service[9]. The rates, in addition to the RA and DEC, at the observation mid-time, are shown in Table 2.1 . During the observations in this project the seeing was between 1" and 3". The exposure time of the targets ranged between 5 and 30 seconds and is shown in Table 2.1 for all of the observations. The non-sidereal tracking was implemented by adjusting the drive speeds of the telescope and the tracking direction. The RA and DEC rate for each target (in arcseconds/hour; see Table 2.1), converted to arcseconds/second, were used as the drive speeds. Figure 2.4 shows example frames of how this approach was successful in correctly tracking on the asteroids. The figure shows four 20 second exposures of 2013 DU in the r′-filter. This target had a visual (V) magnitude of 18.8 during the observations. In all of the observations, a signal-to-noise ratio (SNR) of at least 10 was required in a single exposure to extract reliable photometric measurements. This is explained further in Section 2.3. For this specific case, to achieve an SNR of 10, the exposure time had to be slightly larger than the exposure time calculated with equation 2.1. This resulted in the stars appearing slightly streaked, but this level of streaking was acceptable for the photometry extraction procedure in this project.

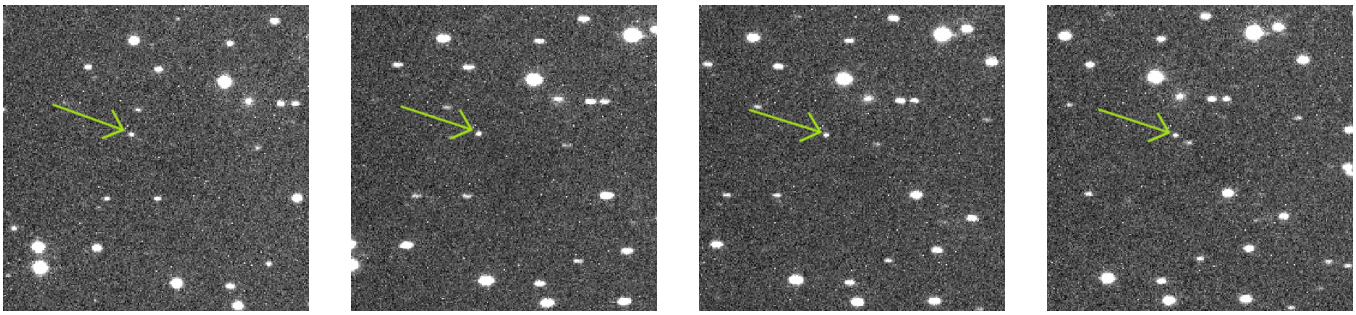

(a) (b) (c) (d)

Figure 2.4: Four exposures from the observations of 2013 DU in the r′-filter. The green arrow indicates the target, with the field stars moving to the left of the page from (a) to (d). The exposure time for each image was 20 seconds. The frames shown from (a) to (d) were *not* adjacent exposures; there is approximately 2 minutes between each frame, shown so that the movement is more obvious.

During the pilot study, eight small, fast-moving NEAs were successfully observed. The SNR for a 20-50 m object (the desired size range for this project) at 4 LD with a V magnitude of 17 was ∼10, i.e., sufficient for the photometry pipeline to locate the correct source and perform aperture photometry. The FoV of SHOC on the 40-inch was also sufficient that there were at least 10 reference stars in most frames for astrometric and photometric calibration (see Section 2.3). During the study it was also shown that the 40-inch could accommodate the non-sidereal rates of the targets via a "hidden" menu on the TCS and that the non-sidereal tracking was accurate enough such that the object did not streak, i.e., it stayed a point source within the seeing pixel during the exposure time. Finally, SHOC's high-speed photometric capabilities and scripting mode made it possible to take hundreds of exposures, with a filter change after each exposure, without the software or filter wheel failing.

After the successful pilot study, the project was expanded to this MSc project by applying for and being awarded subsequent telescope time during three trimesters: Trimester III of 2019 (October-December), Trimester I of 2020 (January-April) and Trimester II of 2020 (May-August). The average

[9] https://ssd.jpl.nasa.gov/?horizons

time awarded per trimester was 13 nights. The NEAs were observed on or within a median of 3 days (minimum of 1 day and maximum of 46 days) of their close-approach date, as reported in Table 2.1. Additionally, seven NEAs were also observed within a median of 11 days (minimum of 4 days and maximum of 39 days) of their discovery date.

In total, 14 small NEAs (diameter $< 300\,\mathrm{m}$) and 6 NEAs with diameters larger than 300 m were observed on a total of 25 nights between September 2018 and May 2020. Two of the 25 nights were performed at the telescope in Sutherland while the remaining nights were performed remotely from the SAAO facilities in Cape Town. A summary of all the observations is given in Table 2.1, including the observation length of all the targets. The weather and a sparse FoV played a role in five NEAs being observed for less than 2 hours. However, 15 NEAs were observed for longer than 2 hours, of which seven were observed on two consecutive nights.

To verify the methodology used and to validate the results of the NEA study reported in this thesis, seven large and well-studied MBAs were also observed between October 2019 and May 2020 on a total of 4 nights, as reported in Table 2.1. They were primarily observed for colour information and therefore did not require long observation periods. MBAs can be observed and characterised similarly to NEAs. Target selection for well-studied MBAs is much easier because there are more than 900 000 known MBAs versus only approximately 24 000 known NEAs. The observed MBAs were large (diameter $> 1\,\mathrm{km}$), had published rotation and composition (taxonomy) information, and they had well-known sky positions and slow sky rates. This meant they were bright and could be observed with long exposure times, resulting in a high SNR and quality photometry collected for these validating MBA observations.

The data were reduced by performing basic CCD reductions. A cube of 100 bias frames were taken during every observation at close to zero exposure time (0.28395 seconds) with the dome and camera shutter closed. A cube of 10 sky flat frames were also obtained at exposure times of 2 and 5 seconds in three filters (r', g' and i') at every observation, either after sunset or before sunrise if there were no clouds. During these observations, the telescope was pointed to the zenith and tracking was turned off. The same binning and preamplifier settings as the target observations were used for both the bias frames and flat fields. Since the dark current of SHOC is very small, no dark frames were taken.

To perform bias subtraction, the 100 bias frames were combined into an average "master bias" and subtracted from all of the science images as well as the sky flats. The flat frames were median-combined to form a normalised and bias-subtracted "master flat" for each filter. In the case where flats could not be taken on a specific night, the most recent, previously acquired flats were used. Finally, the science images were divided by the respective flats (i.e., flat-fielded) to obtain reduced images. All of the reductions were done by making use of Python, and Astropy's[10] (The Astropy Collaboration et al., 2013; Price-Whelan et al., 2018) `fits` module to read in the FITS files as 2D arrays. The subtractions, divisions and averaging of the arrays were performed with Python's `numpy`[11] module. Calibrated photometry was extracted from the reduced images. This is explained in Section 2.3.

[10] https://www.astropy.org/
[11] https://numpy.org/

Table 2.1: List of targets and observation details.

Target name	Orbit Type	H[a] (mag)	Diameter[b,c] (m)	CA distance (LD)[b]	CA date[b]	Discovery date[d]	Observation date(s)	Exp. time (seconds)	Obs. period (minutes)	RA[e] (deg)	DEC[e] (deg)	RA rate[e,f] (arcsec/hour)	DEC rate[e,g] (arcsec/hour)	Airmass[e]	V[e] (mag)
NEAs															
1620 Geographos (1951 RA)	Apollo, PHA	15.3	2300 - 5200	53.42	2019/8/31	1951/09/14	2019/10/16	10	50.72	319.14	4.11	85.15	37.06	1.25	15.74
86667 (2000 FO10)	Aten	17.6	800 - 1800	75.05	2019/03/03	2000/03/30	2019/03/04	10	154.17	81.60	-51.51	379.30	301.01	1.20	16.84
481394 (2006 SF6)	Aten, PHA	19.9	280 - 620	11.23	2019/11/21	2006/09/17	2019/11/18	5	34.22	25.96	-15.44	-756.63	-1018.43	1.11	14
2007 YU56	Amor	22.1	100 - 230	27.26	2019/01/05	2007/12/31	2019/01/14	20	120.90	89.93	-2.31	330.65	-298.67	1.21	18.41
358744 (2008 CR118)	Apollo, PHA	18.9	440 - 990	38.38	2018/08/28	2008/02/10	2018/09/03	10	42.85	288.19	-44.75	549.39	82.57	1.04	16.26
528159 (2008 HS3)	Amor, PHA	21.6	130 - 280	14.54	2019/05/09	2008/04/30	2019/05/02	10	66.17	217.33	-35.79	358.89	320.20	1	15.88
2010 AE30	Apollo	23.6	51 - 110	11.82	2020/01/17	2010/01/10	2020/01/15, 2020/01/16	10	75.47	88.60	-36.12	-871.72	-1696.89	1.02	18.27
454177 (2013 GJ35)	Amor	15.8	1800 - 4100	75.18	2019/01/14	2011/08/23	2019/01/19	10	118.98	116.98	-26.98	-230.19	-458.38	1.05	14.24
2013 CW32	Aten, PHA	22.0	110 - 240	13.86	2019/01/29	2013/02/05	2019/01/28, 2019/01/29	5	507.87	135.30	-32.03	-598.50	2120.32	1.05	16.65
2013 DU	Amor	24.0	42 - 94	14.84	2020/01/20	2013/02/17	2020/01/16	20	125.62	132.22	-22.63	687.41	-7.63	1.14	18.78
515767 (2015 JA2)	Apollo, PHA	21.1	160 - 360	24.65	2019/01/19	2015/04/14	2019/01/19	10	123.47	160.25	-17	-411.71	886.33	1.10	17.03
2019 AG7	Aten	25.5	21 - 47	3.92	2019/01/15	2019/01/09	2019/01/13, 2019/01/14	5	497.35	109.38	-5.65	-3094.54	-131.73	1.19	16.87
2019 CT4	Apollo	24.4	35 - 78	6.01	2019/03/02	2019/02/09	2019/03/02, 2019/03/03	5	562.78	128.38	-52.84	-1736.51	-2715.97	1.10	17.90
2019 EN	Apollo, PHA	21.2	150 - 340	9.69	2019/03/27	2019/03/02	2019/03/13	30	182.10	149.43	-24.87	-119.39	-106.54	1.07	18.15
2019 HV3	Aten	24.0	42 - 94	12.35	2019/05/04	2019/04/26	2019/05/02, 2019/05/03	5	313.93	187.76	-35.21	-1612.68	-89.75	1.02	18.08
2019 OM	Aten	22.6	80 - 180	21.09	2019/08/20	2019/07/24	2019/08/15, 2019/08/16	10	254.72	303.53	-22.18	-509.92	-494.11	1.14	17.60
2019 PZ2	Aten	19.8	290 - 650	24.86	2019/08/17	2019/08/13	2019/08/19	5	222.43	336.32	-20.14	-413.57	-1328.91	1.68	14.95
2019 SP3	Apollo	26.2	15 - 34	0.97	2019/10/03	2019/09/22	2019/10/01	5	282.65	315.96	-29.44	552.99	-1598.46	1.02	17.75
2020 BR10	Apollo	22.8	74 - 170	15.35	2020/02/23	2020/01/27	2020/02/17, 2020/02/18	20, 15	225.50	93.74	0.86	-930.09	47.05	1.20	18.62
2020 HT2	Amor	22.5	84 -190	26.30	2020/06/02	2020/04/21	2020/05/30	20	121.77	195.17	-49.92	-123.36	-588	1.05	18.57
MBAs															
141 Lumen (A875 AA)	MBA	8.5	117 916	-	-	1875/01/13	2020/05/30	10	64.75	237.96	-37.74	-32.93	10.53	1.01	12.81
175 Andromache (A877 TA)	MBA	8.4	94 532	-	-	1877/10/01	2020/05/30	10	49.63	223.54	-19.19	-25.72	6.48	1.04	13.26
270 Anahita (A887 TA)	MBA	8.8	54 100	-	-	1887/10/08	2020/03/06	10	22.77	237.55	-22	25.84	-6.23	1.10	13.07
329 Svea (A892 FG)	MBA	9.6	81 057	-	-	1892/03/21	2020/03/05	20	17.88	106.53	5.48	5.33	22.82	1.41	13.91
383 Janina (A894 BC)	MBA	9.9	43 500	-	-	1894/01/29	2019/10/16	10	33.80	304.09	-21.97	18.21	5.18	1.19	15.56
1273 Helma (1932 PF)	MBA	12.9	6278	-	-	1932/08/08	2020/03/05	20	36.78	207.79	-19.41	-11.66	-3.26	1.09	17.35
1933 Tinchen (1972 AC)	MBA	13	4508	-	-	1972/01/14	2020/03/05	20	35.78	239.48	-13.64	20.58	4.54	1.14	17.83

Notes:

[a] Absolute magnitude from https://ssd.jpl.nasa.gov/sbdb.cgi.

[b] Diameter range and close-approach (CA) distance and date of NEAs obtained from https://cneos.jpl.nasa.gov/ca/. Diameters of MBAs obtained from https://ssd.jpl.nasa.gov/sbdb.cgi.

[c] Diameter range calculated from equation 1.1 with geometric albedos of 0.25 and 0.05.

[d] Obtained from https://minorplanetcenter.net/.

[e] Obtained from https://ssd.jpl.nasa.gov/horizons.cgi at the observation mid-time.

[f] RA rate given as $d(\mathrm{RA})/dt \cos(\mathrm{DEC})$. It is multiplied by $\cos(\mathrm{DEC})$ to obtain a linear rate.

[g] DEC rate given as $d(\mathrm{DEC})/dt$.

2.2 Target selection

As explained in Chapter 1 and Section 2.1, small NEAs only become bright enough to observe with 1-m class telescopes during or at their close approach to the Earth. Often these small NEAs are also only discovered during the same close-approach. Luckily, new NEAs are discovered every day. The International Astronomical Union (IAU) Minor Planet Center's (MPC's)[12] database shows that more than 2 000 NEAs have already been discovered this year and more than 24 000 have already been discovered to date. This number is increasing, on average, by four per day. Most of these NEAs are small and only discovered weeks or even days before their close-approach date when they become bright enough for the discovery programs to detect them. Very few are also fully characterised before they move away from Earth and become too faint to observe. Therefore, unlike most observing strategies, the target selection for this study needed to be revised in the beginning of the night on every observation night in order to observe the best candidates.

At the beginning of the night, a list of all the NEAs that would make close approaches with the Earth was compiled. NASA's JPL CNEOS computes the orbit of all NEAs and also freely provides the close-approach distance, close-approach date, estimated diameter and absolute magnitude of all known NEAs that will make close approaches with the Earth. It also calculates whether any NEA will collide with the Earth for any future close approaches through the JPL Sentry System[13]. The CNEOS Application Program Interface[14] was queried to compile a list of NEAs (including the newly discovered ones) that would make a close approach within 30 LD of the Earth and within a window of 14 days of the allocated observation date. A window of 14 days and close-approach distance of 30 LD were used so that targets were observed when they are closest to the Earth and therefore the brightest.

After obtaining a list of targets that will make a close approach with the Earth within 14 days of the observation date, NASA's JPL Horizons service was used to determine if any of the targets will be observable from Sutherland with the 40-inch telescope and SHOC. The Horizons service was queried with Python's `astroquery` package[15] (Ginsburg et al., 2019). Unlike stars and galaxies which can be found at set coordinates (RA and DEC) and only move through the sky because of the Earth's movement, asteroids can be found at a different RA and DEC every hour, minute or sometimes second. The Horizons service provides the ephemerides of a target, given a specific observing location and date. In addition to the RA and DEC, it also gives information such as when the target rises and sets, the DEC and RA rates, airmass and V magnitude. Targets that were considered for observing included the following criteria:

- Observable for at least two hours to identify a rotation period.
- Within the observing limits of the telescope.
- Had an airmass of less than 1.3 at some point during the night.
- Had a V magnitude less than 19 to obtain an SNR ∼10 in a single exposure.

[12] https://minorplanetcenter.net/
[13] https://cneos.jpl.nasa.gov/sentry/
[14] https://ssd-api.jpl.nasa.gov/
[15] https://github.com/astropy/astroquery

- Were more south than $-20°$ to obtain southern sky coverage.

If several targets were observable, preference was given to the smallest object and/or to objects that were located at a declination below $-40°$. These targets were unlikely to be characterised by other NEA characterisation programs.

The target candidates were further filtered by discarding objects that required exposure times below 5 seconds (because of their sky rate). This was because it was unlikely to achieve an SNR of 10 for a $\sim$19 magnitude NEA with such a short exposure time. It would also possibly result in insufficient counts in the limited number of comparison stars to do proper photometric and astrometric calibration (see Section 2.3). A longer exposure time for such a fast moving target would also result in streaked sources and the photometry pipeline used for this project would not be able to extract reliable photometry.

The final step in deciding which targets would be observed was to look at the field that the target would move through using SIMBAD[16], using the RA and DEC from Horizons, to see how many stars there were in the FoV. There had be to at least 10 stars in the FoV with a magnitude greater than 19 so that photometric measurements could be extracted, which is described further in Section 2.3.

[16] http://simbad.u-strasbg.fr/simbad/

2.3 Photometric extraction

Photometric calibration was performed using PHOTOMETRYPIPELINE (PP)[17], an open-source and Python-based software package developed by Michael Mommert (2017) and available on PP's Github repository[18]. The pipeline was developed specifically for moving sources and is therefore primarily used for the extraction of photometry of asteroids, but it also has the ability to obtain photometric measurements of stationary sources like variable stars and extragalactic sources. The pipeline can be fed imaging data (FITS files) from small to medium-sized telescopes as input and returns calibrated photometry, with an accuracy of ≤ 0.05 magnitudes. It can in principle be used on imaging data from any telescope, provided the user creates a configuration file (examples, instructions and a template are provided by the developer). The configuration file is used by PP to translate header information from the telescope to PP-specific header keywords. PP is Mac and Linux compatible with a command line interface; Ubuntu 16.04 is the recommended and tested environment. In this project, the pipeline and all the required additional software were installed and executed through a Docker container. This made it possible to execute PP in a containerised Ubuntu 16.04 environment on any operating system.

PP consists of multiple executable Python scripts and requires the Python modules `numpy`, `scipy`[19], `astropy`, `astroquery`, `matplotlib`[20] (Hunter, 2007), `Python-Future`[21], `scikit-image`[22] (van der Walt et al., 2014) and `pandas`[23]. Each script has a specific function or process and can be called from the command line either individually, or automatically in sequence with the default input parameters through the command `pp_run`. In this project, the scripts were executed individually so that the input parameters could be adjusted to optimise the photometry extraction for each of the observations. Six commands were used to extract calibrated photometry: `pp_prepare`, `pp_register`, `pp_extract`, `pp_photometry`, `pp_calibrate` and `pp_distill`. For PP to successfully extract photometry, it requires that these commands be executed in this order.

The command `pp_prepare` prepares the FITS files for the subsequent processes by reading the existing FITS headers and adding new header keywords that are not telescope or instrument dependant (using the configuration file). Information like the instrument binning, filter, where the telescope was pointing during the observations and when the observations were performed, are copied to the new header keywords.

Image registration was performed with the command `pp_register` and requires SCAMP[24] (Bertin, 2006) to be installed on the system that PP runs from. This command first calls the process `pp_extract` to identify sources with Source Extractor[25] (Bertin and Arnouts, 1996), with a user-provided minimum SNR for sources to be considered. In this project it was found that PP worked best for SHOC data from the 40-inch telescope where the fields were not too sparse ($\gtrsim 10$ stars in the

[17] https://photometrypipeline.readthedocs.io/en/latest/
[18] https://github.com/mommermi/photometrypipeline
[19] https://www.scipy.org/
[20] https://matplotlib.org/
[21] http://python-future.org/
[22] https://scikit-image.org/
[23] https://pandas.pydata.org/
[24] http://www.astromatic.net/software/scamp
[25] http://www.astromatic.net/software/sextractor

FoV of SHOC) but also not too crowded ($\lesssim$ 50 stars in the FoV of SHOC), with stars that had an SNR of at least 3. PP requires at least 10 sources for the image registration to proceed. In the case of insufficient sources to do the astrometric and photometric calibration, PP will output instrumentation magnitudes. After the source extraction, SCAMP matched the extracted sources with sources in the GAIA Data Release 1[26] (GAIA DR1; Gaia Collaboration et al., 2016) catalogue, which was queried from the VizieR service[27] at the Centre de Données astronomiques de Strasbourg[28]. At least four sources had to be matched with the sources in GAIA DR1 for the registration to be successful.

After the astrometric calibration, PP performed aperture photometry with Source Extractor, through the commands `pp_extract` and `pp_photometry`, to measure the flux and its uncertainty of each identified source and thereby calculate the instrumental magnitudes. In PP, aperture photometry can be performed either through a curve-of-growth analysis, where PP attempts to auto-select the best aperture radius, or through a user-selected aperture radius. In this project, the latter method was used because pushing the exposure time limit to maximise the SNR for faint asteroids often resulted in slightly streaked background stars (see Figure 2.4 as an example). In those cases the aperture radius were manually set larger to ensure that the entire streak was captured by the pipeline.

The photometric calibration was performed with the command `pp_calibrate`. It compares the instrumental magnitudes of the background stars in each image to their respective magnitudes in photometric catalogues in order to calculate the magnitude zeropoint and its uncertainty. At least three background stars had to be successfully matched with sources in the catalogue for the calibration to be successful. PP makes use of four photometric catalogues in the optical bands: the Pan-STARRS Data Release 1 (DR1), SDSS DR9[29] (Ahn et al., 2012), AAVSO Photometric All-Sky Survey Release 9[30] (APASS9; Henden et al., 2016) and SkyMapper DR1[31] (Wolf et al., 2018). All of these catalogues have southern sky coverage and were queried with VizieR. Both SDSS DR9 and APASS9 have photometry available in SDSS filters (the same filters used in this project). Pan-STARRS and SkyMapper use slightly different filters to SDSS and therefore their photometry had to be transformed into SDSS photometry. Transformation equations from Tonry et al. (2012) are implemented by PP to transform Pan-STARRS $g\ r\ i\ z\ y$ to SDSS $g\ r\ i\ z$. There were no equations transforming SkyMapper magnitudes to SDSS magnitudes implemented in PP, which resulted in a discrepancy of the pilot results. This is described in more detail in Section 2.4.

Through the command `pp_calibrate`, the user can specify the catalogue used for the photometric calibration. If no specific catalogue was specified, PP will try all of the catalogues in the order SkyMapper→SDSS DR9→APASS9→Pan-STARRS until at least three catalogue sources were matched with the sources that had instrumental magnitudes. The majority of the photometry in this project were calibrated with SkyMapper because it was queried first and with its good southern sky coverage matched at least 3 stars in the FoV. The command also allows the user to adjust the number of sources used in the photometric calibration.

[26] https://sci.esa.int/web/gaia/
[27] http://vizier.u-strasbg.fr/viz-bin/VizieR
[28] http://cds.u-strasbg.fr/
[29] http://www.sdss3.org/dr9/
[30] https://www.aavso.org/apass
[31] http://skymapper.anu.edu.au/

The calibrated photometry of the targets were extracted using the command `pp_distill`, with the asteroid designation specified by the user as additional input. The function uses the Horizon's service via Python's `astroquery` package to determine the position of the target at the observation time.

In this project, the data in the three filters (r′, g′ and i′) were processed by the pipeline separately because PP is only designed for the input of images from a single filter at a time. PP is also intended for data where the field remains the same and the asteroid moves through the field from image to image. For the intended input format, PP can be supplied all images as a single input. In this project, with an ever-changing field, the images had to be processed individually, and because hundreds and sometimes thousands of images were taken for each observation, this was achieved by scripting PP's command line functions through a bash script. This significantly increased the run time of PP, with `pp_register` taking the most time. For example, the run time of 2007 YU56, which was observed for approximately 2 hours and had a total of 272 images (combined total in all three filters), was approximately 4 hours. In comparison, because of their slow sky rate, two MBAs (329 Svea and 175 Andromache) had star fields that remained the same over the observation period and could be processed by PP as its intended input format. The run time of 175 Andromache, which was observed for approximately 50 minutes and had 160 images in total, was approximately 45 minutes.

The calibrated photometry were also automatically flagged by PP from the final output file if the astrometric position of the selected source was more than 10 arcseconds away from the asteroid position predicted by the Horizon's service. This is because PP suspects that the photometry was not performed on the correct source in the frame (i.e., the asteroid). Data points were not flagged by PP if the target intersected a star which resulted in the counts from the star being included in the photometry calculation. It also did not flag the data points when PP could not perform the photometric calibration and recorded the instrumental magnitude instead of the apparent magnitude. The latter two scenarios would potentially show up as outliers in the light curves (see the top plot of Figure 2.5 where multiple cases like these are highlighted for one of the targets, 2020 HT2).

For all of the observations, the remaining outliers were manually removed. The resulting light curve of 2020 HT2 is shown in the bottom plot of Figure 2.5 as an example. Some of the other targets had outliers showing a decrease in brightness that could indicate an eclipsing event from a binary asteroid system, but this was not the focus of the study and those data points were also removed. It should be noted that this was not the case for 2020 HT2. The data of each target were scrubbed by discarding data that deviated within a 0.5 magnitude of the median magnitude. Asteroids rarely have a deviation in brightness (i.e., light curve amplitude) larger than about 1 magnitude. This is because for the brightness of an asteroid to vary by a magnitude of 1, it would require the reflected flux to change by a factor of 2.5 (refer to equation 1.2). For a rotating, hypothetical smooth asteroid, this would only occur if the length-to-width axis ratio was about 2:5. Such an extreme elongation is not impossible (e.g., the interstellar object 'Oumuamua, Vazan and Sari, 2020), but is rare. Additionally, Hatch and Wiegert (2015) report an axis ratio of ∼1.4 on average for small NEAs. Therefore a threshold of 0.5 magnitude is justified. A data point was also removed if the magnitude error was larger by a factor of 3.5 of the median magnitude error.

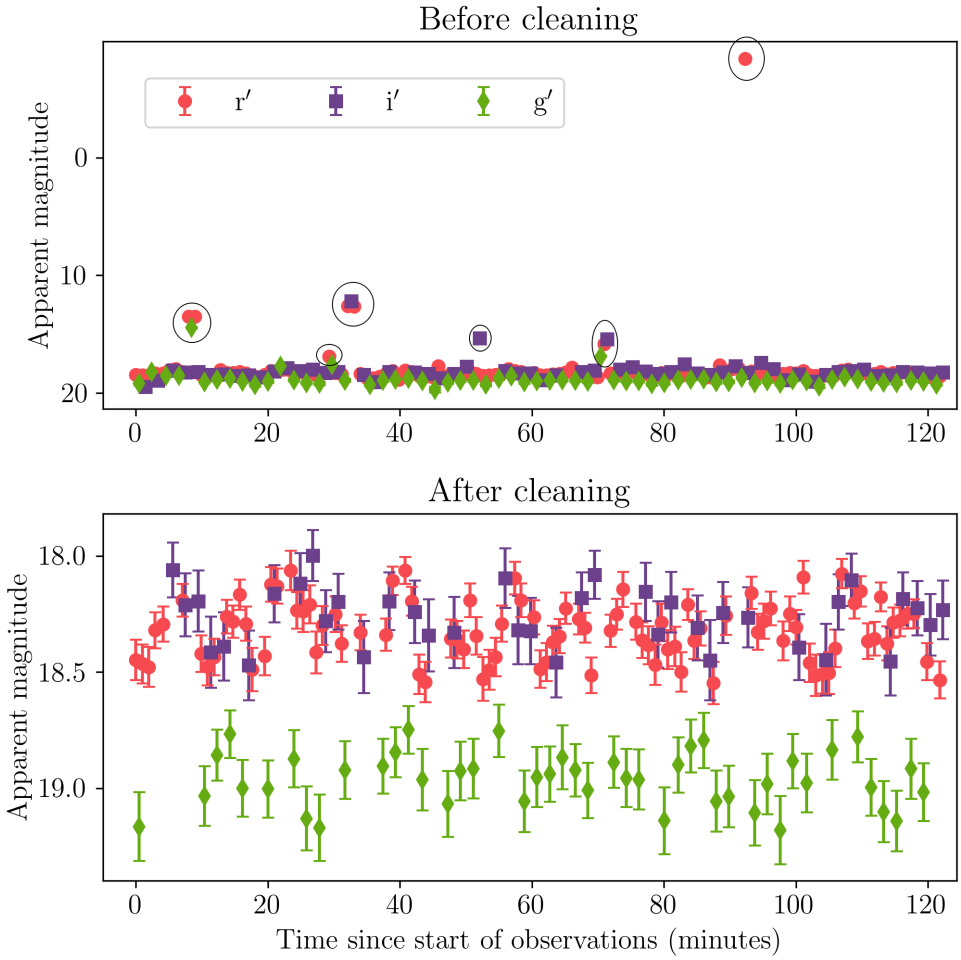

Figure 2.5: The light curve of 2020 HT2, where the green diamonds show the calibrated photometry in the g′-filter, the red circles in the r′-filter and the purple squares in the i′-filter. The top plot shows the photometric data extracted with PP. Some of the outliers are indicated with black circles. The bottom plot shows the final light curve after the outliers were manually removed.

A median of 53% of the r′-filter data, 47% of the i′-filter data and 41% of the g′-filter data were successfully put through PP and calibrated photometry (without outliers) were extracted. The data where the photometry extraction by PP was unsuccessful was in most cases due to not enough comparison stars in the field and therefore astrometric and photometric calibration could not be performed. It was inevitable that during the observational window, while tracking the asteroid with the small FoV, it would move into a part of the sky that were sparser than others. Therefore, some images had fewer stars in the frame than the minimum required by PP and hence resulting in the failure of the astrometric and photometric calibration. Hundreds of images were taken during the observational window with the field constantly changing. It would be a tedious exercise to stop/start the observations every time if visual inspection deemed the field too sparse or not. It was decided to continue the observations unabated and leave it up to PP to attempt calibration for each image. The photometry extraction of the g′- and i′-filter was not as successful as the r′-filter because less sources could be resolved in the FoV due to the quantum efficiency of SHOC decreasing at shorter and longer wavelengths (see Figure 2.3 in Section 2.1). Therefore there were not enough sources with a high enough SNR in the FoV to perform the astrometric and photometric calibration.

2.4 SkyMapper transformations

After the reduction and photometric calibration of the targets observed in the pilot study, the colours were calculated (see Section 2.5) and plotted on a colour-colour plot ($r'-i'$ vs $g'-r'$) which is shown in Figure 2.6. As discussed in Chapter 1, NEAs are mainly classified as either S- (stony) or C-type (carbonaceous) asteroids, with the majority classified as S-type (e.g., Carry et al., 2016; Ieva et al., 2018; Navarro-Meza et al., 2019). To determine if the initial results agreed with past studies, the expected colours of an S- and C-type asteroid were also plotted in Figure 2.6. The expected colours were estimated from the centres of the two distributions shown in Figure 2.7. This figure was obtained from Ivezić et al. (2001) and it shows the bimodal distribution of S- and C-type main-belt asteroids. As can be seen from Figure 2.6, most of the pilot study asteroids had C-type colours and none had a colour associated with a typical S-type asteroid. This was unexpected since literature suggests the majority of NEAs are S-type.

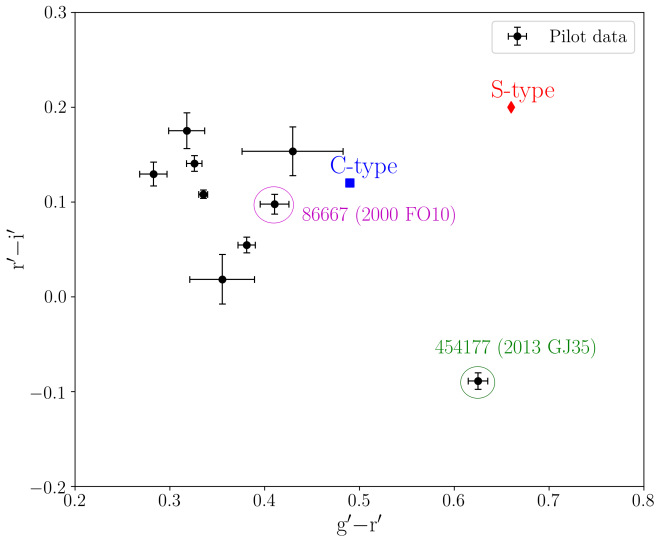

Figure 2.6: A colour-colour plot ($r'-i'$ vs $g'-r'$) of the targets observed during the pilot study. The colours of the pilot targets are plotted in black, the expected S-type colours plotted as a red diamond and the expected C-type colours as a blue square. The extracted pilot colours did not agree with the literature where most NEAs are classified as S-type asteroids. In addition, 86667 (2000 FO10), a well-studied S-type NEA (indicated with a magenta circle) appears to be classified here as a C-type. The location of 454177 (2013 GJ35) (shown with a green circle) led to an investigation into the photometric calibration performed by PP.

Additionally, 86667 (2000 FO10), a well-studied large NEA observed in the pilot project, has been classified as an S-type asteroid by Carry et al. (2016) from SDSS photometry. This target is indicated with a magenta circle in Figure 2.6. The pilot-study colour of this NEA suggested that this was a C-type asteroid which also raised concerns about the colour determination. There appeared to be a colour offset of $\sim$0.2 magnitude in $g'-r'$ and an offset of $\sim$0.03 magnitude in $r'-i'$. These offsets, especially in $g'-r'$, hinted that there was potentially a problem with the extracted g' magnitudes of the asteroids.

In order to investigate the potential colour offset further, aperture photometry was performed manually with the Image Reduction and Analysis Facility[32] (IRAF; Tody, 1986, 1993) on one image per filter of one of the targets to confirm that PP measured the flux of the sources correctly. After confirming with IRAF that the aperture photometry was performed correctly by PP, the photometric calibration of PP was investigated next, in particular the calibration of 454177 (2013 GJ35). This target was separate from the other NEAs and the expected S- and C-type colours in the colour-colour plot (Figure 2.6).

[32] http://ast.noao.edu/data/software

The reason for its separation was because the data of 2013 GJ35 were calibrated with PP using two different catalogues: the r′ data were calibrated with SkyMapper and the g′ and i′ data were calibrated with Pan-STARRS.

The difference between the photometric calibration performed with SkyMapper and Pan-STARRS were further investigated by obtaining the calibrated photometry of another target, 2007 YU56, through PP, but specifying which catalogue should be used. 2007 YU56 was chosen because it was at a declination of ∼0° and therefore catalogues in the Northern hemisphere should have had photometric coverage as well. SDSS was not tested because there were no sources in the catalogue at this location in the sky. The light curve of 2007 YU56 is shown in Figure 2.9, where in 2.9a the data were calibrated with SkyMapper and in 2.9b with Pan-STARRS. A clear difference can be seen between the light curves and the respective colours. Since the observations in this project were performed with SDSS filters, the photometry of the reference stars had to be in the SDSS system as well. In PP, the photometry from Pan-STARRS are transformed to SDSS before the photometric calibration is performed, but in the case of SkyMapper, PP assumed that the photometry was given as SDSS magnitudes.

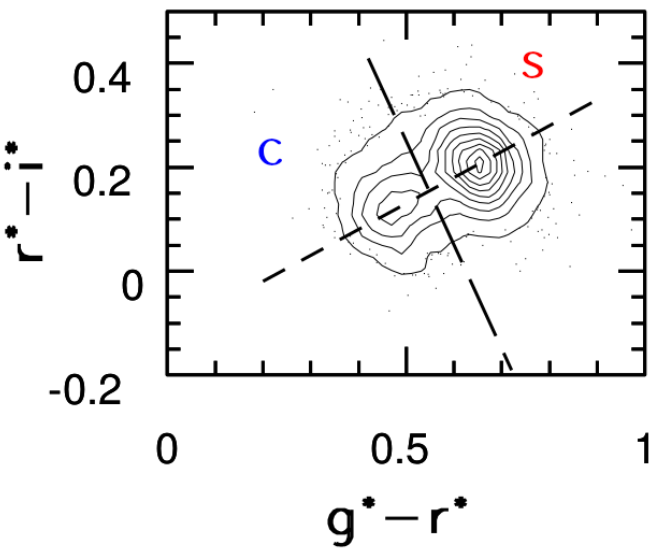

Figure 2.7: Colour-colour plot (r^*-i^* vs g^*-r^*) from Ivezić et al. (2001) showing the distribution of MBAs from SDSS data. A clear separation between the S- and C-type asteroids can be seen in the distribution. The g^*, r^* and i^* magnitudes are simply the measured photometry in the g′, r′ and i′ filters, respectively. The colours were estimated at the centre of each of the contours.

Further investigation revealed that SkyMapper's filters are slightly different from SDSS filters in order to study the surface gravity of stars in the Milky Way (Wolf et al., 2018). There are six SkyMapper filters (u v g r i z) and their transmission curves from Bessell et al. (2011) are shown in Figure 2.8, together with the SDSS transmission curves. The Hydrogen Balmer break can be studied with the $u-v$ colour and the metallicity with the $v-g$ colour. The SDSS r′, i′ and z′ filters are similar to the SkyMapper r, i and z filters, but the SDSS u′-filter was split into a SkyMapper violet v-filter and a shorter-wavelength u-filter. As a result, the blue edge of the SkyMapper g-filter is at a longer wavelength compared to the SDSS g′-filter. Because of the slightly different filters, SkyMapper photometry is different to SDSS photometry and transformation equations are required to transform from the SkyMapper to the SDSS system, which was not implemented in PP.

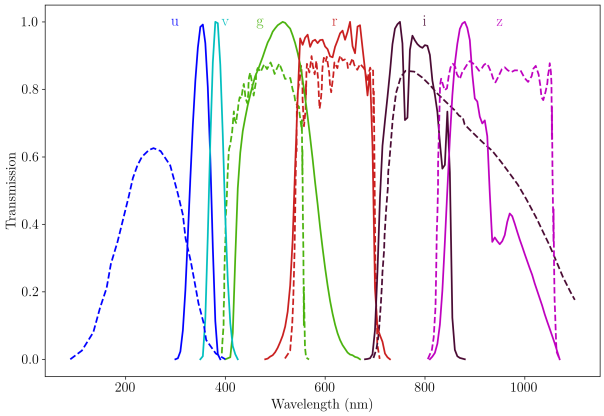

Figure 2.8: Shown in solid lines are the SkyMapper transmission curves from Bessell et al. (2011) for the six SkyMapper filters: u v g r i z. The transmission curves for the SDSS filters on the 40-inch telescope (u′ g′ r′ i′ z′) are also shown for comparison with dashed lines.

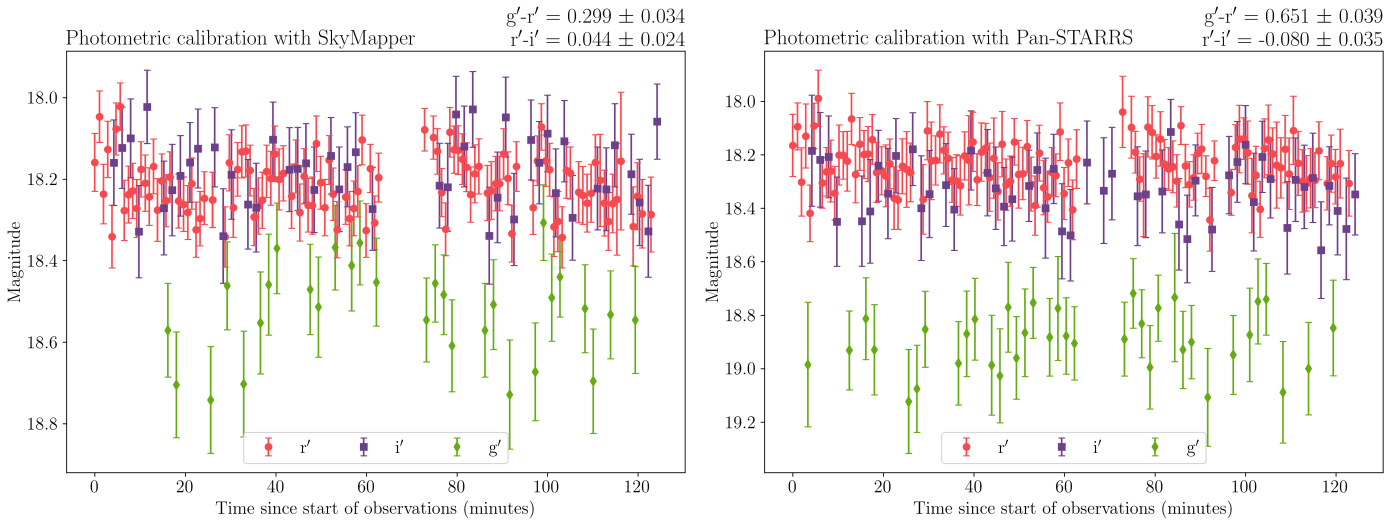

(a) Photometric calibration performed with SkyMapper.

(b) Photometric calibration performed with Pan-STARRS.

Figure 2.9: Shown is the light curve (apparent magnitude as a function of time) of 2007 YU56. The apparent magnitude is indicated as green diamonds for the g′-filter, red circles for the r′-filter and purple squares for the i′-filter. The g′−r′ and r′−i′ colours are also displayed in the top-right corner of each plot. The photometric calibration was performed by PP with two different catalogues: (a) SkyMapper and (b) Pan-STARRS. The SkyMapper photometry was extracted before any transformation equations were implemented in PP.

At the time of writing, there were no published transformation equations from the SkyMapper to the SDSS system. However, Wolf et al. (2018) compared the photometry in the two systems using synthetic photometry of F- and G-type main-sequence stars in the luminosity class IV and V, as well as giant and white dwarf stars. This can be seen in Figure 2.10a which is also available on the SkyMapper website[33] and Figure 17 in Wolf et al. (2018). The data of the main-sequence stars were extracted from the individual plots in Figure 2.10a with WebPlotDigitizer[34] (Rohatgi, 2020) so that transformation equations could be extracted. Only the F- and G-type main-sequence stars with luminosity class IV and V were used, following the recommendation from the SkyMapper website, because they are situated at the centre of the main-sequence and the colour terms between SkyMapper and SDSS have a low scatter as a function of the SkyMapper $g - i$ colour.

Transformation equations from the SkyMapper to SDSS system were calculated for the g-, r-, i- and z-filter by fitting linear equations to the main-sequence data. The main-sequence data and linear fits with the fitting parameters are shown in Figure 2.10b. The data were separated at a $g - i$ value where a clear discontinuity in the data was present and two separate linear equations were fitted per filter. Polynomials were also fitted and tested, but they did not perform as well as the linear transformation equations (discussed later). The transformation equations are given in equations 2.2, 2.3, 2.4 and 2.5 for the g-, r-, i- and z-filter, respectively.

[33] http://skymapper.anu.edu.au/filter-transformations/
[34] https://automeris.io/WebPlotDigitizer/index.html

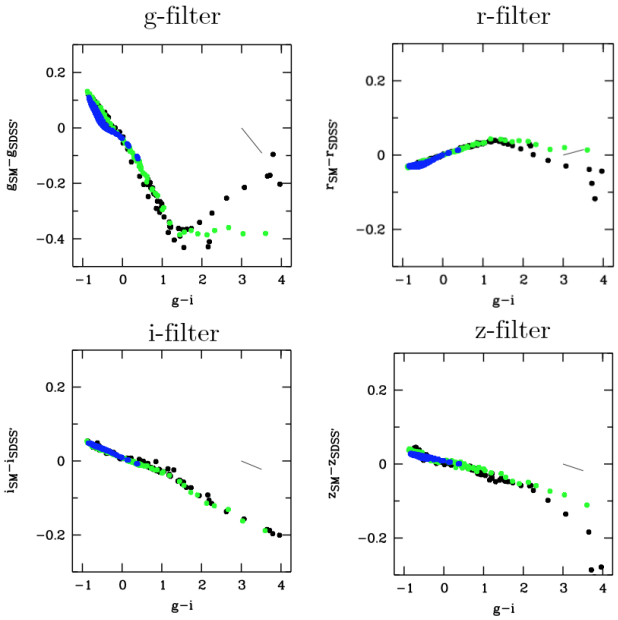

(a) Figures from the Skymapper website[35] and also available in Figure 17 of Wolf et al. (2018).

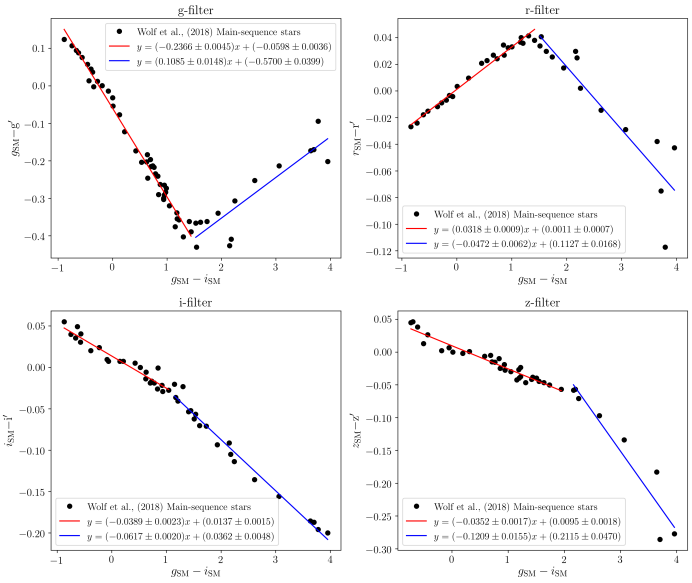

(b) Extracted main-sequence data with linear equations.

Figure 2.10: Colour differences between SkyMapper and SDSS are plotted as a function of the SkyMapper $g-i$ colour in the g-, r-, i- and z-filter. (a) Plotted are the synthetic colours of IV/V Main-Sequence stars (black), giant stars (green) and DA/DB white dwarfs (blue). (b) Data of the main-sequence stars are extracted from (a) and two linear equations are fitted to determine the transformation equations. The two linear equations are shown in red and blue.

SkyMapper g to SDSS g′

$$\begin{aligned} \text{For } (g-i) < 1.5: \quad g' &= g - (-0.2366 \pm 0.0045) \times (g-i) - (-0.0598 \pm 0.0036) \\ \text{For } (g-i) > 1.5: \quad g' &= g - (0.1085 \pm 0.0148) \times (g-i) - (-0.5700 \pm 0.0399) \end{aligned} \tag{2.2}$$

SkyMapper r to SDSS r′

$$\begin{aligned} \text{For } (g-i) < 1.5: \quad r' &= r - (0.0318 \pm 0.0009) \times (g-i) - (0.0011 \pm 0.0007) \\ \text{For } (g-i) > 1.5: \quad r' &= r - (-0.0472 \pm 0.0062) \times (g-i) - (0.1127 \pm 0.0168) \end{aligned} \tag{2.3}$$

SkyMapper i to SDSS i′

$$\begin{aligned} \text{For } (g-i) < 1.1: \quad i' &= i - (-0.0389 \pm 0.0023) \times (g-i) - (0.0137 \pm 0.0015) \\ \text{For } (g-i) > 1.1: \quad i' &= i - (-0.0617 \pm 0.0020) \times (g-i) - (0.0362 \pm 0.0048) \end{aligned} \tag{2.4}$$

SkyMapper z to SDSS z′

$$\begin{aligned} \text{For } (g-i) < 2: \quad z' &= z - (-0.0352 \pm 0.0017) \times (g-i) - (0.0095 \pm 0.0018) \\ \text{For } (g-i) > 2: \quad z' &= z - (-0.1209 \pm 0.0155) \times (g-i) - (0.2115 \pm 0.0470) \end{aligned} \tag{2.5}$$

[35] http://skymapper.anu.edu.au/filter-transformations/

Synthetic photometry of 74 Hubble Space Telescope (HST) standard stars (also from the SkyMapper website[36]) were used to test if the transformation equations were successful. The photometry of each standard star was available in various photometric systems, including SkyMapper and SDSS and it ranged in-between SkyMapper $g - i$ values of -0.89 and 4.36. The SkyMapper photometry of the standard stars were transformed to SDSS by using the linear transformation equations (equations 2.2 to 2.5). The difference between the measured SDSS photometry and the photometry from the transformation equations were then calculated. The median difference was 0.002 for the g- and r-filter, 0.003 for the i-filter and 0.001 for the z-filter. In comparison, when the polynomial transformation equations were used, the median difference was 0.012 for the g-filter, 0.006 for the r- and z-filter and 0.004 for the i-filter. Figure 2.11 also shows, as an example, the transformed g′ magnitudes as a function of the measured magnitudes. A clear 1:1 relationship can be seen. The r′, i′ and z′ filters show a similar relationship.

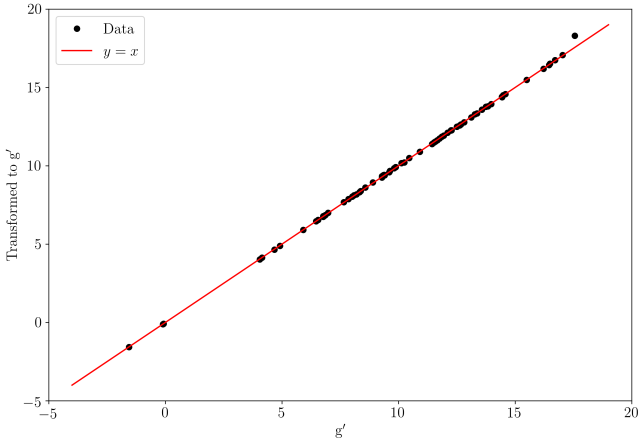

Figure 2.11: Shown on the x-axis are the measured g′ magnitude values of the HST standard stars obtained from the SkyMapper website. Plotted on the y-axis are the g′ magnitude values calculated by using the transformations in equation 2.2 to transform the SkyMapper g magnitude to g′. A 1:1 relationship is also shown with a red line.

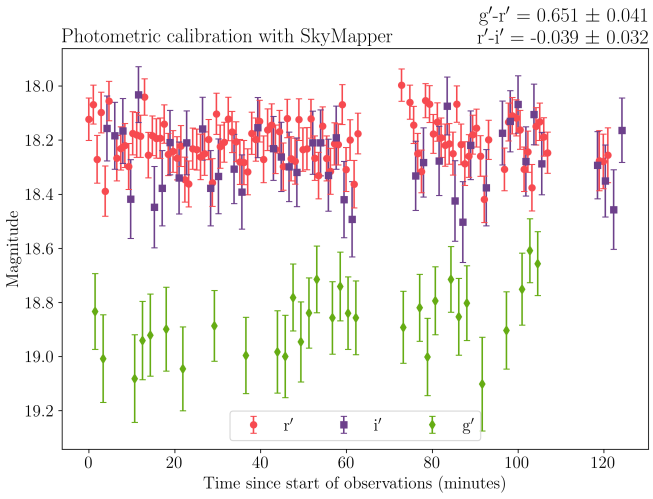

(a) Photometric calibration performed with SkyMapper photometry transformed to SDSS.

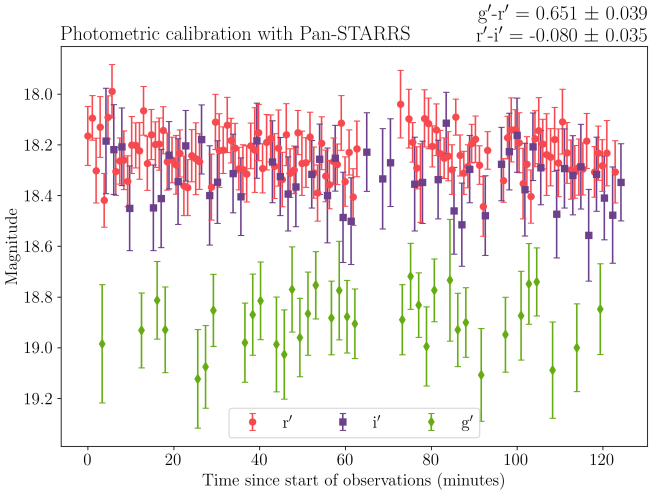

(b) Photometric calibration performed with Pan-STARRS. The same as Figure 2.9b.

Figure 2.12: Shown again is the light curve of 2007 YU56, similar to Figure 2.9, but here the photometry were extracted with SkyMapper after the transformation equations were implemented in PP. The apparent magnitude is indicated as green diamonds for the g′-filter, red circles for the r′-filter and purple squares for the i′-filter. The g′−r′ and r′−i′ colours are again displayed in the top-right corner of each plot. (a) shows the photometry calibrated with SkyMapper and (b) shows the calibration with Pan-STARRS.

[36] http://skymapper.anu.edu.au/filter-transformations/

The equations transforming SkyMapper photometry to SDSS were then implemented in PP's code base with guidance from the developer Michael Mommert. There were two Python scripts that had to be modified: `catalog.py` and `pp_calibrate.py`, where `pp_calibrate.py` performs the photometric calibration through the command `pp_calibrate` and `catalog.py` queries the required catalogues and performs the transformations between photometric systems when necessary. The transformation equations were inserted into `catalog.py`, and the relevant lines of code in `pp_calibrate.py` were modified so that the pipeline knew to perform the transformation from SkyMapper to SDSS when the SkyMapper catalogue was used by the pipeline. The code changes were also pushed to the master PP in the PP Github repository[37].

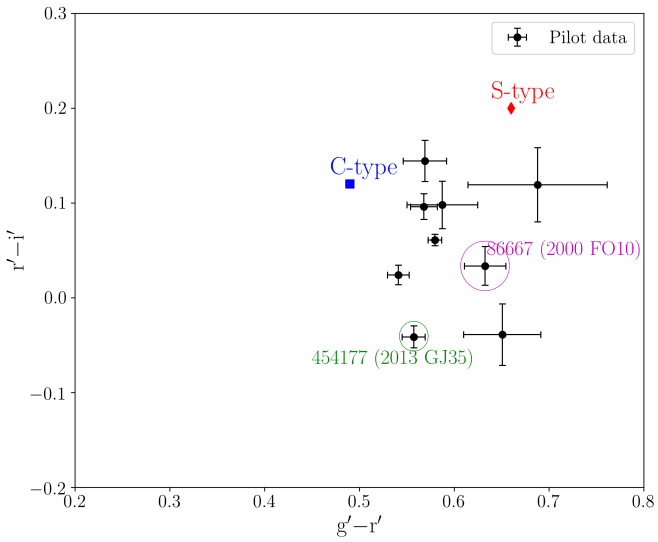

Figure 2.13: The same as Figure 2.6, however here the colour-colour plot shows the reprocessed pilot data after the SkyMapper-SDSS transformation equations were implemented in PP. The colours of the pilot targets are plotted in black, the expected S-type colours plotted as a red diamond and the expected C-type colours as a blue square.

To confirm that the transformation equations were implemented correctly by PP, calibrated photometry of 2007 YU56 were extracted with the pipeline again, but this time specifying that the photometric calibration had to be performed with only SkyMapper. In Figure 2.12 the light curve of 2007 YU56 is shown again (similar to Figure 2.9), but here Figure 2.12a shows the light curve where the photometry was calibrated with the transformed SkyMapper photometry. Figure 2.12b is the same as Figure 2.9b and is only provided for comparison. The colours calculated with SkyMapper and Pan-STARRS also agree within 1σ for $g'-r'$ and 2σ for $r'-i'$, where σ is the uncertainty in the colour. All data were reprocessed through PP after the transformation equations were implemented. The colours of the reprocessed pilot targets are shown in Figure 2.13. Further analysis are described in Sections 2.5 and 2.6, and the results are shown and discussed in Chapter 3.

[37] https://github.com/mommermi/photometrypipeline

2.5 Colours and taxonomy determination

Most asteroids are rotating and can have an irregular shape. This can manifest into a change in observed brightness as a function of time, as seen from the perspective of the observer, as more or less sunlight is reflected off of the changing surface area. An asteroid can also have a non-uniform albedo over its surface, meaning that different regions on the asteroid surface will have a different colour (Szabó et al., 2004), however, this effect is much weaker and not typically seen in a light curve. Additionally, an NEA can also have a rotation period of a few minutes or sometimes seconds. For example, 2012 TC4, a ∼10 m NEA, has a rotation period of 12.2 minutes (Reddy et al., 2019) and Thirouin et al. (2018) showed that NEAs with diameters ∼10 m can also have rotation periods of only a few seconds, as discussed in Chapter 1. Therefore, in order to accurately calculate the colours, the magnitudes in the different photometric filters ideally have to be recorded at the same time. For the setup used in this study (see Section 2.1), this was unfortunately not possible.

To account for the light curve changes, a similar approach to that of Mommert et al. (2016) was taken where they cycled *J, K, Z* and *H* filters and interpolated the *J* magnitudes. Similarly, in this study, the magnitudes were measured in the sequence r′-g′-r′-i′, with approximately 30 seconds between each exposure. This time includes the exposure and readout time, and the time it took to perform the filter-change (see Section 2.1). Here, a linear interpolation was performed between adjacent r′ observations to get an approximate measurement of the r′ magnitude at the observation times of the g′ and i′ measurements. The g′−r′ colour was calculated by simply subtracting the interpolated r′ measurements from the g′ measurements and the r′−i′ colour was calculated by subtracting the i′ measurements from the interpolated r′ measurements. The uncertainty in each colour measurement was calculated, also following a similar approach to Mommert et al. (2016), as the root-sum-square of the three measurement uncertainties involved in the colour calculation, i.e., two r′ uncertainties and one g′ or i′ uncertainty.

The final colour was calculated by taking the weighted mean of all the colour measurements that could be made within the observation window, where the weights were the inverse of the squared colour uncertainties. The final colour uncertainty was calculated as the root-sum-square of the standard error of the mean and the uncertainty in the weighted mean of the colour measurements (σ_{mean}). The standard error of the mean is $\sigma/\sqrt{N}$, where σ was the standard deviation of the colour measurements and N was the number of colour measurements. The uncertainty in the weighted mean can be calculated from error propagation and is given by equation 2.6, where σ_i is the uncertainty in each colour measurement.

$$\sigma_{\text{mean}} = \sqrt{\frac{1}{\sum_i \frac{1}{\sigma_i^2}}} \tag{2.6}$$

For the targets that were observed on two consecutive nights, the data were first combined and then the colours were calculated using the data from both observations.

The colours g′−r′ and r′−i′ were used to calculate the a^* parameter of the asteroids observed in this project. This parameter was defined by Ivezić et al. (2001) through rotating and translating the r*−i* vs g*−r* coordinate system, as seen in Figure 2.14, which is the same as Figure 2.7, but shown here again. The a^* parameter can be calculated through equation 2.7, where g*, r* and i* are simply the measured magnitudes in the g′, r′ and i′ filters, respectively.

$$a^* = 0.89(g^* - r^*) + 0.45(r^* - i^*) - 0.57 \quad (2.7)$$

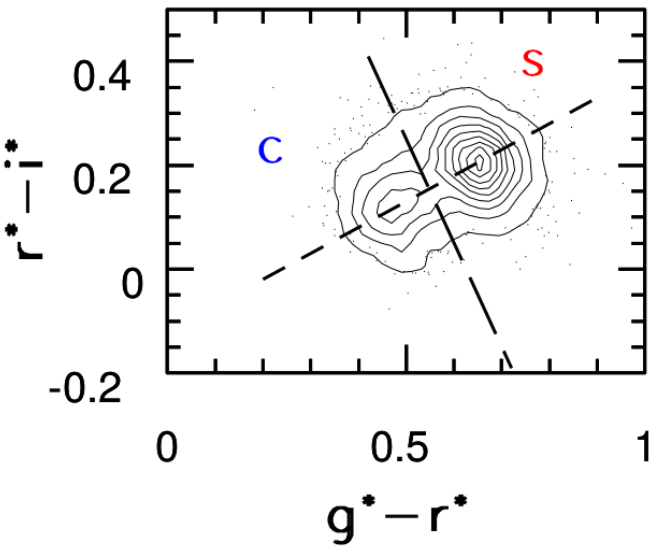

Figure 2.14: The same plot as Figure 2.7. Colour-colour (r*−i* vs g*−r*) plot from Ivezić et al. (2001) showing the distribution of MBAs from SDSS data. A clear separation between the S- and C-type asteroids can be seen in the distribution. The g*, r* and i* magnitudes are simply the measured photometry in the g′, r′ and i′ filters, respectively. The two dashed lines indicate the rotated coordinate system that was used by Ivezić et al. (2001) to define the a^* parameter.

As discussed by Ivezić et al. (2001), the a^* parameter can distinguish the redder asteroids (e.g., S-, Q- and V-type) from the bluer asteroids (e.g., C-type), but it cannot, for example, distinguish between the redder asteroid types (e.g., between S-, Q- or V-type) or between the bluer asteroids (e.g., between C- or B-type). A positive a^* value indicates that the asteroid is redder and a negative value that the asteroid is bluer. NEAs are mainly classified as either silicon-rich (S) or carbon-based (C) asteroids, which was discussed in Chapter 1 and Section 2.4. To visually inspect the separation between the redder and bluer asteroids in this project, the a^* value of each target were compared to the a^* values of well-studied inner main-belt asteroids by using the supplementary data of Delbo' et al. (2017).

Delbo' et al. (2017, suppl.) contains a summary of important parameters for over 150 000 known inner main-belt asteroids. This includes:

- The absolute magnitude (H) and slope parameter (G), as well as the proper semi-major axis, eccentricity and inclination of every asteroid.
- The rotation period of over 5 000 asteroids.
- The diameter, albedo and taxonomic type for over 20 000 asteroids.

The taxonomic type of each inner MBA is given in seven taxonomic classification schemes, if the taxonomy has been determined in the specific scheme. The classification schemes are Bus-DeMeo (DeMeo et al., 2009), Bus (Bus and Binzel, 2002), SMASS (Xu et al., 1995), Tholen (Tholen, 1989), S^3OS^2 (Lazzaro et al., 2004) and two systems that are based on SDSS photometry (Demeo and Carry, 2013) and SDSS spectroscopy (Carvano et al., 2010). These schemes were all discussed in Chapter 1. Even though these are different classification schemes, they do build on one another. The Bus and SMASS scheme builds on Tholen and in turn Bus-DeMeo, S^3OS^2, DeMeo and Carry, and Carvano builds on the Bus scheme.

The a^* parameters are also given in Delbo' et al. (2017, suppl.) for over 10 000 inner MBAs classified as S-, C-, X-, D-, Q- or V-type asteroids (the taxonomic classes considered in this project, see Chapter 1). Figure 2.15 shows the absolute magnitude of these asteroids plotted as a function of their a^* parameter. The plot shows that the a^* parameter can differentiate between the redder and bluer asteroids, but it cannot differentiate between the S-, Q- and V-type asteroids because they overlap in a^*-space. The a^* values of the targets observed in this project are shown and discussed in Chapter 3.

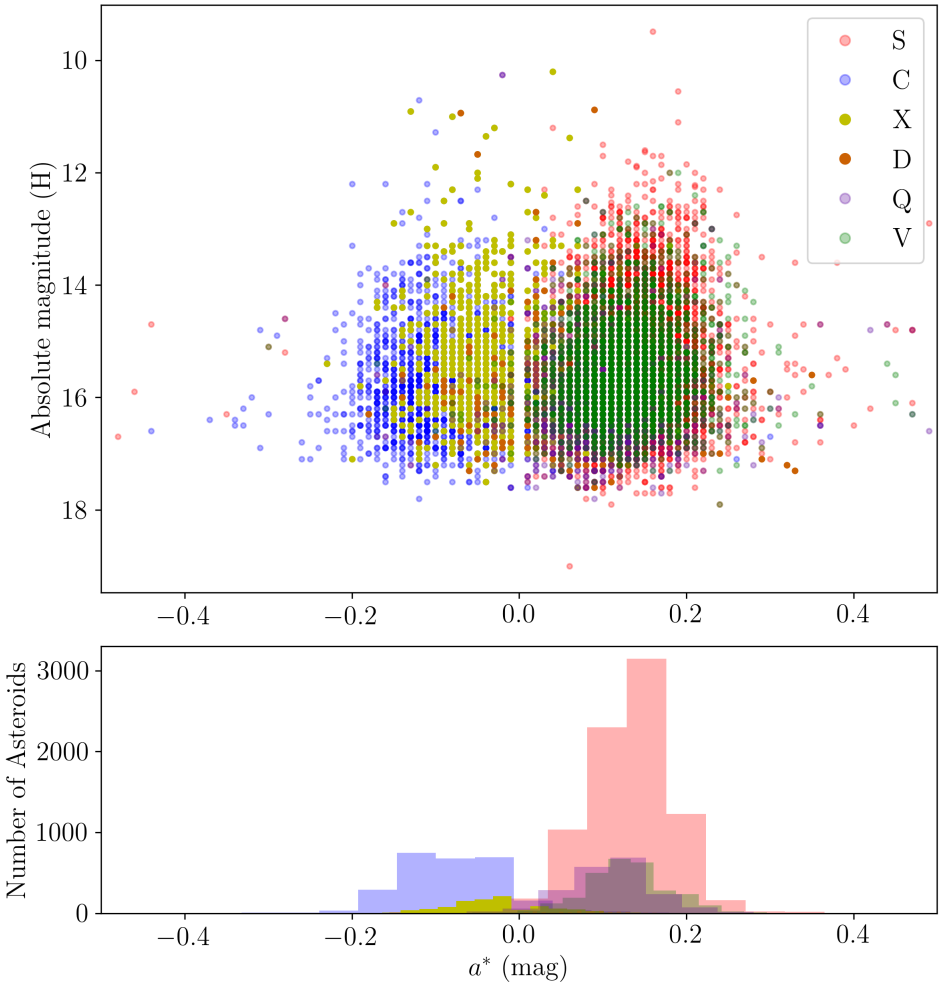

Figure 2.15: The top plot shows the absolute magnitude (H) plotted as a function of the a^* parameter from data of inner MBAs in the supplementary data of Delbo' et al. (2017). Only the asteroids classified as one of the taxonomic classes considered in this project are plotted: 8208 S-type (red), 2717 C-type (blue), 1018 X-type (yellow), 355 D-type (orange), 1989 Q-type (purple) and 2845 V-type (green) asteroids. The asteroids were classified by the taxonomic schemes given in this section. The bottom plot shows the distribution of each class. The S-, Q- and V-type asteroids all overlap in a^*-space at mostly positive a^* values, C-type asteroids are mostly at $a^* < 0$ and X- and D-types cover both positive and negative a^* values.

As discussed above, the a^* parameter is sufficient for distinguishing between redder and bluer asteroids, but to differentiate further between different redder or different bluer asteroids, a more sophisticated approach is required. For this project, in order to obtain a more discrete classification, the colours $g'-r'$ and $r'-i'$ were used, in combination with a machine learning (ML) algorithm trained on synthetic colours, to classify the targets according to the Bus-DeMeo classification scheme (DeMeo et al., 2009). A similar approach to Erasmus et al. (2017, 2020) and Mommert et al. (2016, 2020) was followed.

The training sample (a requirement for ML classification techniques) was built through synthesising g′−r′ and r′−i′ colours from asteroid spectra in the MIT-Hawaii Near-Earth Object Spectroscopic Survey[38] (MITHNEOS; Binzel et al., 2019). The spectra from MITHNEOS includes near-infrared (NIR) data, covering the wavelength range between 0.8 and 2.5 microns, and optical data from the MIT SMASS observing program[39] (e.g., Xu et al., 1995; Bus and Binzel, 2002), covering the wavelength range between approximately 0.45 and 0.95 microns. The NIR data were measured with *SpeX* (Rayner et al., 2003) on the NASA Infrared Telescope Facility (IRTF). Spectra were used because the taxonomic type can be unambiguously determined from it, which is not possible with, for example, asteroid colours from literature. The success of the ML algorithm depends on the quality of the training data and labels.

Each spectrum was classified according to the Bus-DeMeo scheme by Navarro-Meza et al. (2019) and were provided to be used in this project. Three taxonomic complexes (S, C and X) and three taxonomic types (D, Q and V) were considered in this project, as discussed in Chapter 1. Only these taxonomies were considered because there were sufficient spectroscopic data. The S-complex included the spectra of all the subtypes: S, Sa, Sk, Sq, Sr, Sv and Sw, where S was the most abundant. Similarly for the C-complex (C, Cb, Cg, Cgh and Ch) and X-complex (X, Xc, Xe, Xk and Xn). It should be noted that because all of the taxonomic types in the Bus-DeMeo classification scheme were not included and because some taxonomies were close together in the g′−r′ vs r′−i′ colour space (like the C- and X-complex), there might be an ambiguity with the classification. Therefore, in this project, a probabilistic classification is provided instead (see Chapter 3).

Before synthesising colours from the spectra, each spectrum and its respective uncertainties were linearly extrapolated to the short wavelength edge of the g′-filter (∼0.4 microns) with `numpy` using the first 30 data points of each spectrum, following Erasmus et al. (2020). This was done because the minimum wavelength of all of the spectra was greater than the short wavelength edge of the g′-filter. Only the first 30 data points of the spectrum were used in the extension because the spectrum was mostly linear in that wavelength range, as can be seen in the average reflectance spectra (DeMeo et al., 2009) shown in Figure 2.16 and in the spectra of three asteroids shown in Figure 2.17. In addition, to accommodate the linear extrapolation described above, only the measured spectra with a starting wavelength of ≤ 0.5 microns were used to extract synthetic photometry.

The colours were synthesized following the procedure used by Erasmus et al. (2020), where the flux (F) in each filter (g′, r′ and i′) was calculated by convolving the g′-, r′- and i′-filter transmissions with each of the measured spectra. The magnitude (m) in each filter was then calculated through $m = -2.5 \log_{10}(F)$. In order to calibrate the synthetic photometry, the zero-point magnitudes were calculated similarly by convolving the filter transmissions with the Solar spectrum[40]. The total synthetic colours were 196, which includes the S-complex: 118, C-complex: 27, X-complex: 30, D-type: 4, Q-type: 12 and V-type: 5.

Some of taxonomic types (e.g., D and V) only had very few synthetic colours that could be extracted from published spectra. The performance of the ML algorithm can be improved by increasing

[38] http://smass.mit.edu/minus.html
[39] http://smass.mit.edu/smass.html
[40] http://kurucz.harvard.edu/stars.html

the training data. All of the training data were increased by using the average reflectance spectra from DeMeo et al. (2009). The average reflectance spectra were also extrapolated to ∼0.4 microns, but here through fitting a cubic spline to the four shortest wavelengths with `scipy.interpolate`, following a similar approach to Mommert et al. (2020). The cubic spline fits for the S- and C-type spectra are illustrated in Figure 2.16a and the extended average reflectance spectra for the S-, C-, X-, D-, Q- and V-type asteroids are plotted in Figure 2.16b, in addition to the transmission curves of the g′-, r′- and i′-filter on the 40-inch telescope.

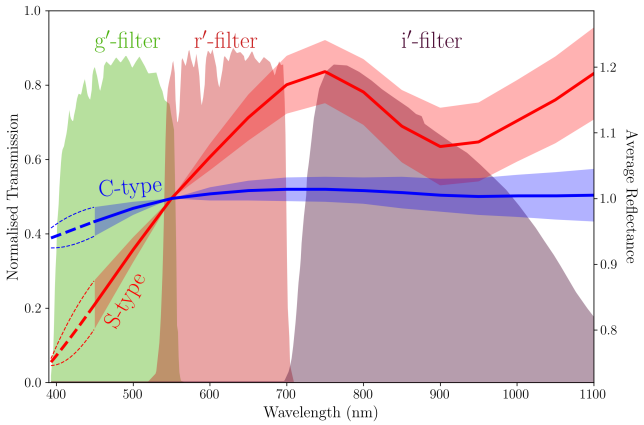

(a) Average reflectance spectra of an S- and C-type asteroid, where the cubic spline extensions are demonstrated with dashed lines.

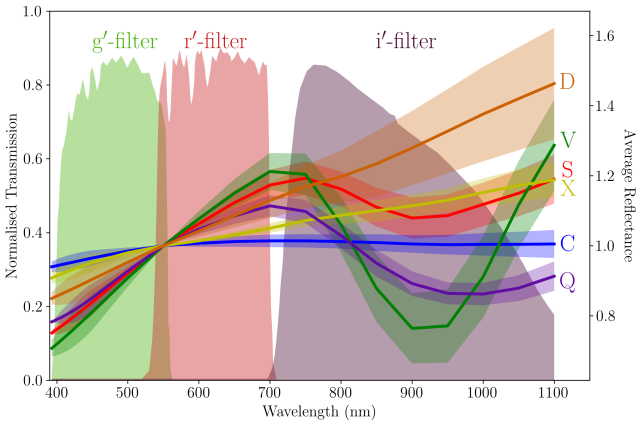

(b) Average reflectance spectra of an S-, C-, X-, D-, Q- and V-type asteroid, extended to ∼0.4 microns with a cubic spline.

Figure 2.16: The filter transmissions of the g′, r′ and i′ filters on the 40-inch telescope are shown in transparent green, red and purple, respectively. (a) The cubic spline extension to ∼0.4 microns (400 nm) of the average reflectance spectra is illustrated with dashed lines for the S- (red) and C-type (blue) asteroids. The upper and lower bounds in each type are also indicated with shading. (b) The average reflectance spectra for S- (red), C- (blue), X- (yellow), D- (orange), Q- (purple) and V-type (green) asteroids are shown, where the spectra were extended to ∼0.4 microns with a cubic spline to include the short wavelength edge of the g′-filter. The upper and lower bounds are again shown with shading.

The average colours were synthesised in the same way as the colours from the measured asteroid spectra. The same procedure was also followed with the upper and lower bounds of the average spectra in order to calculate the uncertainty in the average colours. Training data were added in each of the taxonomies by generating 30 random colours, following a uniform distribution, within the upper and lower bounds of the average colours. Therefore, the total amount of synthetic data used to train the machine learning algorithm were 376, which includes the S-complex: 148, C-complex: 57, X-complex: 60, D-type: 34, Q-type: 42, and V-type: 35.

Finally, to do finer calibration of all of the synthetic colours, three of the targets that were observed in this project and also had published spectra available in MITHNEOS (the source for the synthetic colours) were used. The three targets were 1620 Geographos (1951 RA), 141 Lumen (A875 AA) and 175 Andromache (A877 TA) and their spectra are shown in Figure 2.17. Their observed and synthetic colours are shown in Table 2.2. The median difference between these two colours were used to shift all of the synthetic colours (including the average colours). The reason for the difference between the observed and synthetic colours could be because only relative photometric calibration was performed on the synthetic photometry, not absolute photometric calibration. The latter method was challenging because it was sensitive to the exact filter responses and the solar spectra.

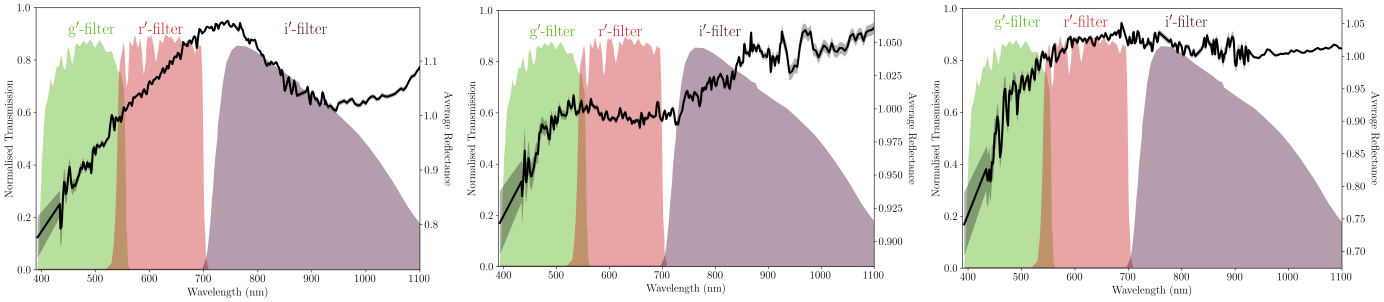

(a) 1620 Geographos (1951 RA)

(b) 141 Lumen (A875 AA)

(c) 175 Andromache (A877 TA)

Figure 2.17: The filter transmissions of the g′, r′ and i′ filters on the 40-inch telescope are shown in transparent green, red and purple, respectively. The reflectance spectra for the three calibrators are shown in black for (a) 1620 Geographos, (b) 141 Lumen and (c) 175 Andromache. The spectra were linearly extrapolated to ∼0.4 microns in order to include the short wavelength edge of the g′-filter. The upper and lower bounds of each spectra are also indicated with shading. The synthetic and observed colours of each target is shown in Table 2.2.

The *shifted* synthetic colours were used as the training data in the machine learning algorithm. As seen in Figure 2.20a, the separation of the shifted S- and C-complex training data, was consistent with the colour-colour plot in Ivezić et al. (2001), which is shown in Figure 2.14.

Table 2.2: Synthetic and observed colours of the three calibrators.

	Synthetic colours		Observed colours	
	g′−r′	r′−i′	g′−r′	r′−i′
1620 Geographos (1951 RA)	0.314	0.589	0.652	0.112
141 Lumen (A875 AA)	0.148	0.625	0.507	0.017
175 Andromache (A877 TA)	0.251	0.578	0.488	0.080

Following a similar approach to Erasmus et al. (2017, 2018, 2019) and Mommert et al. (2016, 2020), the targets were classified by training a k-Nearest-Neighbor (kNN) classifier on the synthetic data, through the Python implementation `sklearn.neighbours.KNeighborsClassifier`[41] (Pedregosa et al., 2011). As the name suggests, kNN classifies an object based on the class of the k number of objects nearest to it.

In this project, 30% of the synthetic data were randomly set aside to use as test data in order to evaluate the accuracy of the ML algorithm. The ML algorithm was only trained on the remaining 70% of the data (further referred to as training data). The process of how the ML algorithm was trained is shown in Figure 2.18. The k parameter was determined by searching for the parameter with the highest accuracy using a combined grid-search and cross-validation approach through `sklearn.model_selection.GridSearchCV`. In the grid search, the algorithm was trained using values of k between 1 and 30. For each value of k, the accuracy of the algorithm was determined through a five-fold cross-validation, as illustrated in Figure 2.18. With five folds, the training data are divided such that $^1/_5$ of the training data were set aside as a "validation set" to evaluate the accuracy of the algorithm and the remaining $^4/_5$ of the training data were used to train the algorithm. The final accuracy was calculated as the average accuracy over the five folds. The parameter with the highest accuracy was used to train the algorithm. In this project, the parameter with the highest accuracy was $k = 4$, with a validation sample accuracy of 95%.

[41] https://scikit-learn.org/stable/index.html

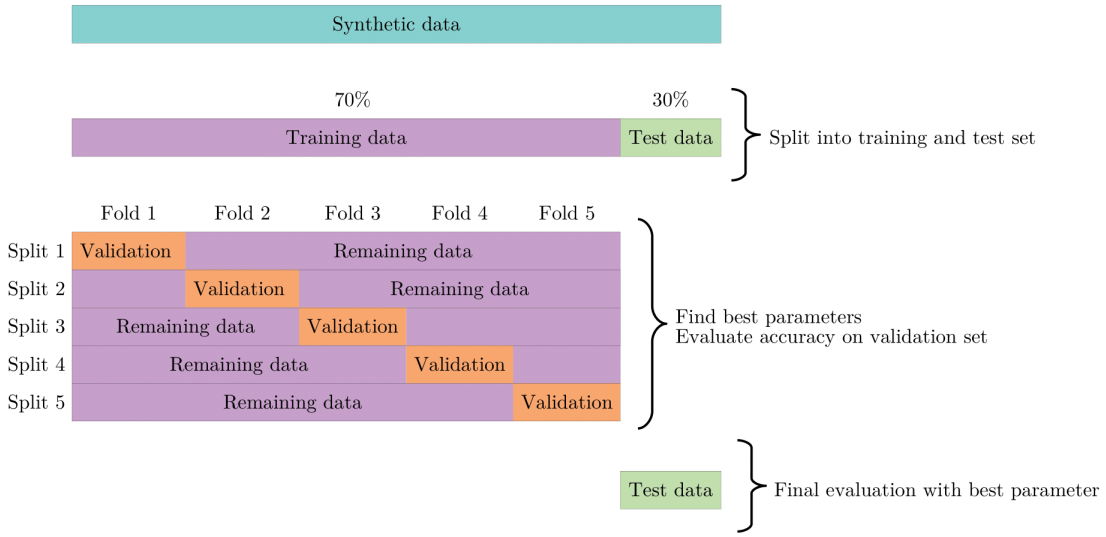

Figure 2.18: A diagram illustrating the process of training and evaluating the ML algorithm. The synthetic data were randomly split into a training (70%) and test set (30%), where the test data were set aside for the final evaluation of the algorithm. To find the k parameter with the highest accuracy, a grid-search and five-fold cross validation approach was used. The diagram was adapted from the `sklearn` User Guide[42].

The ML algorithm was then trained with $k = 4$ and it was also weighted with distance so that the neighbours that were closer counted more towards the classification. The final accuracy of the algorithm was evaluated by using the test data and an accuracy of 92% was achieved. Additionally, a normalised confusion matrix was generated using `sklearn.metrics.confusion_matrix` to visually evaluate the accuracy of the trained algorithm. The confusion matrix is shown in Figure 2.19. The values on the diagonal indicates when the algorithm classified the object correctly and on the off-diagonal when the classification was incorrect. Based on the test data, the confusion matrix shows that the algorithm can successfully classify 96% of the S-complex objects. The remaining 4% of the data were incorrectly classified by the algorithm as part of the X-complex or V-

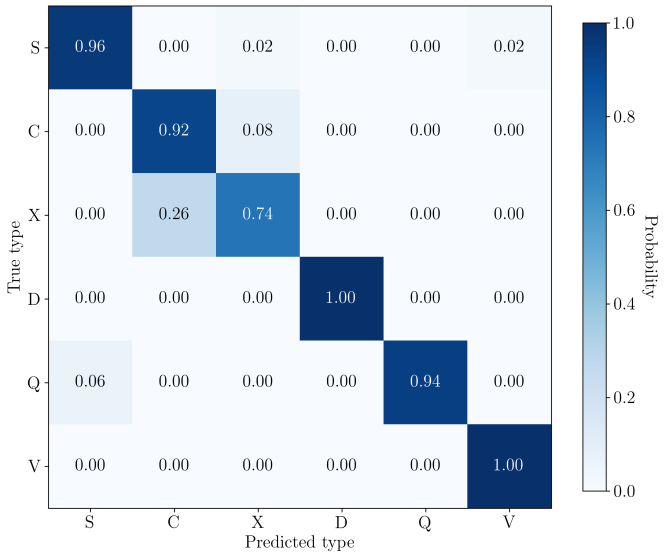

Figure 2.19: The confusion matrix demonstrating the accuracy of the ML algorithm, based on the test data. The x-axis shows the classification predicted from the algorithm and the y-axis the known classification of the object in the test data. Each block shows the probability, which is also indicated through the colour bar. The values on the diagonal shows the probability of a correct classification, therefore higher values means a better performance of the algorithm. The confusion matrix shows that, based on the test data, the algorithm can correctly classify 96% S-complex, 92% C-complex, 74% X-complex, 94% Q-type and 100% D- and V-type asteroids.

[42] https://scikit-learn.org/stable/modules/cross_validation.html

type. It also shows that the algorithm can successfully classify the D-, Q- and V-type asteroids, based on the test data, but it is not as good at differentiating the C- and X-complex.

The trained algorithm was also used to generate decision boundaries separating each taxonomic class. These decision boundaries with the respective synthetic colours are plotted in Figure 2.20a. The trained algorithm in combination with the measured g′−r′ and r′−i′ colours were used to calculate the most probable taxonomy of each target. Similar to Erasmus et al. (2017, 2018, 2019) and Mommert et al. (2016, 2020), a Monte-Carlo approach was used to include the colour uncertainties in the taxonomic determination. This was done by generating 10 000 random colours with a Gaussian distribution within 1σ of the measured colour uncertainties of each target. The random colours were then classified with the trained ML algorithm. The probability that the target was either part of the S-, C- or X-complex, or the D-, Q- or V-type, was calculated by tallying the number of classifications of the random colours in each taxonomy. This process is illustrated for two targets in Figure 2.20b. A target was assigned a distinct classification if it had a taxonomic probability of more than 50%. The taxonomic probabilities of all the objects observed in this project are shown and discussed in Section 3.2 of Chapter 3.

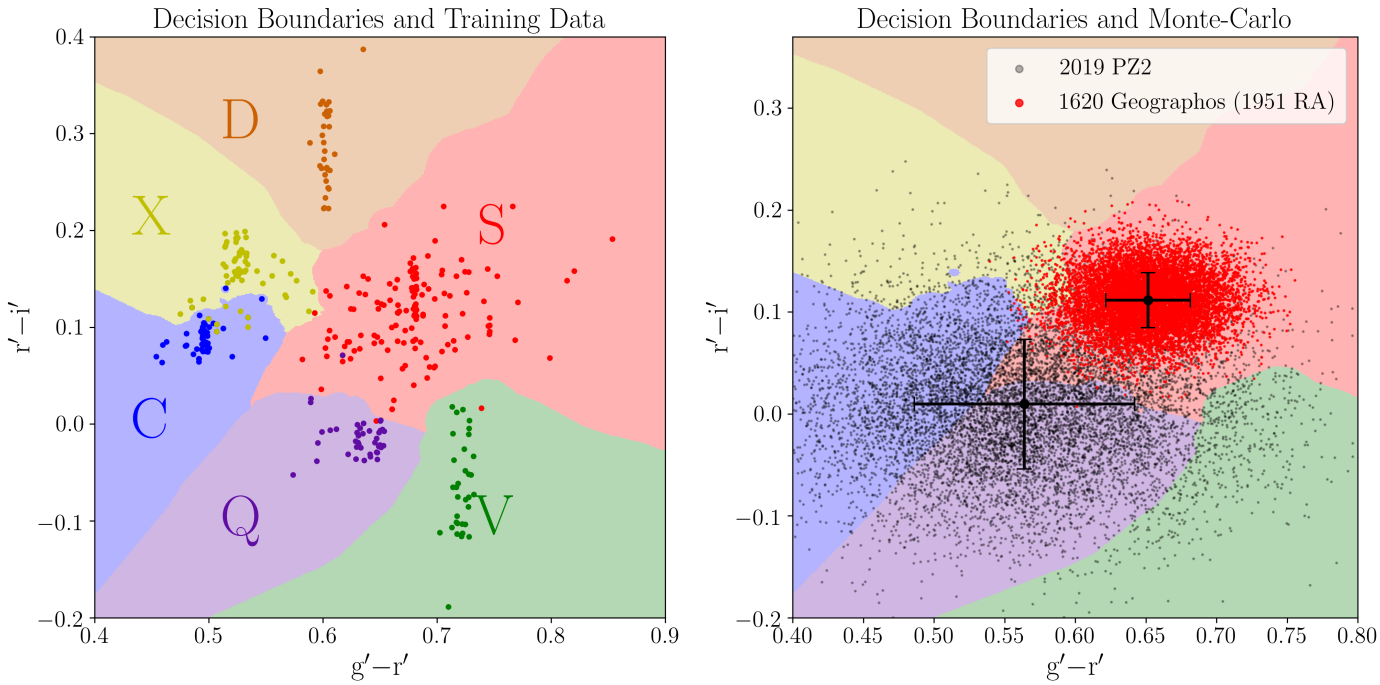

(a) Decision boundaries and synthetic colours.

(b) Decision boundaries and 10 000 random colours.

Figure 2.20: (a) Shown are the synthetic data, generated from MITHNEOS and average reflectance spectra for the S- (red), C- (blue) and X-complex (yellow), and the D- (orange), Q- (purple) and V-type (green) asteroids. The decision boundaries, separating the taxonomies and generated with the trained ML algorithm, are also shown. (b) The decision boundaries from (a) with 10 000 randomly generated colours, following a Gaussian distribution within 1σ of the measured colour uncertainties for two of the targets. The random colours were used to calculate the taxonomic probabilities. For example, for 2019 PZ2, about 21% of the random colours fall within the S-complex zone, 21% in the C-complex, 3% in the X-complex, 42% in the Q-type, 5% in the V-type and less than 1% in the D-type zone. Therefore this target remains unclassified.

2.6 Rotation period extraction

The multi-band (g′, r′ and i′) light curve of each target was also used to extract the rotation period of the asteroid since the reflected sunlight (i.e., brightness) of a non-spherical object will change as the exposed surface area varies under rotation. The rotation period is the time it takes the asteroid to rotate once on its axis. For a non-spherical body, this will result in two peaks and two troughs in the light curve. Therefore the rotation period is twice the light curve period. The light curve period could only be fully resolved if the observation period of the target exceeded that period.

To successfully extract the periods in the light curve only due to the rotation of the asteroid, other flux variations because of observing geometries had to be eliminated first. For instance, an asteroid will become brighter as it approaches an observer (i.e., Earth in this case) and also when the phase angle of the asteroid changes from ∼90° to 0°. When observing distant objects like trans-Neptunian objects or even MBAs for a couple of hours, these effects can be small and are often ignored because the observing geometry does not change much over a few hours or days. However, the observing geometry for a close-approaching asteroid can drastically change over the course of a day. For completeness and to ensure that these effects are accounted for during the observations in this project that often span a few hours (or days), both of these effects were corrected for using the formulation developed by Bowell et al. (1989) and summarised in Dymock (2007). Additionally, to change the observations to the time frame of the asteroid, the time it took the light to travel from the asteroid to the observer (i.e., light-time) were subtracted from the timestamps of all the data. The light-time for each target at every timestamp were obtained from the Horizons service.

The brightness variation due to the asteroid-observer distance were removed by calculating the reduced magnitude, H(α), for each filter band using equation 2.8 (Dymock, 2007), where V is the apparent magnitude (i.e., the g′, r′ or i′ data points in this project), D is the distance between the asteroid and the Sun and Δ is the distance between the asteroid and the Earth.

$$\mathrm{H}(\alpha) = \mathrm{V} - 5\log(D\Delta) \tag{2.8}$$

The phase angle effect was removed by converting the reduced magnitudes to the absolute magnitudes (H_g, H_r and H_i), following Dymock (2007). The absolute magnitude (H) is the magnitude of an asteroid if it was placed at the hypothetical geometry of 1 AU from the Earth and the Sun and at zero phase angle (α). It was calculated through equation 2.9, where H(α) is the reduced magnitude and G is the slope parameter. G is a function of the taxonomic type, but for most asteroids the taxonomy is unknown and an assumed value of 0.15 is used. The constants $\varphi_1(\alpha)$ and $\varphi_2(\alpha)$ were calculated using equation 2.10, where $i = 1$ or 2, $A_1 = 3.33$, $A_2 = 1.87$, $B_1 = 0.63$ and $B_2 = 1.22$.

$$\mathrm{H} = \mathrm{H}(\alpha) + 2.5\log\left[(1-\mathrm{G})\varphi_1(\alpha) + \mathrm{G}\varphi_2(\alpha)\right] \tag{2.9}$$

$$\varphi_i(\alpha) = \exp\left\{-A_i\left(\tan\frac{1}{2}\alpha\right)^{B_i}\right\} \tag{2.10}$$

Equation 2.9 is only valid for phase angles smaller than 120°, but in this project the targets were all observed at phase angles between 6° and 80°. The uncertainty in H was just the uncertainty in the observed magnitudes, since D, Δ, and α are all constants and G is only a function of taxonomic type.

After calculating the respective absolute magnitudes, a densely sampled light curve was formed with all of the data points of each target by shifting the H_g- and H_i-magnitudes with the $g'-r'$ and $r'-i'$ colours, respectively, to normalise H_g and H_i to H_r. The uncertainties in the shifted measurements were calculated as the root-sum-square of the measurement and the respective colour. The data for the targets that were observed on two consecutive nights were also combined into one light curve.

In order the extract the light curve period of each target, the `astropy` implementation of the Lomb-Scargle (Lomb, 1976; Scargle, 1982) periodogram were used through the `autopower()` method. The Lomb-Scargle periodogram searches for periods based on a least-squares spectral analysis and is especially useful in data that were unevenly sampled (VanderPlas, 2018). The search for the light curve period was limited to periods shorter than the full observation period or using published rotation periods (e.g., (454177) 2013 GJ35). Photometric measurement uncertainties were also included in the periodogram calculation and 30 samples per peak were used. If there was a distinct peak in the periodogram, the light curve was folded at this peak period to confirm that the light curve period could be resolved. Since the periodogram peaks do not follow a Gaussian distribution and the full width at half maximum (FWHM) does not accurately represent the uncertainty in the measured period (VanderPlas, 2018), the light curve period was calculated instead as the median of the period peak and the uncertainty was calculated as the upper and lower quartiles of the period peak. The confidence in the peak signifying a real periodicity in the data were further expressed by calculating the false alarm probability, using the `false_alarm_probability()` method.

The rotation period of the target, with its respective upper and lower quartile, was calculated by doubling the light curve period. The amplitude of the light curve was also calculated, similarly to Erasmus et al. (2017), by subtracting the minimum and maximum values of a running mean of the phase-folded light curve with a window of 10 data points. The rotation periods and amplitudes for all of the objects observed in this project are shown and discussed in Section 3.3 of Chapter 3.

3 | Results and Discussion

3.1 Light curves

The light curves of two MBAs, 141 Lumen (A875 AA) and 175 Andromache (A877 TA), are shown in Figure 3.1. The light curves of the remaining five MBAs are shown in Figure A.1 of Appendix A. These MBAs were only observed to verify the methodology and to validate the results, and were therefore only observed for a shorter amount of time compared to the NEA observations ($\lesssim 1$ hour). The shorter observation periods were still sufficient to calculate the colours of the MBAs using the same methodology as for the NEAs. The light curves of four small NEAs are shown in Figure 3.2. The light curves of the remaining NEAs are in Figure B.1 of Appendix B. Each light curve shows the calibrated photometry, extracted with PP from the reduced observing data, in three filters: g′, r′ and i′, plotted in green diamonds, red circles, and purple squares, respectively. The g′−r′ and r′−i′ colours were extracted from these light curves, as explained in Section 2.5 of Chapter 2, and is shown in the top-right corner of each plot.

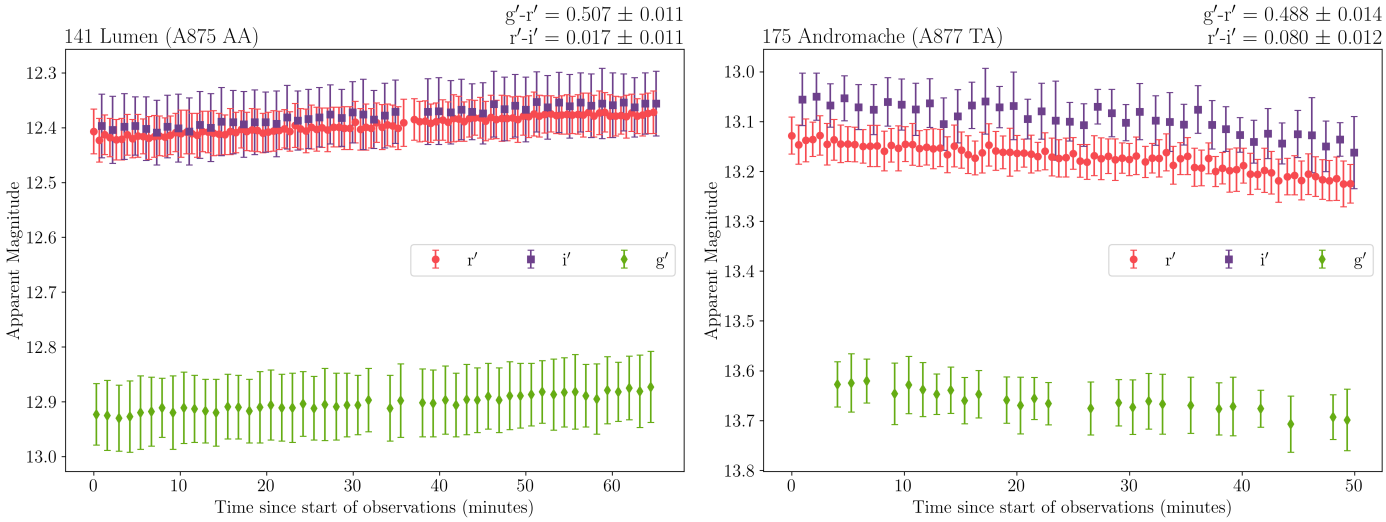

(a) 141 Lumen (A875 AA)

(b) 175 Andromache (A877 TA)

Figure 3.1: The light curves (apparent magnitude as a function of time) of two MBAs observed in this project to verify the methodology and to validate the results. (a) Plotted is a ∼60 minute light curve of 141 Lumen (A875 AA), and (b) a ∼50 minute light curve of 175 Andromache (A877 TA). The apparent magnitude is indicated as green diamonds for the g′-filter, red circles for the r′-filter and purple squares for the i′-filter. The g′−r′ and r′−i′ colours are also displayed in the top-right corner of each plot. The measured colours of these two targets, in addition to the colours of the NEA 1620 Geographos (1951 RA), were used to calibrate the synthetic colours, as described in Section 2.5 of Chapter 2. The light curve of 1620 Geographos (1951 RA) is shown in Figure B.1a of Appendix B and the remaining MBA light curves in Appendix A.

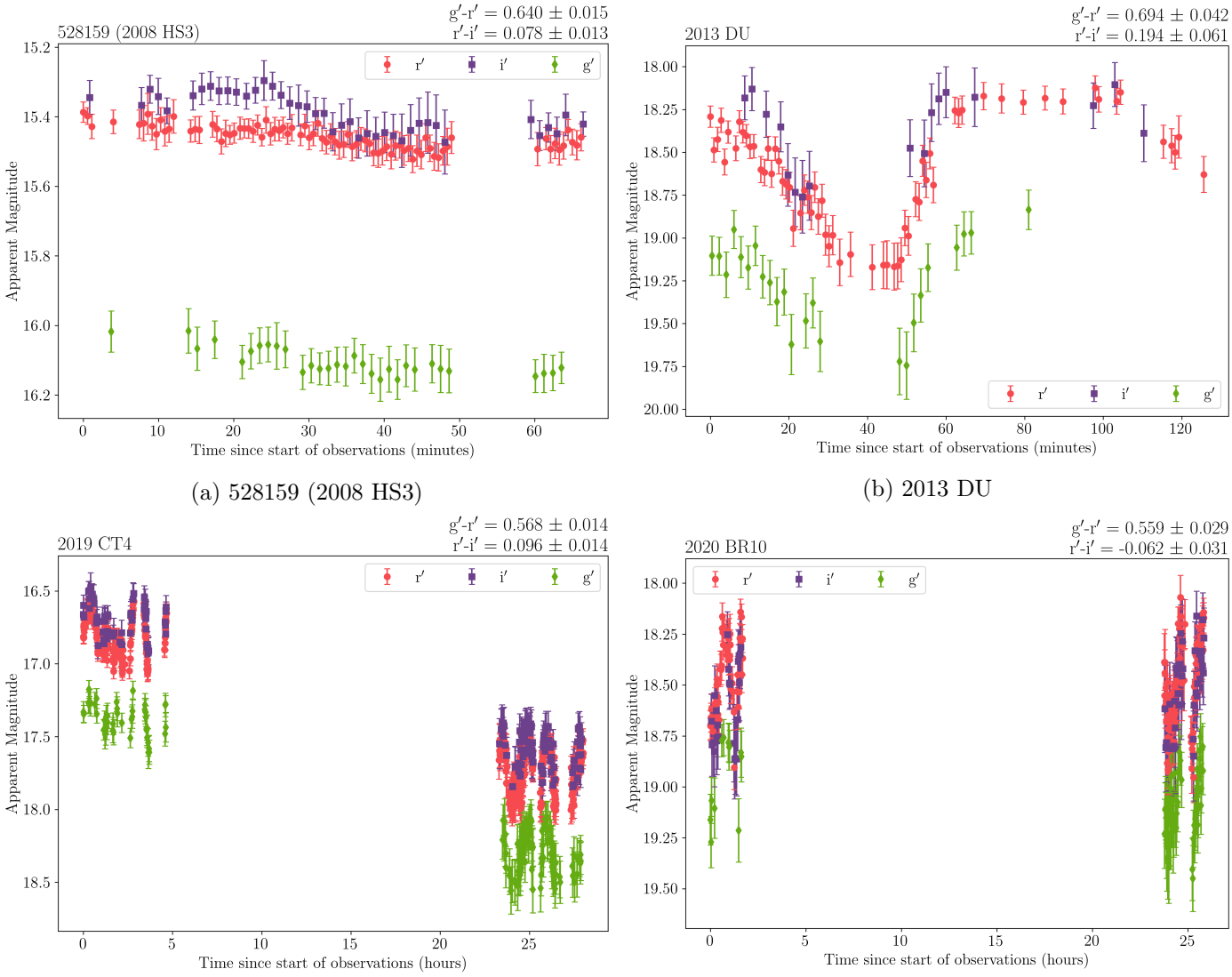

Figure 3.2: The light curves (apparent magnitude as a function of time) of four small NEAs. Plotted are the light curves of (a) 528159 (2008 HS3) and (b) 2013 DU that were only observed on one night. (c) and (d) shows the light curves of 2019 CT4 and 2020 BR10 that were observed on two consecutive nights. The apparent magnitude is indicated as green diamonds for the g′-filter, red circles for the r′-filter and purple squares for the i′-filter. The g′−r′ and r′−i′ colours are also displayed in the top-right corner of each plot. The light curves of the other NEAs are shown in Figure B.1 of Appendix B.

3.2 Taxonomic classification

The taxonomic probability of each target was calculated using the colours extracted from the light curves, in combination with the ML method described in Section 2.5 of Chapter 2. A summary of the taxonomic classifications is shown in Table 3.1. The g′−r′ and r′−i′ colours, as well as the a^* values for each target are also included in the table. In Figure 3.3 and 3.4, a visual representation of the derived taxonomic classification are shown for the MBAs and NEAs, respectively.

Figure 3.3a and 3.4a shows a colour-colour plot of r′−i′ vs g′−r′, with the decision boundaries generated by the ML algorithm superimposed. The targets are colour-coded according to their most probable classification. A class is assigned to the target if it has a taxonomic probability of more than 50% in a specific class. A threshold of 50% was decided as an appropriate level to make a judgement on a successful classification or not. The same threshold was used in Mommert et al. (2016) and Erasmus et al. (2017). The targets plotted in black remain unclassified as none of the probabilities are >50%. The taxonomic probabilities were calculated with a Monte-Carlo approach as described in Section 2.5 of Chapter 2. Figures 3.3b and 3.4b show similar plots to Figure 2.15 in Chapter 2, where the absolute magnitude of inner main-belt asteroids is plotted as a function of a^* from the supplementary data of Delbo' et al. (2017). The observed MBAs are plotted in Figure 3.3b and the NEAs in Figure 3.4b, where the targets were colour-coded according to their taxonomic classification determined by the ML algorithm. These plots are shown for completeness and to compare the ML classification with the expected a^* values.

Figure 3.3b and 3.4b also clearly show that, from the absolute magnitude, the MBAs in this study had much smaller H values compared to the sample in Delbo' et al. (2017, suppl.), which meant they were bright and suitable for validation data. Contrary to the MBAs, the NEAs in this study had much larger H values. As discussed in Chapter 1, NEAs are thought to have escaped from the inner main-belt, which means small MBAs should exist, but they are too faint to be observed from the Earth. This highlighted the benefit of the close proximity of NEAs and how the study of small NEAs can help in the understanding of the formation and evolution of the Solar System.

Using the ML method with the observed colours, the algorithm was able to successfully classify 6 out of the 7 MBAs to the same taxonomic classification that has been reported in the literature. This result further validates the classification method of this study. In this study, out of the 7 MBAs, 4 are classified as C-complex asteroids, 2 as S-complex asteroids and 1 as a V-type asteroid. The classifications also agree with the expected a^* values, as can be seen in Figure 3.3b and in Table 3.1. A positive a^* value indicates a redder asteroid (e.g., S, V) and a negative a^* value a bluer asteroid (e.g., C). However, it should be noted, that a^* alone could not differentiate between the S- and V-type asteroids. The separation between the two classes were only possible through the ML algorithm, which illustrates the power of the ML method over the simpler a^* method for classification.

Table 3.1: Colours and summary of the taxonomic classification.

Target	H[h] (mag)	Diameter[i] (m)	g′−r′ (mag)	r′−i′ (mag)	a^{*}[j] (mag)	Probabilities[k] S-complex	C-complex	X-complex	D-type	Q-type	V-type	Taxonomy[l]
NEAs												
1620 Geographos (1951 RA)	15.3	2300 - 5200	0.652 ± 0.030	0.112 ± 0.027	0.060 ± 0.020	**0.9807**	0.0008	0.0167	0.001	0.0003	0.0005	S
86667 (2000 FO10)	17.6	800 - 1800	0.633 ± 0.022	0.033 ± 0.020	0.008 ± 0.014	**0.7595**	0	0	0	0.2378	0.0027	S
481394 (2006 SF6)	19.9	280 - 620	0.610 ± 0.093	0.089 ± 0.069	0.013 ± 0.057	**0.5056**	0.1764	0.1429	0.03	0.0991	0.046	S
2007 YU56	22.1	100 - 230	0.651 ± 0.041	-0.039 ± 0.032	-0.008 ± 0.027	0.0575	0.0004	0	0	**0.7095**	0.2326	Q
358744 (2008 CR118)	18.9	440 - 990	0.566 ± 0.021	0.146 ± 0.021	-0.001 ± 0.012	0.0911	0.0868	**0.8079**	0.0142	0	0	X
528159 (2008 HS3)	21.6	130 - 280	0.640 ± 0.015	0.078 ± 0.013	0.035 ± 0.009	**1**	0	0	0	0	0	S
2010 AE30	23.6	51 - 110	0.575 ± 0.091	0.188 ± 0.038	0.026 ± 0.053	0.3095	0.0274	0.4759	0.1872	0	0	-
454177 (2013 GJ35)	15.8	1800 - 4100	0.557 ± 0.012	-0.041 ± 0.012	-0.093 ± 0.007	0	0	0	0	**1**	0	Q
2013 CW32	22.0	110 - 240	0.580 ± 0.007	0.061 ± 0.006	-0.027 ± 0.004	**0.9996**	0.0004	0	0	0	0	S
2013 DU	24.0	42 - 94	0.694 ± 0.042	0.194 ± 0.061	0.135 ± 0.031	**0.825**	0.0003	0.0047	0.1656	0.0004	0.004	S
515767 (2015 JA2)	21.1	160 - 360	0.688 ± 0.074	0.119 ± 0.039	0.096 ± 0.051	**0.8968**	0.0222	0.0603	0.0078	0.0028	0.0101	S
2019 AG7	25.5	21 - 47	0.541 ± 0.011	0.024 ± 0.010	-0.078 ± 0.006	0.2229	0.3503	0	0	0.4268	0	-
2019 CT4	24.4	35 - 78	0.568 ± 0.014	0.096 ± 0.014	-0.021 ± 0.008	0.3755	0.3702	0.2543	0	0	0	-
2019 EN	21.2	150 - 340	0.588 ± 0.037	0.098 ± 0.025	-0.003 ± 0.022	**0.5996**	0.2091	0.1878	0.0003	0.0032	0	S
2019 HV3	24.0	42 - 94	0.558 ± 0.053	-0.015 ± 0.040	-0.081 ± 0.029	0.0905	0.2017	0.0008	0	**0.6984**	0.0086	Q
2019 OM	22.6	80 - 180	0.641 ± 0.064	0.063 ± 0.030	0.029 ± 0.041	**0.7798**	0.0862	0.0165	0	0.0643	0.0532	S
2019 PZ2	19.8	290 - 650	0.564 ± 0.078	0.010 ± 0.064	-0.064 ± 0.044	0.2119	0.2882	0.0291	0.001	0.4199	0.0499	-
2019 SP3	26.2	15 - 34	0.662 ± 0.063	0.020 ± 0.033	0.028 ± 0.042	0.4476	0.0218	0.0009	0	0.2865	0.2432	-
2020 BR10	22.8	74 - 170	0.559 ± 0.029	-0.062 ± 0.031	-0.100 ± 0.016	0.0011	0.0139	0	0	**0.9838**	0.0012	Q
2020 HT2	22.5	84 - 190	0.642 ± 0.032	0.063 ± 0.035	0.030 ± 0.021	**0.8815**	0.0022	0.0095	0.0003	0.0866	0.0199	S
MBAs												
141 Lumen (A875 AA)	8.5	117 916	0.507 ± 0.011	0.017 ± 0.011	-0.111 ± 0.006	0.0007	**0.9746**	0	0	0.0247	0	C
175 Andromache (A877 TA)	8.4	94 532	0.488 ± 0.014	0.080 ± 0.012	-0.100 ± 0.007	0	**0.993**	0.007	0	0	0	C
270 Anahita (A887 TA)	8.8	51 400	0.673 ± 0.023	0.011 ± 0.035	0.034 ± 0.016	**0.5285**	0	0	0	0.2635	0.208	S
329 Svea (A892 FG)	9.6	81 057	0.519 ± 0.043	0.095 ± 0.043	-0.065 ± 0.023	0.1133	**0.571**	0.2866	0.0018	0.0273	0	C
383 Janina (A894 BC)	9.9	43 482	0.471 ± 0.017	0.053 ± 0.011	-0.127 ± 0.008	0	**1**	0	0	0	0	C
1273 Helma (1932 PF)	12.9	6 278	0.710 ± 0.048	-0.025 ± 0.030	0.051 ± 0.034	0.0804	0	0	0	0.2334	**0.6862**	V
1933 Tinchen (1972 AC)	13	4 508	0.720 ± 0.030	0.113 ± 0.028	0.122 ± 0.022	**0.9932**	0	0	0	0	0.0068	S

Notes:

[h] Absolute magnitude from https://ssd.jpl.nasa.gov/sbdb.cgi.

[i] Diameter range of NEAs obtained from https://cneos.jpl.nasa.gov/ca/. It was calculated from equation 1.1 with geometric albedos of 0.25 and 0.05. Diameters of MBAs obtained from https://ssd.jpl.nasa.gov/sbdb.cgi.

[j] $a^{*} = 0.89(g^{*} - r^{*}) + 0.45(r^{*} - i^{*}) - 0.57$ as explained in Chapter 2.

[k] Probabilities >50% are highlighted in bold.

[l] Taxonomic type with probability >50%.

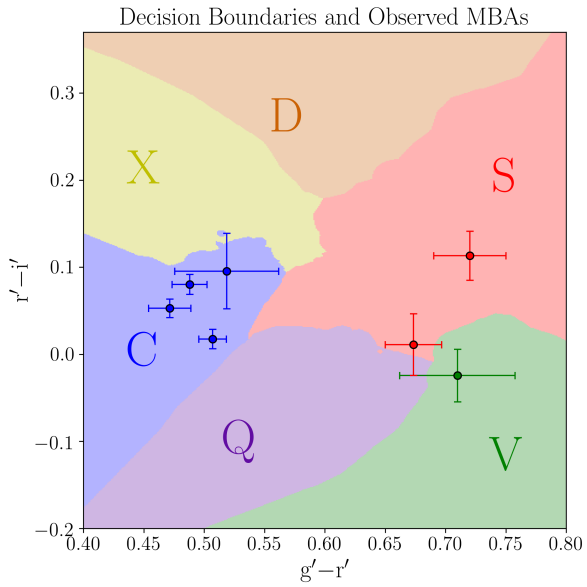

(a) MBAs classified with the ML algorithm.

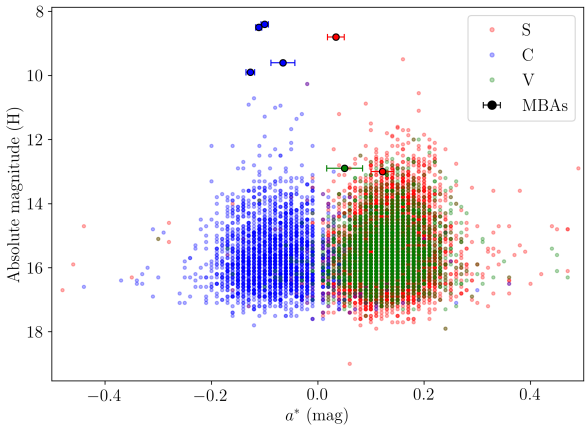

(b) MBAs classified with the ML algorithm, plotted with data of inner main-belt asteroids from Delbo' et al. (2017, suppl.).

Figure 3.3: The taxonomic classification of the seven MBAs observed in this project. (a) Colour-colour plot of r′−i′ vs g′−r′. The decision boundaries generated by the ML algorithm are plotted for the taxonomic types considered in this project: S- (red), C- (blue) and X-complex (yellow), and D- (orange), Q- (purple) and V-type (green). The colours of the MBAs are plotted and colour-coded according to their most probable taxonomic type (>50% taxonomic probability). If none of the taxonomic probabilities were >50%, the target remained unclassified and is plotted in black (none of the MBAs). (b) Plotted is the absolute magnitude (H) as a function of the a^* parameter, similar to Figure 2.15, but here only three taxonomies are shown corresponding to the distinct taxonomies of the MBAs in this study, i.e., S (red), C (blue) and V (green). The MBAs of this study are also plotted and colour-coded according to the most probable taxonomy determined by the ML algorithm.

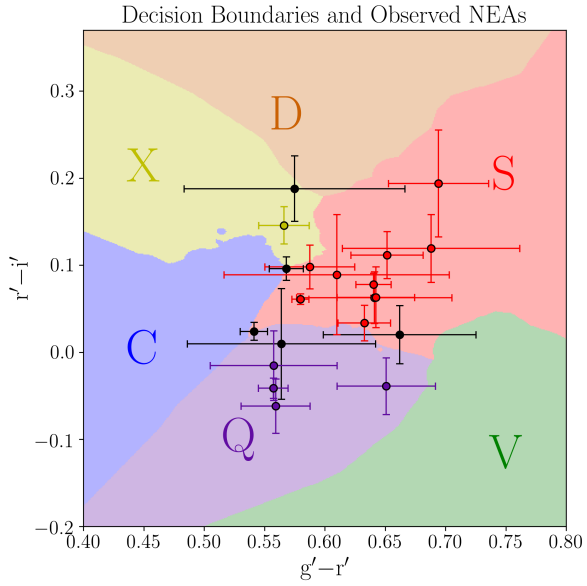

(a) NEAs classified with the ML algorithm.

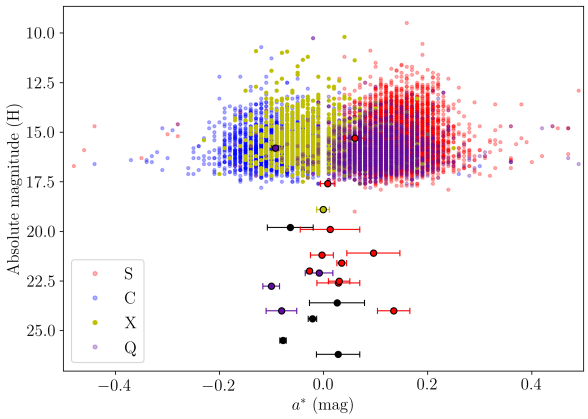

(b) NEAs classified with the ML algorithm, plotted with data of inner main-belt asteroids from Delbo' et al. (2017, suppl.).

Figure 3.4: The same as Figure 3.3, but here the taxonomic classification of the 20 NEAs are shown. In (b), only four taxonomic types are plotted corresponding to the distinct taxonomies of the NEAs in this study: S-type (red), C-type (blue), X-type (yellow) and Q-type (purple).

In this study, MBA 141 Lumen and MBA 175 Andromache are both classified as C-complex asteroids with ML probabilities of almost 100%. These classifications are in agreement with Bus and Binzel (2002) who classified 141 Lumen as a Ch-type asteroid and 175 Andromache as a Cg-type asteroid based on reflectance spectroscopy. Both of these classes are part of the C-complex. Belskaya et al. (2017) also classified 141 Lumen as a Ch-type asteroid from polarimetry and according to the Bus-DeMeo classification scheme. MBA 270 Anahita is classified as an S-complex asteroid with a probability of 53%. This agrees with Lazzaro et al. (2004) who classified it as an S-type asteroid from spectroscopic data. The MBA 329 Svea was classified as a C-type asteroid by Lazzaro et al. (2004) as well as Morate et al. (2019), which is in agreement with the results in this study where it is classified as a C-complex asteroid with a probability of 57%.

MBA 383 Janina is classified as a C-complex asteroid with a probability of 100% in this study. It was also classified as a C-type asteroid by Erasmus et al. (2020) (with a probability of 91%) based on the $c-o$ colour from ATLAS data, however Bus and Binzel (2002) classified it as a B-type asteroid from optical reflectance spectra. The $c-o$ colour could only be used to differentiate between S- and C-type asteroids and therefore a B-type asteroid would be misclassified as a C-type asteroid in that study. In this study, the B-type classification was also not included as a possibility due to a lack in training data and therefore the C-complex classification here does not rule out a B-type taxonomy as reported by others.

Erasmus et al. (2020) also classified the MBAs 1273 Helma and 1933 Tinchen as S-type asteroids, both with probabilities around 86%, and they identified both as part of the Vesta family. The Vesta family is a known V-type family. Similarly to 383 Janina, V-type asteroids could also be misclassified as S-types with only the $c-o$ colour since a single colour is not sufficient to distinguish between the S- and V-type taxonomies. Additionally, both of these targets were classified by Xu et al. (1995) as V-type asteroids based on optical reflectance spectra. In this study, 1273 Helma is classified as a V-type asteroid with a probability of 69%, but 1933 Tinchen is classified as an S-complex asteroid with a probability of 99%. As shown in Figure 2.20a of Chapter 2, there were only 35 V-type asteroids in the training data of the ML algorithm and most of them were generated from the Bus-DeMeo average V-type spectra and were therefore close to each other in the colour-colour plot. With more training data, the boundary between the S-complex and V-type asteroids could be defined better and 1933 Tinchen could possibly have a higher V-type probability.

In summary, the MBA classifications determined with the high-quality MBA photometry data collected in this study, in combination with the methodology explained in Section 2.5 of Chapter 2, are in excellent agreement with the literature. This gives confidence in the NEA results that follow.

Out of the 20 NEAs reported in this study, 10 are classified as S-complex, 4 as Q-type asteroids and 1 as an X-type asteroid by the ML algorithm. The remaining 5 targets do not have a taxonomic probability >50% in any of the taxonomic classes and remain unclassified in this study. These results can also be seen in Figure 3.4. The targets that are unclassified are mainly situated on the boundaries between the different taxonomic types. Therefore the ML algorithm struggles to definitively determine a concrete taxonomic type, even when the uncertainty in the measured colours are small (e.g., 2019 AG7 and 2019 CT4). More observations in other photometric bands or reflectance spectroscopy will be needed to determine the taxonomic class of these NEAs, however the probabilistic taxonomic results (see Table 3.1) can perhaps at least exclude some taxonomic types for these unclassified targets.

Only four NEAs studied in this project have previously reported taxonomic classes in the literature and were successfully classified by the ML algorithm. New taxonomic classes are reported for the remaining 11 targets. The NEAs with reported classes are 1620 Geographos (1951 RA), 86667 (2000 FO10), 481394 (2006 SF6) and 528159 (2008 HS3). Out of these four NEAs, only 2008 HS3 has a diameter less than 300 m and only 2000 FO10 is not considered a potentially hazardous asteroid (PHA).

In this project, 1620 Geographos is classified as an S-complex asteroid with a probability of 98%. This result agrees with Bus and Binzel (2002) and Binzel et al. (2019) who classified it as an S-type asteroid from optical and near-infrared reflectance spectra. It was also classified as an S-type by Dandy et al. (2003) from multi-band photometry. Dandy et al. (2003) used the Tholen classification scheme and Binzel et al. (2019) used the Bus-DeMeo classification scheme. 2000 FO10 was classified by Binzel et al. (2019) as an Sq-type asteroid and by Carry et al. (2016) as an S-type asteroid based on SDSS photometry in four filters (g′, r′, i′, z′). The result in this study agrees as this target is classified as an S-complex asteroid with a probability of 71%, but it also has a 29% probability of being a Q-type asteroid. Hasegawa et al. (2018) classified 2006 SF6 as either an S-, A- or D-type asteroid based on the Tholen classification scheme from photometric observations in four filters (B V R I). In this project, it is classified as an S-complex asteroid with a probability of 51%. The final target, 2008 HS3, was classified as a Q-type asteroid by Binzel et al. (2019), but here it is classified as an S-complex asteroid with 100% probability. This difference could be because Binzel et al. (2019) classified the spectra based on mostly near-infrared spectra (wavelength between 0.8 and 2.45 microns) and in this project it was only done based on optical data in three filters covering a range between approximately 0.4 and 1.1 microns. The S-complex and Q-type spectra are also very similar, therefore the results of this work are not in disagreement with Binzel et al. (2019).

Figure 3.4 gives an indication of the taxonomic distribution of the NEAs in this project. An overwhelming amount of NEAs are classified as S-complex and Q-type asteroids and only one is classified as an X-complex asteroid. It should be noted that for the S-complex and X-complex asteroids, the ML classification agrees with the expected a^* values, but the NEAs classified as Q-type asteroids by the ML algorithm all have negative a^* values (see Table 3.1). If classification relied solely on a^*, these NEAs would have been classified as, and resulted in an overestimation of C-type asteroids. The power of the ML technique over the a^* classification is illustrated here again. C-complex and Q-type asteroids can be differentiated with two colours and the ML algorithm.

Even though the discrete taxonomic classes of the NEAs in this project suggest an overwhelming fraction of silicate-based asteroids, Erasmus et al. (2017) showed that a more statistically correct way to study the taxonomic distribution is to calculate the fractional compositional distribution. The fraction is calculated by adding the probabilities together in each taxonomic class, which are given in Table 3.1. The fractional compositional distribution is given in Figure 3.5 for two size ranges. The diameters were estimated by using an assumed geometric albedo of 0.2. The distribution in this study was also compared to similar data from Erasmus et al. (2017) and Mommert et al. (2016) and this is also shown in Figure 3.5. Erasmus et al. (2017) only considered the S, C, X and D classes. Mommert et al. (2016) only considered the S, D and V classes and they combined the C and X class compositions. All of the data from Erasmus et al. (2017) were used to calculate the compositional fractions, but only the reliable data from Mommert et al. (2016) were used, which they stated as those with colour uncertainties ≤ 0.3 magnitudes. This means Mommert et al. (2016) only considered the

brightest targets, therefore introducing a bias that is in favor of larger asteroids, as well as asteroids with higher albedos like S-complex asteroids. Poisson uncertainties were also included since all of the sample sizes were small.

In the large size range ($14 \leq H < 20$), the fraction of S-complex asteroids in this study was ∼42% and in the small size range ($20 \leq H < 29$) it was ∼54%. Within uncertainty, the results agree across the size ranges and with the results in Erasmus et al. (2017) and Mommert et al. (2016). It is also similar to the fraction of S-type asteroids obtained in Navarro-Meza et al. (2019), where they considered a size range of ∼30−850 m. It should be noted that in this project, for the large size range, only six NEAs contributed to the distribution since this study was mainly focused on observing and classifying small NEAs.

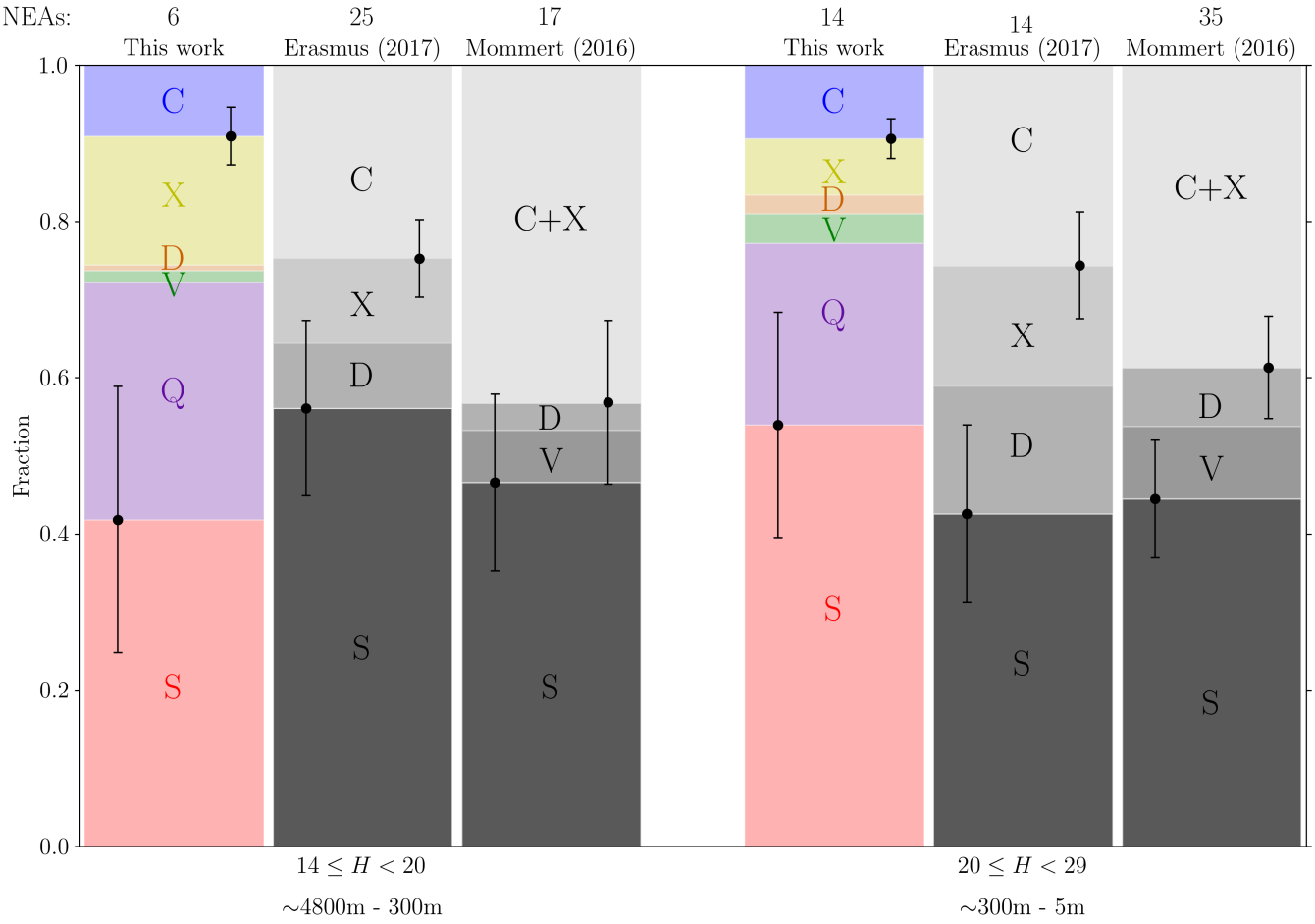

Figure 3.5: The fractional compositional distribution for the six taxonomic classes considered in this project: S-complex (red), C-complex (blue), X-complex (yellow), D-type (orange), Q-type (purple) and V-type (green). The distribution is plotted for two absolute magnitude (and therefore size) ranges. An estimated diameter range is given, assuming a geometric albedo of 0.2. Shown with the results of this study is similar data from Erasmus et al. (2017) and Mommert et al. (2016) in grey. The number of NEAs in each distribution is given at the top. Because of the small sample sizes, Poisson uncertainties are shown for the S- and C-complex.

The fraction of V- and D-type asteroids in this study is less than the fractions in Mommert et al. (2016) and Erasmus et al. (2017) for the small and large size ranges. However, the fractions are still less than 10% which is also consistent with other studies such as Carry et al. (2016) and Perna et al.

(2018). D-type asteroids are mostly found in the outer main-belt and the small fraction of D-types are in favour of the models suggesting that NEAs originate in the inner main-belt (Dandy et al., 2003).

The fraction of Q-type NEAs in this study was about 30% and 23% for the large and small size ranges, respectively. Binzel et al. (2015) stated that 20% of near-Earth objects (which includes near-Earth asteroids and comets) are Q-types, which is slightly lower than the fraction in this study. The fraction of C- and X-complex asteroids in this study, for both the small and large size ranges, was significantly less compared to the results in Erasmus et al. (2017), Mommert et al. (2016) and Navarro-Meza et al. (2019).

As discussed in Chapter 1, Q-type asteroids have similar spectra to the most common meteorite: ordinary chondrites. Binzel et al. (2015, 2019) also showed that the surface of a Q-type asteroid can change, transforming it into an S-type asteroid, after close encounters with the Earth and Venus. Therefore S- and Q-type asteroids are made of the same material, the one is just weathered and the other unweathered. Binzel et al. (2015) suggested that ordinary chondrites originate from S- *and* Q-type asteroids and the results of this study agree with that. The combined fraction of S- and Q-type asteroids are similar to the fraction of ordinary chondrites in meteorite falls ($\sim$80%). The sample in this project was small and more data will be needed to confirm this result. Neither Erasmus et al. (2017) nor Mommert et al. (2016) included the Q class in their classification. Because of this, they found a discrepancy between the most observed NEA (S-type) and the most common meteorite. However, it is possible that Erasmus et al. (2017) and Mommert et al. (2016) are overestimating the fraction of C-complex asteroids and if they include the Q class in their classification, they would arrive at the same result as this study.

It should be noted that the results of this study also includes an observation bias. Because the study focused on small NEAs, the brightest NEAs, with the highest albedo, were targeted. C-complex asteroids are fainter than silicate-based asteroids like S-, Q- or V-types. The average albedo of an S-type and C-type asteroid is about 0.26 and 0.13, respectively. Q-type asteroids have a slightly higher albedo of almost 0.3 (Thomas et al., 2011). This means there is an overestimation in S-complex and Q-type asteroids and an underestimation in C- and X-complex asteroids.

3.3 Rotation periods

For a rotation period (2× light curve period) to be extracted, a target had to be observed for a duration of at least one light curve period. None of the MBAs observed in this project had light curve periods that could be resolved within the observation period, but they were not the focus of this study. They were only observed for about 60 minutes or less to obtain accurate colour information and thereby evaluate the validity of the classification method, since they also had published taxonomies based on observed spectra. This was discussed in Section 3.2. All of the MBAs reported here have rotation periods longer than about 3.5 hours, as can be seen in Table 3.2, which lists the rotation periods of the MBAs from previous research studies. The observations in this study confirm these relatively long reported rotation periods since no periodic signal is visible in any of the light curves presented here (see Figures 3.1 and A.1) which only span a maximum of 1 hour.

Table 3.2: Rotation periods from previous research studies of the MBAs observed in this project.

Main-belt asteroid (MBA)	Rotation period from previous research (hours)	Reference(s)
141 Lumen (A875 AA)	19.87	e.g., Koff (2006); Pál et al. (2020)
175 Andromache (A877 TA)	7.11	Blanco et al. (2000)
270 Anahita (A887 TA)	15.05	e.g., Durech et al. (2016)
329 Svea (A892 FG)	22.80	Marciniak et al. (2015, 2018)
383 Janina (A894 BC)	4.64	Clark (2006)
1273 Helma (1932 PF)	6.09	e.g., Waszczak et al. (2015); Erasmus et al. (2020)
1933 Tinchen (1972 AC)	3.67	e.g., Waszczak et al. (2015); Pál et al. (2020)

Nine out of the 20 NEAs were observed for long enough in order to resolve a light curve period. In Figure 3.6, three plots are shown for two targets: 2013 CW32 (3.6a) and 2020 HT2 (3.6b). The same plots are shown for the remaining seven targets in Figure C.1 of Appendix C. In the first plot, the absolute magnitudes in all three filters (g′, r′ and i′) were combined into one light curve, where the g′ and i′ data were normalised to the r′ data by shifting them with the g′−r′ and r′−i′ colours, respectively. The second plot shows the Lomb-Scargle periodogram, where the strongest peak is indicated with a red line. The light curve period was extracted as the median of the peak and the uncertainty in the period was given by the lower (Q1) and upper (Q3) quartiles of the peak. A phase-folded light curve is shown in the last plot, where the data were folded at the median rotation period (2× median light curve period). The red line is showing a running average with a window of 10 data points to guide the eye and from which the amplitude was calculated. Table 3.3 gives the amplitude as well as the median, and lower and upper quartile rotation period for each of the nine targets with a resolved light curve period. The false-alarm probability (FAP) of the highest peak in the periodogram is also given in Table 3.3 as an additional measure of the confidence in the periodicity at the specific period.

Three NEAs in Table 3.3 are indicated with an asterisk (*): 454177 (2013 GJ35), 2013 DU and 2019 SP3. The light curve, periodogram and phase-folded light curve for each is given in Figure C.1c, C.1b and C.1f of Appendix C, respectively. As can be seen in the periodograms, the highest peaks are not well defined. This could be due to either a sparse data set or because the observations did not cover the full rotation period. However, the folded light curves show evidence of a possibly resolved rotation with the appearance of troughs and peaks. 2013 GJ35 was studied by Warner and Stephens (2019a)

over 12 nights in the beginning of January 2019 (around the same observation time as in this study, see Table 2.1). In their study, they identified it as a possible very wide binary with two extracted periods: a primary period of 49.75 ± 0.02 hours and a secondary period of 2.8169 ± 0.0001 hours. The secondary period agrees with the period obtained in this study. They also obtain an amplitude of 0.05 for the secondary period, which agrees within 2σ of the amplitude calculated in this study. The FAP of 2019 SP3 is about 10^{-8} which means it is possible that the extracted period is due to a periodicity in the data. Even though its folded light curve show some rotation, the data is sparse and the uncertainties are large enough ($\sim$0.1 mag) to mask a low amplitude periodicity. Better quality data over longer observation periods will be needed to confirm these extracted rotation periods.

Table 3.3: Rotation periods and amplitudes of the NEAs.

Target	H[m] (mag)	Diameter[n] (m)	Rotation period (hours) Q1	Median	Q3	False Alarm Probability (FAP)	Amplitude (mag)
Periods extracted from a Lomb-Scargle periodogram							
2010 AE30	23.6	51 - 110	1.332	1.341	1.351	2.86E-17	0.81 ± 0.01
454177 (2013 GJ35)*	15.8	1800 - 4100	2.460	2.807	3.269	1.32E-24	0.14 ± 0.06
2013 CW32	22.0	110 - 240	2.277	2.302	2.328	<2.58E-314	0.53 ± 0.06
2013 DU*	24.0	42 - 94	3.263	3.539	3.866	5.51E-29	0.91 ± 0.12
2019 CT4	24.4	35 - 78	2.845	2.894	2.945	3.28E-30	0.44 ± 0.10
2019 HV3	24.0	42 - 94	5.275	5.410	5.553	1.09E-31	0.73 ± 0.11
2019 SP3*	26.2	15 - 34	0.448	0.459	0.471	2.04E-08	0.23 ± 0.13
2020 BR10	22.7	74 - 170	2.260	2.283	2.307	5.22E-47	0.58 ± 0.10
2020 HT2	22.5	84 - 190	0.276	0.285	0.296	2.75E-10	0.34 ± 0.10
Lower limit to period							
1620 Geographos (1951 RA)	15.3	2300 - 5200		>1.691		-	-
86667 (2000 FO10)	17.6	800 - 1800		>5.139		-	-
2019 EN	21.2	150 - 340		>6.070		-	-

Notes:
[m] Absolute magnitude from https://ssd.jpl.nasa.gov/sbdb.cgi.
[n] Diameter range of NEAs obtained from https://cneos.jpl.nasa.gov/ca/. It was calculated from equation 1.1 with geometric albedos of 0.25 and 0.05.

Eight NEAs in Table 3.3 with an extracted rotation period have an absolute magnitude ≤ 22, which corresponds to a diameter of approximately 120 m assuming a geometric albedo of 0.2. As demonstrated in Warner et al. (2009) and Thirouin et al. (2018), asteroids with absolute magnitudes less than 22, typically have rotation periods of about 5 hours or less. The results of this thesis are consistent with this. Three of these small NEAs (2010 AE30, 2019 SP3 and 2020 HT2) also have rotation periods shorter than the 2.2 hour spin barrier and are considered fast rotators. Because of their short rotation periods and small sizes, they are probably rigid pieces of rock instead of rubble piles. Their light curves, periodograms and phase-folded light curves are given in Figures C.1a, C.1f and 3.6b, respectively. 2020 HT2 (H = 22.5) has the fastest rotation period of about 17 minutes.

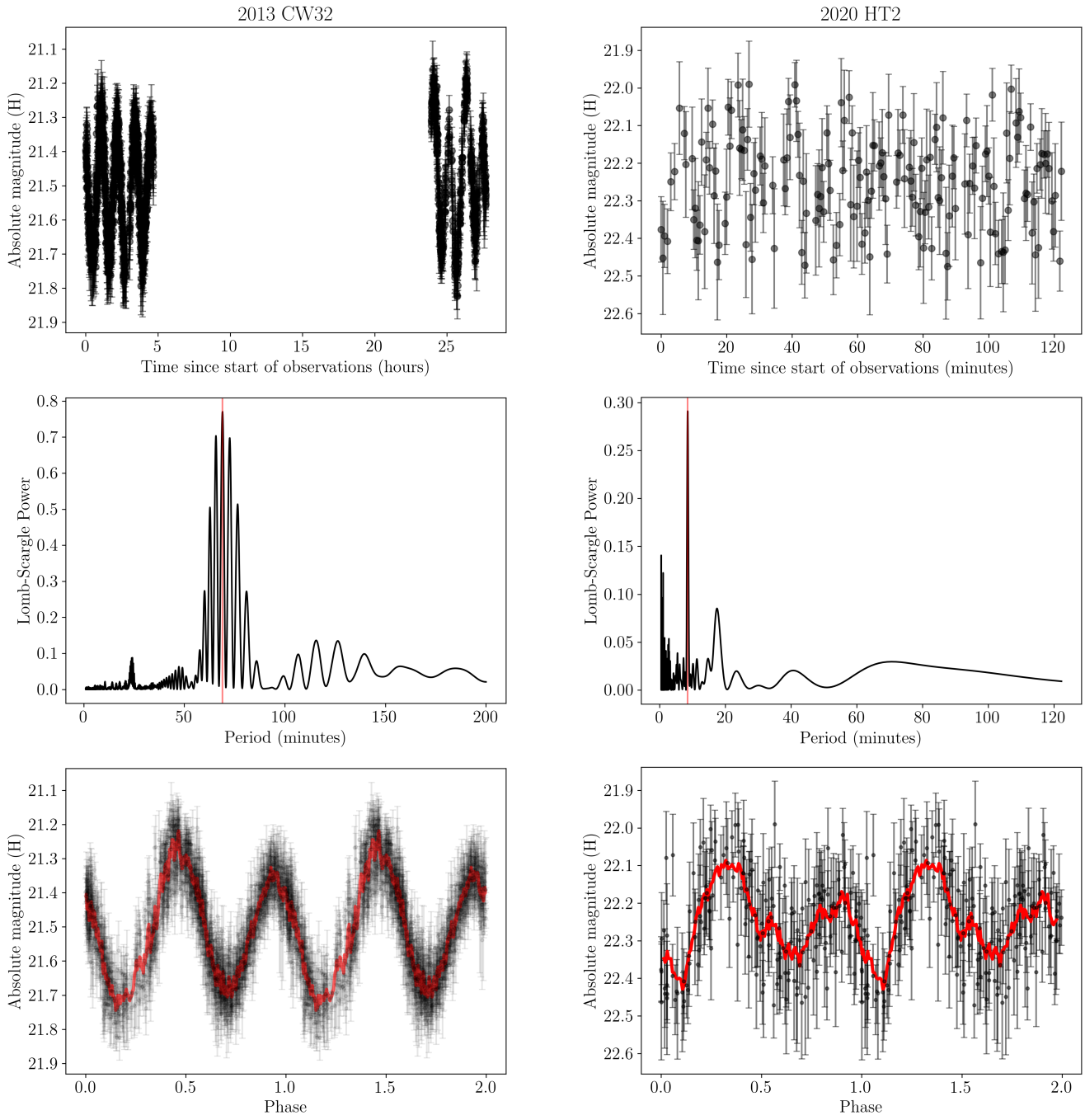

(a) 2013 CW32 (b) 2020 HT2

Figure 3.6: Three plots are shown for two targets: (a) 2013 CW32 and (b) 2020 HT2. Top: The light curve of the target, with the absolute magnitudes in the three filters (H_g, H_r and H_i) as a function of time. H_g and H_i were normalised to H_r by shifting them with the g′−r′ and r′−i′ colours, respectively, to form one densely-sampled light curve. Middle: The Lomb-Scargle periodogram of the light curve, with the highest peak indicated with a red line. Bottom: The phase folded light curve (magnitude as a function of the rotation phase), where the data were folded at the median rotation period given in Table 3.3. The red line is a running average with window of 10 data points to guide the eye and which was also used to calculate the amplitude. The same plots are given in Figure C.1 of Appendix C for the remaining seven targets that had a resolvable light curve period.

2010 AE30 and 2013 DU also have amplitudes close to 1 magnitude (within 2σ and 1σ, respectively). From equation 1.2, shown in Chapter 1, an amplitude of 1 suggests an axial ratio of about 2.5. This means that these two small NEAs potentially have an elongated shape.

Out of these eight small NEAs, only 2013 CW32 has a previously reported rotation period. In the light curve of 2013 CW32, the rotation can clearly be seen (see Figure B.1h and 3.6a). A distinct peak in the periodogram is also visible at about 70 minutes. The high cadence data and two-day observations resulted in the FAP being extremely small, as seen in Table 3.3. The rotation period obtained in this thesis is consistent with the period extracted by Hora et al. (2018) who only observed the target for 42.6 minutes and therefore only extracted a lower limit to the rotation period. They obtained a lower limit of 79.2 ± 2.6 minutes and also calculated an amplitude of 0.224 ± 0.030 magnitudes. This amplitude is about half the amplitude measured in this study.

When the absolute magnitudes were calculated, the default value for the slope parameter was used in equation 2.9 (G = 0.15). By converting to absolute magnitudes, the brightening or dimming of the targets observed on two consecutive nights and therefore at different phase angles were removed. The result was that the observations over the two nights were "normalised" to the same absolute magnitude. However, for 2013 CW32, there were still a decrease in brightness from the first to the second night, possibly indicating that the slope parameter for this target is different from the default value. This NEA was observed at a phase angle of around 51° on the first night and 36° on the second night. To account for the slight decrease in brightness, equation 2.9 was fitted to the r′ reduced magnitudes as a function of phase angle to determine the slope parameter. The slope parameter from the fit was calculated as -0.008. Even though this value is not unusual, it is not expected for an S-type asteroid (Vereš et al., 2015). As discussed in Section 3.2 and shown in Table 3.1, 2013 CW32 is classified as an S-complex asteroid (with a probability of almost 100%). It should be noted that equation 2.9 was only fitted for a limited range of phase angles ($36° < \alpha < 51°$) and therefore the slope parameter could be incorrect. The extracted slope parameter was sufficient to normalise the data on the two nights, which allowed the data to fold on top of each other in the phase folded light curve, but it is not used in any of the further analysis. If this unusually low slope parameter for this S-type asteroid is real, it is worth further investigation.

In addition to the nine NEAs that had period-resolved light curves, lower limits to the rotation period of three additional NEAs are also reported in Table 3.3. These NEAs are 1620 Geographos (1951 RA), 86667 (2000 FO10) and 2019 EN and their light curves are shown in Figure B.1a, B.1b and B.1k of Appendix B, respectively. There are clearly some increase/decrease in brightness indicative of rotation, but the targets were not observed for long enough to resolve the light curve period. The lower limit to the rotation period is just twice the observation period. 1620 Geographos has a reported rotation period of 5.2201 ± 0.0002 hours (Warner and Stephens, 2019a, 2020a) and 2019 EN has a reported rotation period of 14.33 hours (Pál et al., 2020). The period of 2000 FO10 was calculated to be between 25.6 and 26.4 hours by Polishook and Brosch (2008), but the authors noted that the data were poorly sampled. Warner and Stephens (2020b) extracted a period of 53.77 ± 0.01 hours. The results of this study agree with these reported periods since the lower limits are all below the reported periods.

The light curves of 481394 (2006 SF6) (Figure B.1c), 2007 YU56 (Figure B.1d), 358744 (2008 CR118) (Figure B.1e), 528159 (2008 HS3) (Figure 3.2a), 515767 (2015 JA2) (Figure B.1i), 2019 AG7 (Figure B.1j), 2019 OM (Figure B.1m) and 2019 PZ2 (Figure B.1n) show no clear periodicity and no period was

detected in the periodogram. These targets are *not* reported in Table 3.3. As discussed by Thirouin et al. (2018), possible explanations for a flat rotation curve could be when the target:

- Is a slow rotator and has a light curve period longer than the observation period.
- Is observed with a pole-on orientation.
- Has a spherical shape.
- Is a fast to ultra-rapid rotator with a light curve amplitude below the noise of the observation.

The light curve of 2008 HS3 show some small variations, but is still relatively flat. Warner and Stephens (2019b) reported a rotation period of 10.67 ± 0.01 hours for this NEA (much longer than the observation period in this project), but the rotation period varied around 10 hours depending on different subsets of data obtained when the target was at different phase angles. Pál et al. (2020) reported an even longer rotation period of 21.71 hours with data from the Transiting Exoplanet Survey Satellite (TESS; Ricker et al., 2014). For 2019 OM, Warner and Stephens (2020a) calculated a rotation period of 15.83 ± 0.07 hours and an amplitude of 0.39 magnitudes. Even though in this project 2019 OM was observed over two consecutive nights and therefore a period should have been resolved, no period was detected in the periodogram. This could be because the data was sparse and within the uncertainties, the light curve appears flat. The uncertainties were between approximately 0.1 and 0.2 magnitudes, which means an amplitude of about 0.4 would not be resolved. 2006 SF6, 2015 JA2 and 2019 PZ2 were only observed for a short amount of time and the data were too sparse to resolve any periodicity.

2007 YU56, 2008 CR118 and 2019 AG7 does not have a period reported in the Asteroid Photometry Lightcurve Database[43] (Warner et al., 2009). Most slow rotators have an absolute magnitude smaller than 22.4 (Thirouin et al., 2018). 2007 YU56 has an absolute magnitude of 22.1 and 2008 CR118 has an absolute magnitude of 18.9 (see Table 2.1), therefore both of them could possibly be slow rotators.

2019 AG7 was observed on two consecutive nights over an observing period of about 25 hours. It has an absolute magnitude of 25.5, which corresponds to a diameter of about 24 m with an assumed geometric albedo of 0.2. Asteroids of this size are not known to be slow rotators, as shown in Figure 1.2 of Chapter 1, because of an observation bias. These small NEAs are difficult to observe for a long period of time because they are only bright enough to be observed with ground-based telescopes for a short amount of time. Therefore, this target possibly has a rotation period >25 hours. It was most probably not observed pole-on. In Thirouin et al. (2018), it was determined that the probability of observing a small NEA (< 100 m in diameter) pole-on, is less than 1%. 2019 AG7 could also have a spherical shape. Benner et al. (2015) showed from radar observations that many NEAs with diameters > 200 m have an irregular shape and some are more oblate with a ridge at the center (a diamond-like shape, similar to the shape of asteroid Bennu). As explained by Thirouin et al. (2018), if smaller NEAs follow the same trend, 2019 AG7 could be spherical. Another possibility could be that if too long exposure times are used, short periods of a few seconds could be missed. The detectable rotation periodicity (P) can be calculated through equation 3.1, where T_{exp} is the optimal exposure time (Pravec et al., 2000; Thirouin et al., 2018).

[43] http://alcdef.org/

$$T_{exp} = 0.185 \times P \tag{3.1}$$

2019 AG7 was observed with an exposure time of 5 seconds (see Table 2.1), which means any period larger than 27 seconds would be detected. If this target has a rotation period <27 seconds, this would not be detected in the periodogram. This extremely short rotation period is not impossible since Thirouin et al. (2018) reported two targets with rotation periods smaller than 20 seconds. Both of these targets have a diameters of about 10 meters as discussed in Chapter 1.

4 | Conclusion

Studying properties such as the taxonomic class and rotation period of NEAs can give an indication of the most likely properties of potential future impactors. The physical properties are also vital to the success of space missions and it can assist in the understanding of the formation and evolution of the Solar System, including the role the early NEAs had in the delivery of life-starting ingredients to the Earth. Because small NEAs are generally only observable near or at their close approach to the Earth, their discovery and characterisation lag behind.

This MSc project started as a pilot study to determine if the combination of the SAAO 40-inch telescope and SHOC is suitable to observe and characterise small, close-approaching NEAs. The pilot study was expanded to this project after its success. In this project, 20 NEAs were successfully observed and characterised, of which 14 had diameters < 300 m. Additionally, seven large MBAs, with recorded properties from the literature, were observed to verify the methodology and validate the results. Characterisation involved assigning taxonomic probabilities to the targets based on spectra from the Bus-DeMeo classification scheme and extracting the rotation period from multi-band photometry.

The taxonomic probabilities were reported for all of the targets by means of a ML approach. The taxonomic classes considered were the S-, C- and X-complexes, and D-, Q- and V-types. Fifteen targets had a taxonomic probability >50% in one class and a discrete classification was assigned. New taxonomic classes were reported for 11 targets, nine of which had diameters < 300 m. A notable result of this study is that because the Q class was included in the classification and the ML algorithm was able to distinguish between the C-complex and Q-type asteroids, the combined fraction of S-complex *and* Q-type NEAs agreed with the fraction of meteorite falls due to ordinary chondrites (∼80%). S-complex and Q-type asteroids are composed of the same material as ordinary chondrites, but the S-complex asteroids are just weathered. This result is contrary to other studies that did not include the Q class in their classification. The result is based on a small number of NEAs, but it does agree with previously reported predictions.

A rotation period was extracted for 9 out of the 20 NEAs. Only these targets were observed for long enough to resolve a light curve period. A lower limit to the rotation period was reported for three NEAs. The remaining targets did not show any periodicity in the light curves and a period was not detectable or resolvable in the periodogram. The extracted rotation periods were all consistent with previous studies. Three small NEAs (2010 AE30, 2019 SP3 and 2020 HT2), all with $H > 22$, has rotation periods faster than the 2.2 hour spin barrier, suggesting they are rigid rocks and not rubble piles.

In the future, many of the targets reported in this project could be observed again at their next close approach to the Earth to obtain additional data covering a couple of days - especially the targets that had flat or partial light curves or those without a constrained periodogram peak. The problem,

however, is that many of these targets will not make a close approach and be observable with a 1-m class telescope in at least the next 5 years. For example, two of the smallest NEAs in this project was 2019 AG7 and 2019 SP3. The first target will make its next close approach in 2028 and will be observable with a 1-m class telescope, but the second target will only make a close approach in 2046 and it will not be observable with a 1-m telescope.

As an alternative, data in this project could be combined with data of the same targets from other all-sky surveys that likely also observed these objects during their close approach (e.g., ATLAS, Pan-STARRS or the Zwicky Transient Facility[44] (ZTF; Masci et al., 2018)). Additional data over a longer observation period will be able to help constrain the rotation periods of some of the targets. Another parameter in the ML algorithm, like the slope parameter (G), might also be useful to definitively classify the targets on the boundaries between multiple taxonomic classes.

Another possibility is that the observations of small NEAs could be continued at the SAAO with all the available 1-m class telescopes. Even though the same targets will not be observed, the sample size of this project could be increased and the results of this study could be confirmed, especially the combined fraction of S-complex and Q-type asteroids.

[44] https://www.ztf.caltech.edu/

Bibliography

C. P. Ahn, R. Alexandroff, C. A. Prieto, S. F. Anderson, T. Anderton, B. H. Andrews, É. Aubourg, S. Bailey, E. Balbinot, et al. The Ninth Data Release of the Sloan Digital Sky Survey: First Spectroscopic Data From the SDSS-III Baryon Oscillation Spectroscopic Survey. *The Astrophysical Journal Supplement Series*, 203 (2):21, 2012.

L. W. Alvarez, W. Alvarez, F. Asaro, and H. V. Michel. Extraterrestrial Cause for the Cretaceous-Tertiary Extinction. *Science*, 208(4448):1095–1108, 1980.

D. Bancelin, E. Pilat-Lohinger, T. I. Maindl, F. Ragossnig, and C. Schäfer. The Influence of Orbital Resonances on the Water Transport to Objects in the Circumprimary Habitable Zone of Binary Star Systems. *The Astronomical Journal*, 153(6):269, 2017.

I. N. Belskaya, S. Fornasier, G. P. Tozzi, R. Gil-Hutton, A. Cellino, K. Antonyuk, Y. N. Krugly, A. N. Dovgopol, and S. Faggi. Refining the asteroid taxonomy by polarimetric observations. *Icarus*, 284:30–42, 2017.

L. A. M. Benner, M. W. Busch, J. D. Giorgini, P. A. Taylor, and J. L. Margot. Radar Observations of Near-Earth and Main-Belt Asteroids. *Asteroids IV*, pages 165–182, 2015.

D. Bérard, B. Sicardy, J. I. B. Camargo, J. Desmars, F. Braga-Ribas, J.-L. Ortiz, R. Duffard, N. Morales, E. Meza, et al. The Structure of Chariklo's Rings from Stellar Occultations. *The Astronomical Journal*, 154 (4):144, 2017.

E. Bertin. Automatic Astrometric and Photometric Calibration with SCAMP. In C. Gabriel, C. Arviset, D. Ponz, and S. Enrique, editors, *Astronomical Data Analysis Software and Systems XV*, volume 351 of *Astronomical Society of the Pacific Conference Series*, page 112, 2006.

E. Bertin and S. Arnouts. SExtractor: Software for source extraction. *Astronomy and Astrophysics Supplement*, 117:393–404, 1996.

M. Bessell, G. Bloxham, B. Schmidt, S. Keller, P. Tisserand, and P. Francis. SkyMapper Filter Set: Design and Fabrication of Large-Scale Optical Filters. *Publications of the Astronomical Society of the Pacific*, 123 (905):789–798, 2011.

R. P. Binzel, V. Reddy, and T. L. Dunn. The Near-Earth Object Population: Connections to Comets, Main-Belt Asteroids, and Meteorites. *Asteroids IV*, pages 243–256, 2015.

R. P. Binzel, F. E. DeMeo, E. V. Turtelboom, S. J. Bus, A. Tokunaga, T. H. Burbine, C. Lantz, D. Polishook, B. Carry, et al. Compositional distributions and evolutionary processes for the near-Earth object population: Results from the MIT-Hawaii Near-Earth Object Spectroscopic Survey (MITHNEOS). *Icarus*, 324:41–76, 2019.

C. Blanco, M. Di Martino, and D. Riccioli. New rotational periods of 18 asteroids. *Planetary and Space Science*, 48(4):271–284, 2000.

W. F. Bottke, A. Morbidelli, R. Jedicke, J.-M. Petit, H. F. Levison, P. Michel, and T. S. Metcalfe. Debiased Orbital and Absolute Magnitude Distribution of the Near-Earth Objects. *Icarus*, 156(2):399–433, 2002.

A. Bouvier and M. Wadhwa. The age of the Solar System redefined by the oldest Pb-Pb age of a meteoritic inclusion. *Nature Geoscience*, 3(9):637–641, 2010.

E. Bowell, B. Hapke, D. Domingue, K. Lumme, J. Peltoniemi, and A. W. Harris. Application of photometric models to asteroids. In R. P. Binzel, T. Gehrels, and M. S. Matthews, editors, *Asteroids II*, pages 524–556, 1989.

P. G. Brown, J. D. Assink, L. Astiz, R. Blaauw, M. B. Boslough, J. Borovička, N. Brachet, D. Brown, M. Campbell-Brown, et al. A 500-kiloton airburst over Chelyabinsk and an enhanced hazard from small impactors. *Nature*, 503(7475):238–241, 2013.

T. H. Burbine. *Asteroids: Astronomical and Geological Bodies*. Cambridge Planetary Science. Cambridge University Press, 2017.

S. J. Bus and R. P. Binzel. Phase II of the Small Main-Belt Asteroid Spectroscopic Survey: A Feature-Based Taxonomy. *Icarus*, 158(1):146–177, 2002.

B. Carry, E. Solano, S. Eggl, and F. E. DeMeo. Spectral properties of near-Earth and Mars-crossing asteroids using Sloan photometry. *Icarus*, 268:340–354, 2016.

J. M. Carvano, P. H. Hasselmann, D. Lazzaro, and T. Mothé-Diniz. SDSS-based taxonomic classification and orbital distribution of main belt asteroids. *Astronomy & Astrophysics*, 510:A43, 2010.

M. Clark. Lightcurve results for 383 Janina, 899 Jokaste, 1825 Klare, 2525 O'Steen 5064 Tanchozuru, and (17939) 1999 HH8. *Minor Planet Bulletin*, 33(3):53–56, 2006.

R. Coppejans, A. A. S. Gulbis, M. M. Kotze, D. L. Coppejans, H. L. Worters, P. A. Woudt, H. Whittal, J. Cloete, and P. Fourie. Characterizing and Commissioning the Sutherland High-Speed Optical Cameras (SHOC). *Publications of the Astronomical Society of the Pacific*, 125(930):976–988, 2013.

C. L. Dandy, A. Fitzsimmons, and S. J. Collander-Brown. Optical colors of 56 near-Earth objects: trends with size and orbit. *Icarus*, 163(2):363–373, 2003.

M. Delbo', K. Walsh, B. Bolin, C. Avdellidou, and A. Morbidelli. Identification of a primordial asteroid family constrains the original planetesimal population. *Science*, 357(6355):1026–1029, 2017.

F. E. Demeo and B. Carry. The taxonomic distribution of asteroids from multi-filter all-sky photometric surveys. *Icarus*, 226(1):723–741, 2013.

F. E. Demeo and B. Carry. Solar System evolution from compositional mapping of the asteroid belt. *Nature*, 505(7485):629–634, 2014.

F. E. DeMeo, R. P. Binzel, S. M. Slivan, and S. J. Bus. An extension of the Bus asteroid taxonomy into the near-infrared. *Icarus*, 202(1):160–180, 2009.

J. Durech, J. Hanuš, D. Oszkiewicz, and R. Vančo. Asteroid models from the Lowell photometric database. *Astronomy & Astrophysics*, 587:A48, 2016.

R. Dymock. The H and G magnitude system for asteroids. *Journal of the British Astronomical Association*, 117:342–343, 2007.

M. Elvis. Let's mine asteroids - For science and profit. *Nature*, 485(7400):549, 2012.

J. P. Emery and R. H. Brown. The surface composition of Trojan asteroids: constraints set by scattering theory. *Icarus*, 170(1):131–152, 2004.

N. Erasmus, M. Mommert, D. E. Trilling, A. A. Sickafoose, C. van Gend, and J. L. Hora. Characterization of Near-Earth Asteroids Using KMTNET-SAAO. *The Astronomical Journal*, 154(4):162, 2017.

N. Erasmus, A. McNeill, M. Mommert, D. E. Trilling, A. A. Sickafoose, and C. van Gend. Taxonomy and Light-curve Data of 1000 Serendipitously Observed Main-belt Asteroids. *The Astrophysical Journal Supplement Series*, 237(1):19, 2018.

N. Erasmus, A. McNeill, M. Mommert, D. E. Trilling, A. A. Sickafoose, and K. Paterson. A Taxonomic Study of Asteroid Families from KMTNET-SAAO Multiband Photometry. *The Astrophysical Journal Supplement Series*, 242(2):15, 2019.

N. Erasmus, S. Navarro-Meza, A. McNeill, D. E. Trilling, A. A. Sickafoose, L. Denneau, H. Flewelling, A. Heinze, and J. L. Tonry. Investigating Taxonomic Diversity within Asteroid Families through ATLAS Dual-band Photometry. *The Astrophysical Journal Supplement Series*, 247(1):13, 2020.

H. A. Flewelling, E. A. Magnier, K. C. Chambers, J. N. Heasley, C. Holmberg, M. E. Huber, W. Sweeney, C. Z. Waters, A. Calamida, et al. The Pan-STARRS1 Database and Data Products. *The Astrophysical Journal Supplement Series*, 251(1):7, 2020.

Gaia Collaboration, T. Prusti, J. H. J. De Bruijne, A. G. A. Brown, A. Vallenari, C. Babusiaux, C. A. L. Bailer-Jones, U. Bastian, M. Biermann, et al. The Gaia mission. *Astronomy & Astrophysics*, 595, 2016.

A. Ginsburg, B. M. Sipőcz, C. E. Brasseur, P. S. Cowperthwaite, M. W. Craig, C. Deil, J. Guillochon, G. Guzman, S. Liedtke, et al. astroquery: An Astronomical Web-querying Package in Python. *The Astronomical Journal*, 157(3):98, 2019.

J. Gradie and E. Tedesco. Compositional Structure of the Asteroid Belt. *Science*, 216(4553):1405–1407, 1982.

J. Gradie and J. Veverka. The composition of the Trojan asteroids. *Nature*, 283(5750):840–842, 1980.

M. Granvik, A. Morbidelli, D. Vokrouhlický, W. F. Bottke, D. Nesvorný, and R. Jedicke. Escape of asteroids from the main belt. *Astronomy & Astrophysics*, 598:A52, 2017.

A. W. Harris and A. W. Harris. On the Revision of Radiometric Albedos and Diameters of Asteroids. *Icarus*, 126(2):450–454, 1997.

Alan W. Harris. Tumbling asteroids. *Icarus*, 107(1):209–211, 1994.

S. Hasegawa, D. Kuroda, K. Kitazato, T. Kasuga, T. Sekiguchi, N. Takato, K. Aoki, A. Arai, Y. J. Choi, et al. Physical properties of near-Earth asteroids with a low delta-v: Survey of target candidates for the Hayabusa2 mission. *Publications of the Astronomical Society of Japan*, 70(6), 2018.

P. Hatch and P. A. Wiegert. On the rotation rates and axis ratios of the smallest known near-Earth asteroids—The archetypes of the Asteroid Redirect Mission targets. *Planetary and Space Science*, 111:100–104, 2015.

A. A. Henden, M. Templeton, D. Terrell, T. C. Smith, S. Levine, and D. Welch. VizieR Online Data Catalog: AAVSO Photometric All Sky Survey (APASS) DR9 (Henden+, 2016). *VizieR Online Data Catalog*, page II/336, 2016.

D. L. Holdsworth, H. Saio, and D. W. Kurtz. HD 42659: the only known roAp star in a spectroscopic binary observed with B photometry, TESS, and SALT. *Monthly Notices of the Royal Astronomical Society*, 489(3): 4063–4071, 2019.

J. L. Hora, A. Siraj, M. Mommert, A. McNeill, D. E. Trilling, A. Gustafsson, H. A. Smith, G. G. Fazio, S. Chesley, et al. Infrared Light Curves of Near-Earth Objects. *The Astrophysical Journal Supplement Series*, 238(2):22, 2018.

J. D. Hunter. Matplotlib: A 2D graphics environment. *Computing in Science & Engineering*, 9(3):90–95, 2007.

S. Ieva, E. Dotto, E. Mazzotta Epifani, D. Perna, A. Rossi, M. A. Barucci, A. Di Paola, R. Speziali, M. Micheli, et al. Photometric survey of 67 near-Earth objects. *Astronomy & Astrophysics*, 615:A127, 2018.

Ž. Ivezić, S. Tabachnik, R. Rafikov, R. H. Lupton, T. Quinn, M. Hammergren, L. Eyer, J. Chu, J. C. Armstrong, et al. Solar System Objects Observed in the Sloan Digital Sky Survey Commissioning Data. *The Astronomical Journal*, 122(5):2749–2784, 2001.

R. A. Koff. Lightcurves of asteroids 141 Lumen, 259 Alatheia, 363 Padua, 455 Bruchsalia 514 Armida, 524 Fidelio, and 1139 Atami. *Minor Planet Bulletin*, 33(2):31–33, 2006.

D. S. Lauretta, S. S. Balram-Knutson, E. Beshore, W. V. Boynton, C. Drouet d'Aubigny, D. N. DellaGiustina, H. L. Enos, D. R. Golish, C. W. Hergenrother, et al. OSIRIS-REx: Sample Return from Asteroid (101955) Bennu. *Springer*, 212(1-2):925–984, 2017.

D. S. Lauretta, D. N. DellaGiustina, C. A. Bennett, D. R. Golish, K. J. Becker, S. S. Balram-Knutson, O. S. Barnouin, T. L. Becker, W. F. Bottke, et al. The unexpected surface of asteroid (101955) Bennu. *Nature*, 568(7750):55–60, 2019.

D. Lazzaro, C. A. Angeli, J. M. Carvano, T. Mothé-Diniz, R. Duffard, and M. Florczak. S3OS2: the visible spectroscopic survey of 820 asteroids. *Icarus*, 172(1):179–220, 2004. Special Issue: Cassini-Huygens at Jupiter.

N. R. Lomb. Least-squares frequency analysis of unequally spaced data. *Astrophysics and Space Science*, 39 (2):447–462, 1976.

A. Marciniak, F. Pilcher, D. Oszkiewicz, T. Santana-Ros, S. Urakawa, S. Fauvaud, P. Kankiewicz, Ł. Tychoniec, M. Fauvaud, et al. Against the biases in spins and shapes of asteroids. *Planetary and Space Science*, 118: 256–266, 2015. SI:ACM Interrelated.

A. Marciniak, P. Bartczak, T. Müller, J. J. Sanabria, V. Alí-Lagoa, P. Antonini, R. Behrend, L. Bernasconi, M. Bronikowska, et al. Photometric survey, modelling, and scaling of long-period and low-amplitude asteroids. *Astronomy & Astrophysics*, 610:A7, 2018.

F. J. Masci, R. R. Laher, B. Rusholme, D. L. Shupe, S. Groom, J. Surace, E. Jackson, S. Monkewitz, R. Beck, et al. The Zwicky Transient Facility: Data Processing, Products, and Archive. *Publications of the Astronomical Society of the Pacific*, 131(995):018003, 2018.

D. L. Mathias, L. F. Wheeler, and J. L. Dotson. A probabilistic asteroid impact risk model: assessment of sub-300m impacts. *Icarus*, 289:106–119, 2017.

M. Mommert. PHOTOMETRYPIPELINE: An automated pipeline for calibrated photometry. *Astronomy and Computing*, 18:47–53, 2017.

M. Mommert, D. E. Trilling, D. Borth, R. Jedicke, N. Butler, M. Reyes-Ruiz, B. Pichardo, E. Petersen, T. Axelrod, and N. Moskovitz. First Results From The Rapid-Response Spectrophotometric Characterization Of Near-Earth Objects Using UKIRT. *The Astronomical Journal*, 151(4):98, 2016.

M. Mommert, D. E. Trilling, J. L. Hora, C. Lejoly, A. Gustafsson, M. Knight, N. Moskovitz, and H. A. Smith. Systematic Characterization of and Search for Activity in Potentially Active Asteroids. *The Planetary Science Journal*, 1(1):10, 2020.

D. Morate, J. de León, M. De Prá, J. Licandro, N. Pinilla-Alonso, H. Campins, A. Arredondo, J. M. Carvano, D. Lazzaro, and A. Cabrera-Lavers. The last pieces of the primitive inner belt puzzle: Klio, Chaldaea, Chimaera, and Svea. *Astronomy & Astrophysics*, 630:A141, 2019.

A. Morbidelli and D. Vokrouhlický. The Yarkovsky-driven origin of near-Earth asteroids. *Icarus*, 163(1): 120–134, 2003.

A. Morbidelli, J. Chambers, J. I. Lunine, J. M. Petit, F. Robert, G. B. Valsecchi, and K. E. Cyr. Source regions and time scales for the delivery of water to Earth. *Meteoritics and Planetary Science*, 35(6):1309–1320, 2000.

A. Morbidelli, H. F. Levison, K. Tsiganis, and R. Gomes. Chaotic capture of Jupiter's Trojan asteroids in the early Solar System. *Nature*, 435(7041):462–465, 2005.

A. Morbidelli, K. Tsiganis, A. Crida, H. F. Levison, and R. Gomes. Dynamics of the Giant Planets of the Solar System in the Gaseous Protoplanetary Disk and Their Relationship to the Current Orbital Architecture. *The Astronomical Journal*, 134(5):1790–1798, 2007.

S. Navarro-Meza, M. Mommert, D. E. Trilling, N. Butler, M. Reyes-Ruiz, B. Pichardo, T. Axelrod, R. Jedicke, and N. Moskovitz. First Results from the Rapid-response Spectrophotometric Characterization of Near-Earth Objects Using RATIR. *The Astronomical Journal*, 157(5):190, 2019.

A. Pál, R. Szakáts, C. Kiss, A. Bódi, Z. Bognár, C. Kalup, L. L. Kiss, G. Marton, L. Molnár, et al. Solar System Objects Observed with TESS—First Data Release: Bright Main-belt and Trojan Asteroids from the Southern Survey. *The Astrophysical Journal Supplement Series*, 247(1):26, 2020.

K. Paterson, P. A. Woudt, B. Warner, H. Breytenbach, C. K. Gilligan, M. Motsoaledi, J. R. Thorstensen, and H. L. Worters. High-speed photometry of faint cataclysmic variables – IX. Targets from multiple transient surveys. *Monthly Notices of the Royal Astronomical Society*, 486(2):2422–2434, 2019.

F. Pedregosa, G. Varoquaux, A. Gramfort, V. Michel, B. Thirion, O. Grisel, M. Blondel, P. Prettenhofer, R. Weiss, et al. Scikit-learn: Machine Learning in Python. *Journal of Machine Learning Research*, 12: 2825–2830, 2011.

D. Perna, M. A. Barucci, L. Drube, A. Falke, M. Fulchignoni, A. W. Harris, A. W. Harris, and Z. Kanuchova. A global response roadmap to the asteroid impact threat: The NEOShield perspective. *Planetary and Space Science*, 118:311–317, 2015. SI:ACM Interrelated.

D. Perna, M. A. Barucci, M. Fulchignoni, M. Popescu, I. Belskaya, S. Fornasier, A. Doressoundiram, C. Lantz, and F. Merlin. A spectroscopic survey of the small near-Earth asteroid population: Peculiar taxonomic distribution and phase reddening. *Planetary and Space Science*, 157:82–95, 2018.

D. Polishook and N. Brosch. Photometry of Aten asteroids—More than a handful of binaries. *Icarus*, 194(1): 111–124, 2008.

P. Pravec and A. W. Harris. Fast and slow rotation of asteroids. *Icarus*, 148(1):12–20, 2000.

P. Pravec, C. Hergenrother, R. Whiteley, L. Šarounovâ, P. Kušnirák, and M. Wolf. Fast Rotating Asteroids 1999 TY2, 1999 SF10, and 1998 WB2. *Icarus*, 147(2):477–486, 2000.

P. Pravec, A.W. Harris, P. Scheirich, P. Kušnirák, L. Šarounová, C.W. Hergenrother, S. Mottola, M.D. Hicks, G. Masi, et al. Tumbling asteroids. *Icarus*, 173(1):108–131, 2005.

A. M. Price-Whelan, B. M. Sipőcz, H. M. Günther, P. L. Lim, S. M. Crawford, S. Conseil, D. L. Shupe, M. W. Craig, N. Dencheva, et al. The Astropy Project: Building an Open-science Project and Status of the v2.0 Core Package. *The Astronomical Journal*, 156(3):123, 2018.

J. T. Rayner, D. W. Toomey, P. M. Onaka, A. J. Denault, W. E. Stahlberger, W. D. Vacca, M. C. Cushing, and S. Wang. SpeX: A Medium-Resolution 0.8–5.5 Micron Spectrograph and Imager for the NASA Infrared Telescope Facility. *Publications of the Astronomical Society of the Pacific*, 115(805):362–382, 2003.

V. Reddy, M. S. Kelley, D. Farnocchia, W. H. Ryan, C. A. Thomas, L. A. M. Benner, J. Dotson, M. Micheli, M. J. Brucker, et al. Near-Earth asteroid 2012 TC4 observing campaign: Results from a global planetary defense exercise. *Icarus*, 326:133–150, 2019.

G. R. Ricker, J. N. Winn, R. Vanderspek, D. W. Latham, G. Á. Bakos, J. L. Bean, Z. K. Berta-Thompson, T. M. Brown, L. Buchhave, et al. Transiting Exoplanet Survey Satellite. *Journal of Astronomical Telescopes, Instruments, and Systems*, 1(1):1–10, 2014.

A. Rohatgi. Webplotdigitizer: Version 4.3, 2020.

J. D. Scargle. Studies in astronomical time series analysis. II - Statistical aspects of spectral analysis of unevenly spaced data. *The Astrophysical Journal*, 263:835–853, 1982.

E. M. Shoemaker, J. G. Williams, E. F. Helin, and R. F. Wolfe. Earth crossing asteroids: orbital classes, collision rates with earth, and origin. In T. Gehrels and M. S. Matthews, editors, *Asteroids*, pages 253–282, 1979.

G. H. Stokes, B. W. Barbee, W. F. Bottke Jr., M. W. Buie, S. R. Chesley, P. W. Chodas, J. B. Evans, and R. E. Gold. Update to Determine the Feasibility of Enhancing the Search and Characterization of NEOs. Technical report, Report prepared at the request of the National Aeronautics and Space Administration, 2017.

Gy. M. Szabó, Ž. Ivezić, M. Jurić, R. Lupton, and L. L. Kiss. Colour variability of asteroids in the Sloan Digital Sky Survey Moving Object Catalog. *Monthly Notices of the Royal Astronomical Society*, 348(3): 987–998, 2004.

The Astropy Collaboration, T. P. Robitaille, E. J. Tollerud, P. Greenfield, M. Droettboom, E. Bray, T. Aldcroft, M. Davis, A. Ginsburg, et al. Astropy: A community Python package for astronomy. *Astronomy & Astrophysics*, 558:A33, 2013.

A. Thirouin, N. A. Moskovitz, R. P. Binzel, E. J. Christensen, F. E. DeMeo, M. J. Person, D. Polishook, C. A. Thomas, D. Trilling, et al. The Mission Accessible Near-Earth Objects Survey: Four Years of Photometry. *The Astrophysical Journal Supplement Series*, 239(1):4, 2018.

D. J. Tholen. *Asteroid Taxonomy from Cluster Analysis of Photometry.* PhD thesis, University of Arizona, Tucson, 1984.

D. J. Tholen. Asteroid taxonomic classifications. In R. P. Binzel, T. Gehrels, and M. S. Matthews, editors, *Asteroids II*, pages 1139–1150, 1989.

C. A. Thomas, D. E. Trilling, J. P. Emery, M. Mueller, J. L. Hora, L. A. M. Benner, B. Bhattacharya, W. F. Bottke, S. Chesley, et al. ExploreNEOs. v. Average Albedo by Taxonomic Complex in the Near-Earth Asteroid Population. *The Astronomical Journal*, 142(3):85, 2011.

D. Tody. The Iraf Data Reduction And Analysis System. In David L. Crawford, editor, *Instrumentation in Astronomy VI*, volume 0627, pages 733–748. International Society for Optics and Photonics, SPIE, 1986.

D. Tody. IRAF in the Nineties. In R. J. Hanisch, R. J. V. Brissenden, and J. Barnes, editors, *Astronomical Data Analysis Software and Systems II*, volume 52 of *Astronomical Society of the Pacific Conference Series*, page 173, 1993.

J. L. Tonry, C. W. Stubbs, K. R. Lykke, P. Doherty, I. S. Shivvers, W. S. Burgett, K. C. Chambers, K. W. Hodapp, N. Kaiser, et al. The Pan-STARRS1 Photometric System. *The Astrophysical Journal*, 750(2):99, 2012.

J. L. Tonry, L. Denneau, A. N. Heinze, B. Stalder, K. W. Smith, S. J. Smartt, C. W. Stubbs, H. J. Weiland, and A. Rest. ATLAS: A High-cadence All-sky Survey System. *Publications of the Astronomical Society of the Pacific*, 130(988):064505, 2018.

S. van der Walt, J. L. Schönberger, J. Nunez-Iglesias, F. Boulogne, J. D. Warner, N. Yager, E. Gouillart, T. Yu, and the scikit-image contributors. scikit-image: image processing in Python. *PeerJ*, 2:e453, 2014.

J. T. VanderPlas. Understanding the Lomb–Scargle Periodogram. *The Astrophysical Journal Supplement Series*, 236(1):16, 2018.

A. Vazan and R. Sari. On the aspect ratio of 'Oumuamua: less elongated shape for irregular surface properties. *Monthly Notices of the Royal Astronomical Society*, 493(2):1546–1552, 2020.

P. Vereš, R. Jedicke, A. Fitzsimmons, L. Denneau, M. Granvik, B. Bolin, S. Chastel, R. J. Wainscoat, W. S. Burgett, et al. Absolute magnitudes and slope parameters for 250,000 asteroids observed by Pan-STARRS PS1 – Preliminary results. *Icarus*, 261:34–47, 2015.

D. Vokrouhlický, W. F. Bottke, S. R. Chesley, D. J. Scheeres, and T. S. Statler. The Yarkovsky and YORP Effects. *Asteroids IV*, pages 509–531, 2015.

K. J. Walsh, A. Morbidelli, S. N. Raymond, D. P. O'Brien, and A. M. Mandell. A low mass for Mars from Jupiter's early gas-driven migration. *Nature*, 475(7355):206–209, 2011.

B. D. Warner and R. D. Stephens. Near-Earth Asteroid Lightcurve Analysis at the Center for Solar System Studies: 2019 January-April. *Minor Planet Bulletin*, 46(3):304–314, 2019a.

B. D. Warner and R. D. Stephens. Near-Earth Asteroid Lightcurve Analysis at the Center for Solar System Studies. *Minor Planet Bulletin*, 46(4):423–438, 2019b.

B. D. Warner and R. D. Stephens. Near-Earth Asteroid Lightcurve Analysis at the Center for Solar System Studies: 2019 July-September. *Minor Planet Bulletin*, 47(1):23–34, 2020a.

B. D. Warner and R. D. Stephens. Near-Earth Asteroid Lightcurve Analysis at the Center for Solar System Studies: 2020 April - June. *Minor Planet Bulletin*, 47(4):290–304, 2020b.

B. D. Warner, A. W. Harris, and P. Pravec. The asteroid lightcurve database. *Icarus*, 202(1):134–146, 2009.

A. Waszczak, C. K. Chang, E. O. Ofek, R. Laher, F. Masci, D. Levitan, J. Surace, Y. C. Cheng, W. H. Ip, et al. Asteroid Light Curves From the Palomar Transient Factory Survey: Rotation Periods and Phase Functions From Sparse Photometry. *The Astronomical Journal*, 150(3):75, 2015.

G. W. Wetherill and Clark R. Chapman. Asteroids and meteorites. In J. F. Kerridge and M. S. Matthews, editors, *Meteorites and the Early Solar System*, pages 35–67, 1988.

C. Wolf, C. A. Onken, L. C. Luvaul, B. P. Schmidt, M. S. Bessell, S. Chang, G. S. Da Costa, D. Mackey, T. Martin-Jones, et al. SkyMapper Southern Survey: First Data Release (DR1). *Publications of the Astronomical Society of Australia*, 35:e010, 2018.

P. A. Woudt, B. Warner, A. Gulbis, R. Coppejans, F.-J. Hambsch, A. P. Beardmore, P. A. Evans, J. P. Osborne, K. L. Page, G. A. Wynn, and K. van der Heyden. CC Sculptoris: A superhumping intermediate polar. *Monthly Notices of the Royal Astronomical Society*, 427(2):1004–1013, 2012.

S. Xu, R. P. Binzel, T. H. Burbine, and S. J. Bus. Small Main-Belt Asteroid Spectroscopic Survey: Initial Results. *Icarus*, 115(1):1 – 35, 1995.

D. K. Yeomans. *Near-Earth Objects: Finding Them Before They Find Us*. Princeton University Press, 2013.

B. Zellner, D. J. Tholen, and E. F. Tedesco. The eight-color asteroid survey: Results for 589 minor planets. *Icarus*, 61(3):355–416, 1985.

Appendices

A | Light curves of MBAs

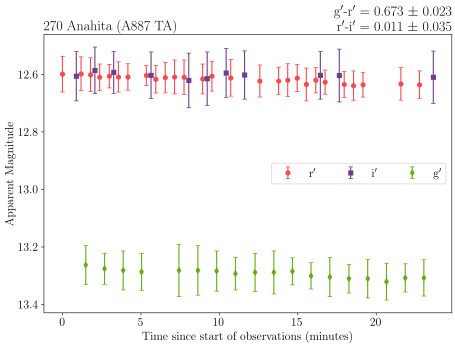

(a) 270 Anahita (A887 TA)

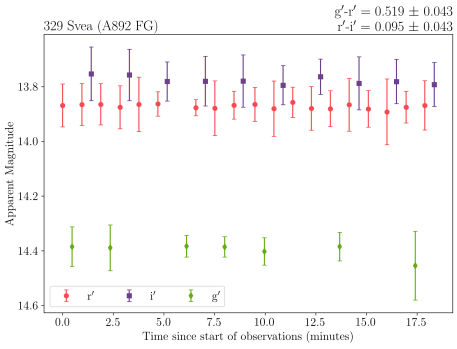

(b) 329 Svea (A892 FG)

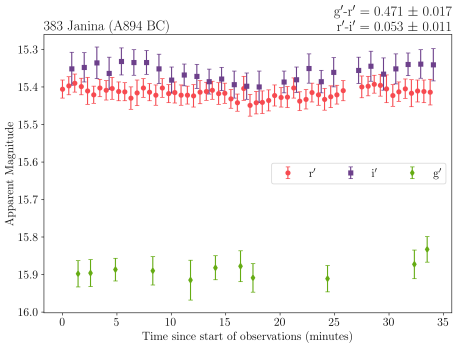

(c) 383 Janina (A894 BC)

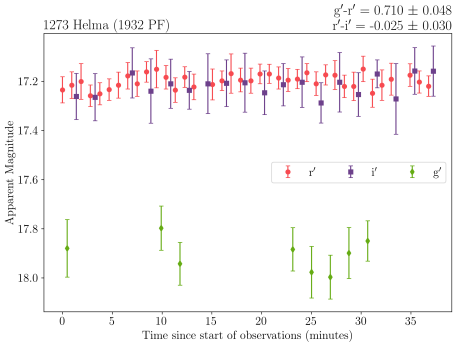

(d) 1273 Helma (1932 PF)

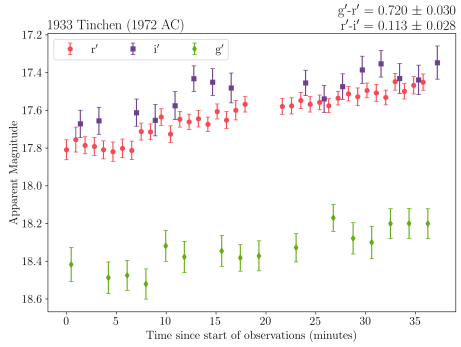

(e) 1933 Tinchen (1972 AC)

Figure A.1: The light curves (apparent magnitude as a function of time) of the remaining five MBAs that were not shown in Figure 3.1 and which were also used to verify the methodology and validate the results. The apparent magnitude is given as green diamonds for the g′-filter, red circles for the r′-filter and purple squares for the i′-filter. The g′−r′ and r′−i′ colours of each target are also shown in the top-right corner of each plot.

B | Light curves of NEAs

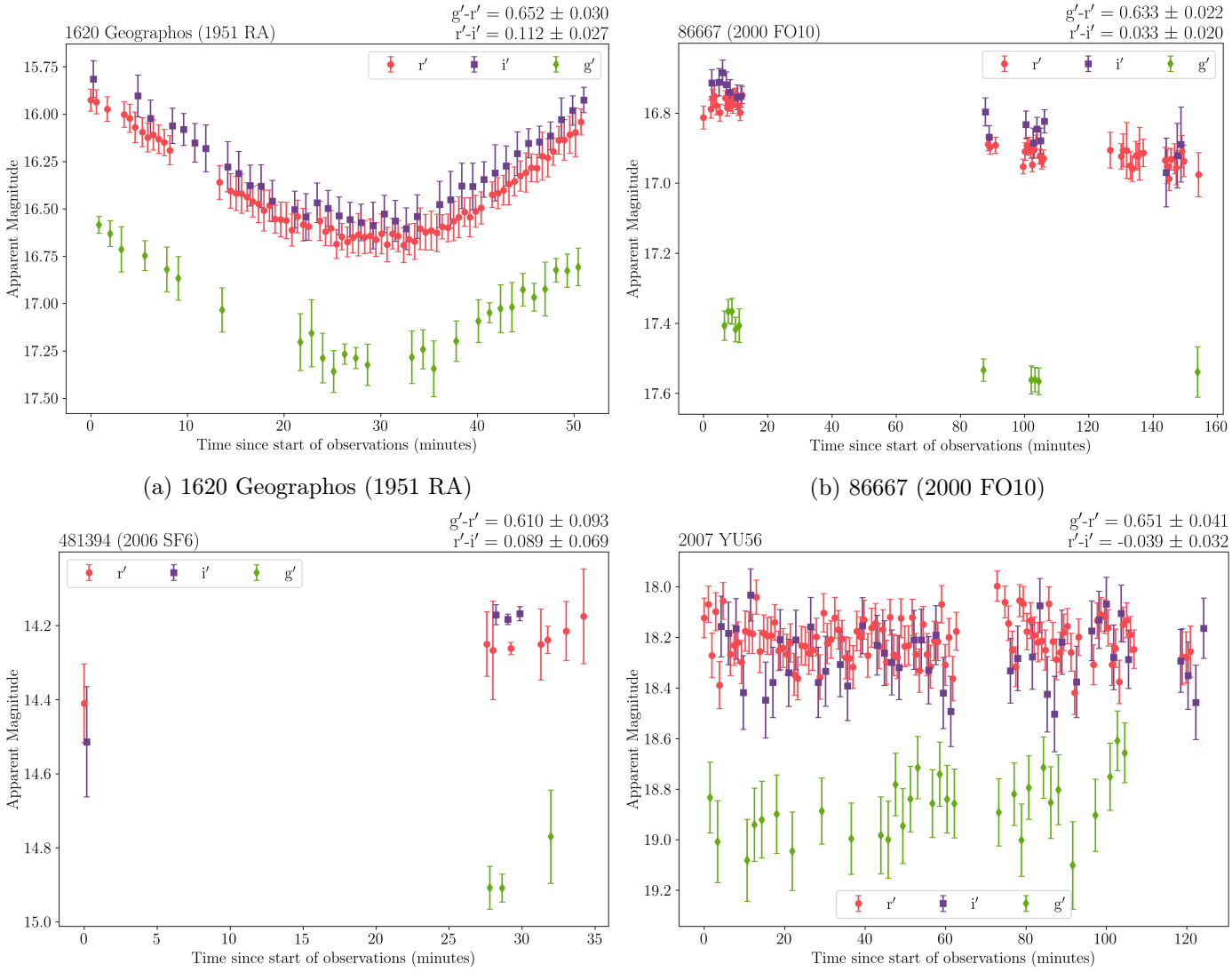

(a) 1620 Geographos (1951 RA)

(b) 86667 (2000 FO10)

(c) 481394 (2006 SF6)

(d) 2007 YU56

Figure B.1: The light curves (apparent magnitude as a function of time) of the remaining 16 NEAs that were not shown in Figure 3.2. The apparent magnitude is given as green diamonds for the g′-filter, red circles for the r′-filter and purple squares for the i′-filter. The g′−r′ and r′−i′ colours of each target are also shown in the top-right corner of each plot.

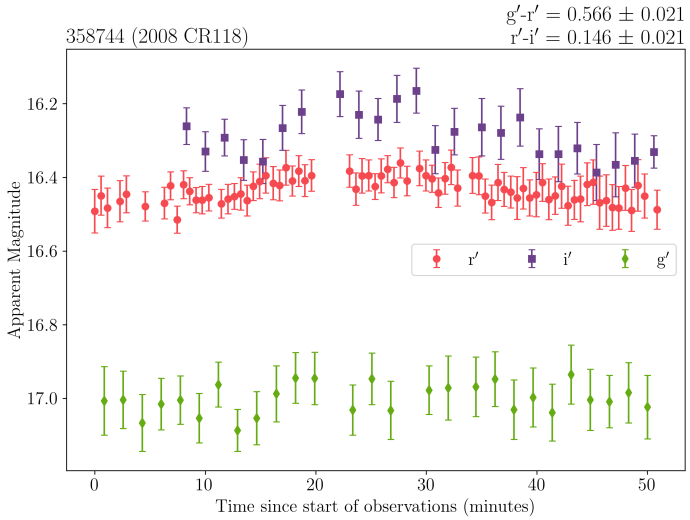

(e) 358744 (2008 CR118)

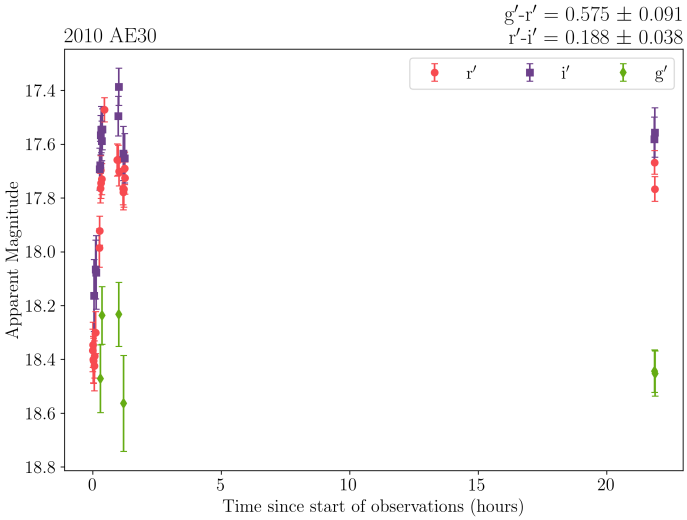

(f) 2010 AE30

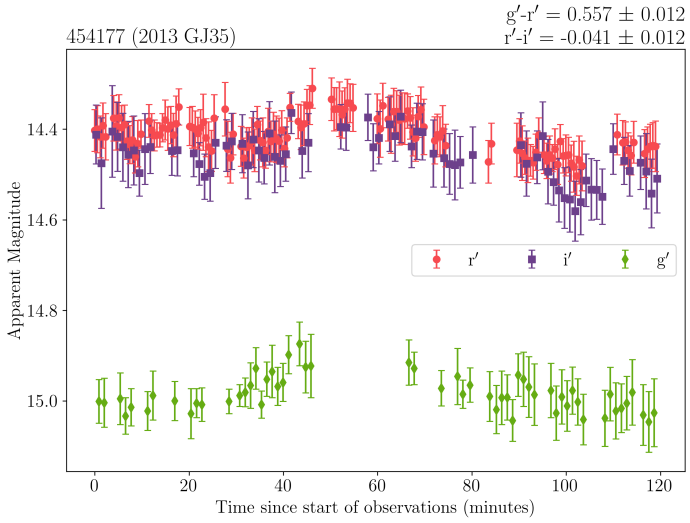

(g) 454177 (2013 GJ35)

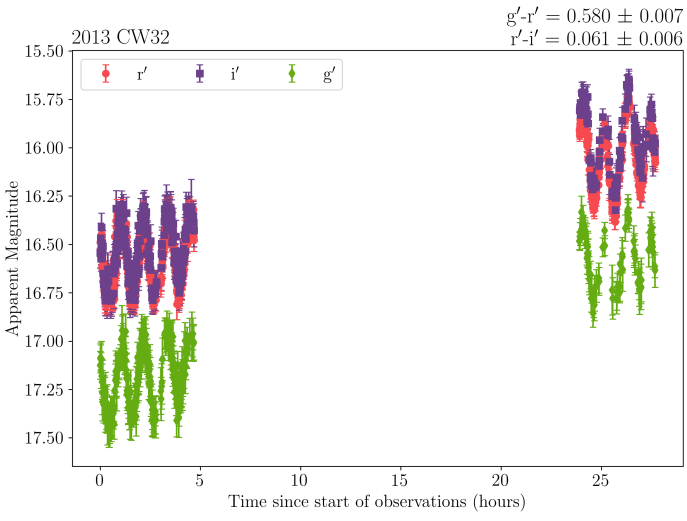

(h) 2013 CW32

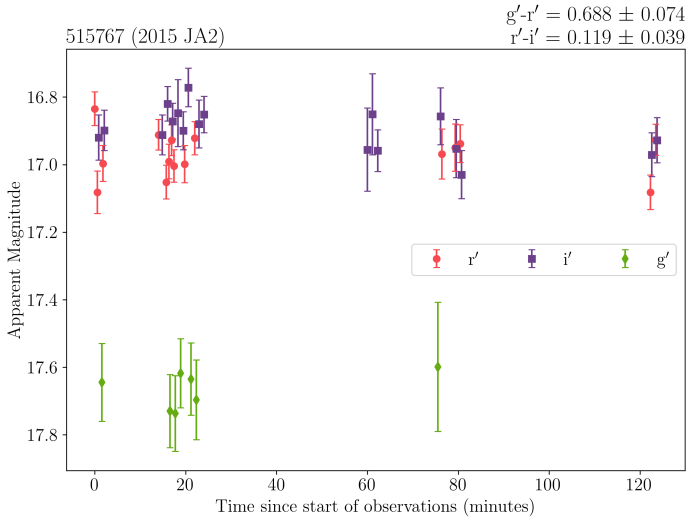

(i) 515767 (2015 JA2)

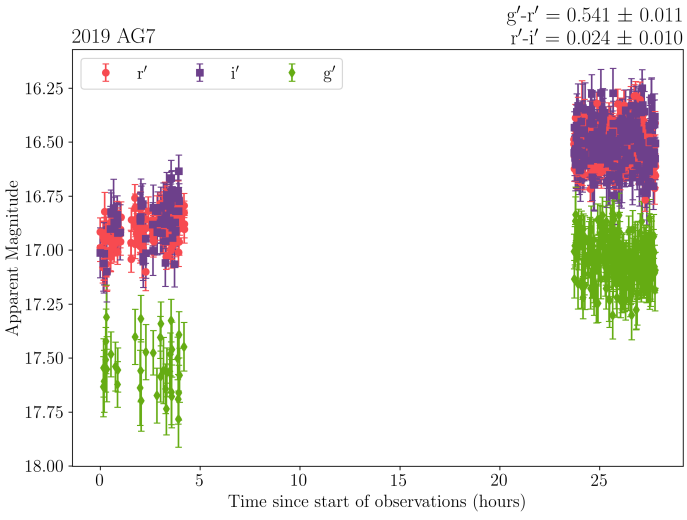

(j) 2019 AG7

Figure B.1: Continued.

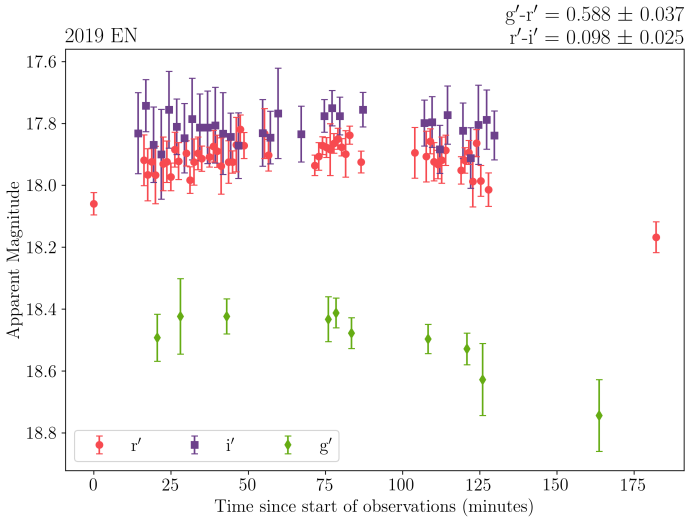

(k) 2019 EN

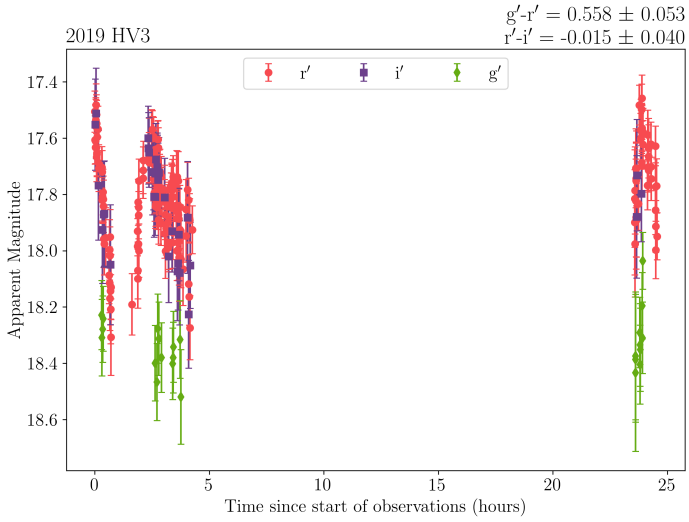

(l) 2019 HV3

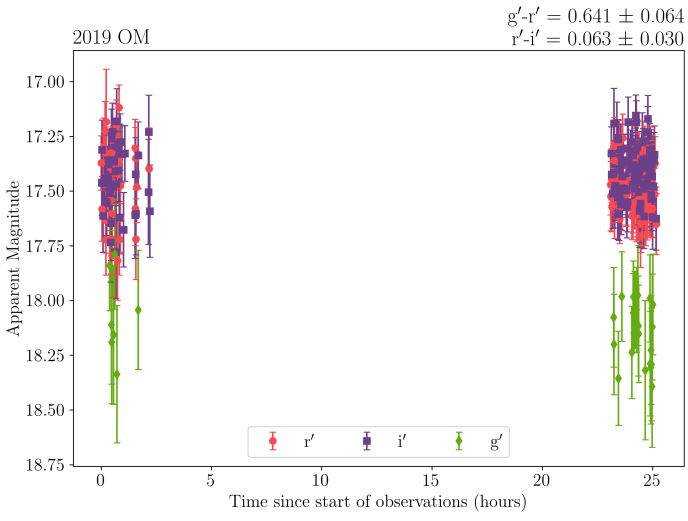

(m) 2019 OM

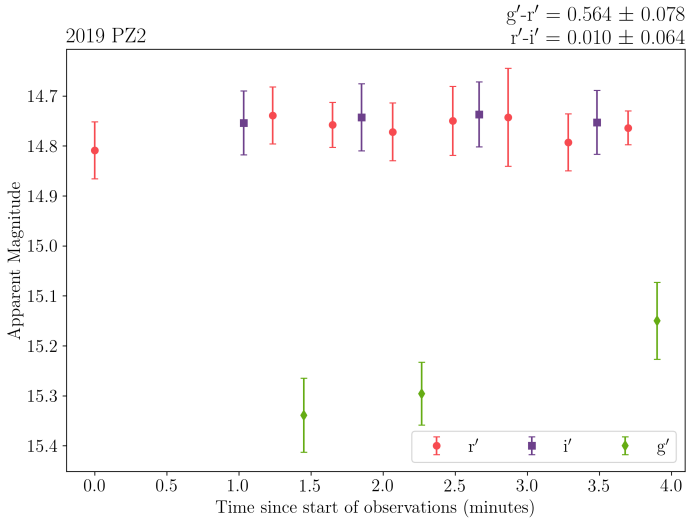

(n) 2019 PZ2

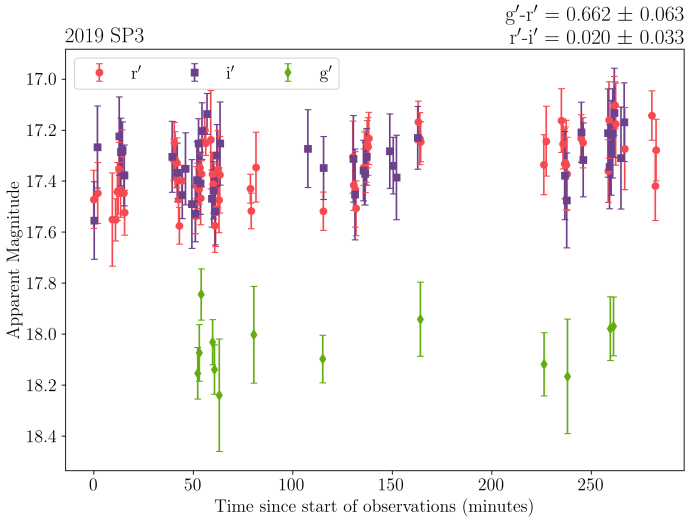

(o) 2019 SP3

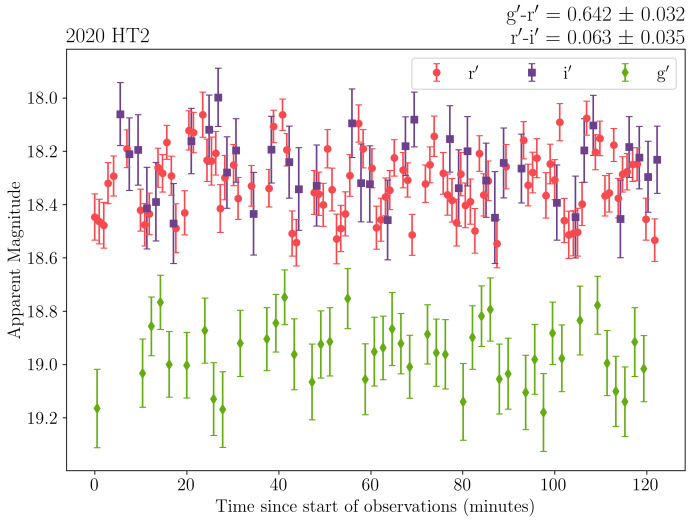

(p) 2020 HT2

Figure B.1: Continued.

C | Rotation periods

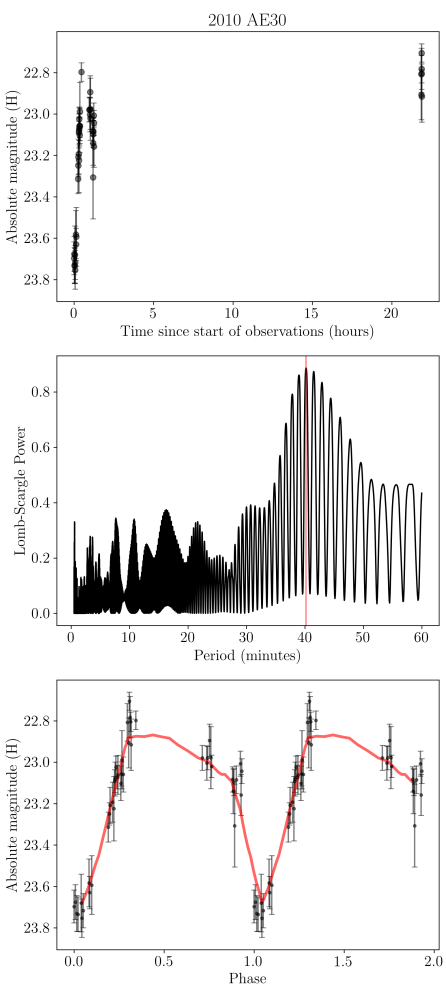

(a) 2010 AE30

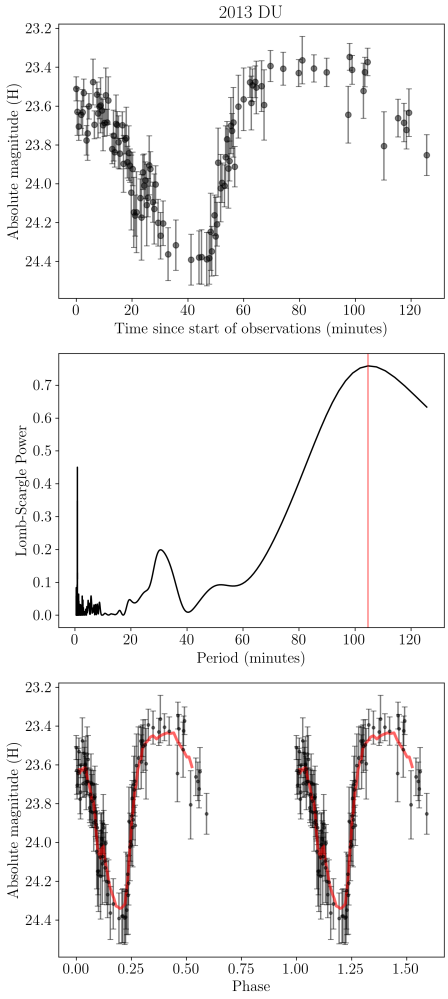

(b) 2013 DU

Figure C.1: Three plots are shown for the seven remaining targets that had a resolvable light curve period: (a) 2010 AE30, (b) 2013 DU, (c) 454177 (2013 GJ35), (d) 2019 CT4, (e) 2019 HV3, (f) 2019 SP3 and (g) 2020 BR10. Top: The light curve of the target, with the absolute magnitudes in the three filters (H_g, H_r and H_i) as a function of time. H_g and H_i were normalised to H_r by shifting them with the $g'-r'$ and $r'-i'$ colours, respectively, to form one densely-sampled light curve. Middle: The Lomb-Scargle periodogram of the light curve, with the highest peak indicated with a red line. Bottom: The phase folded light curve (magnitude as a function of the rotation phase), where the data were folded at the median rotation period given in Table 3.3. The red line is a running average with a window of 10 data points to guide the eye and which was also used to calculate the amplitude. The same plots are given in Figure 3.6 of Chapter 3 for the other two targets that had a resolvable light curve period.

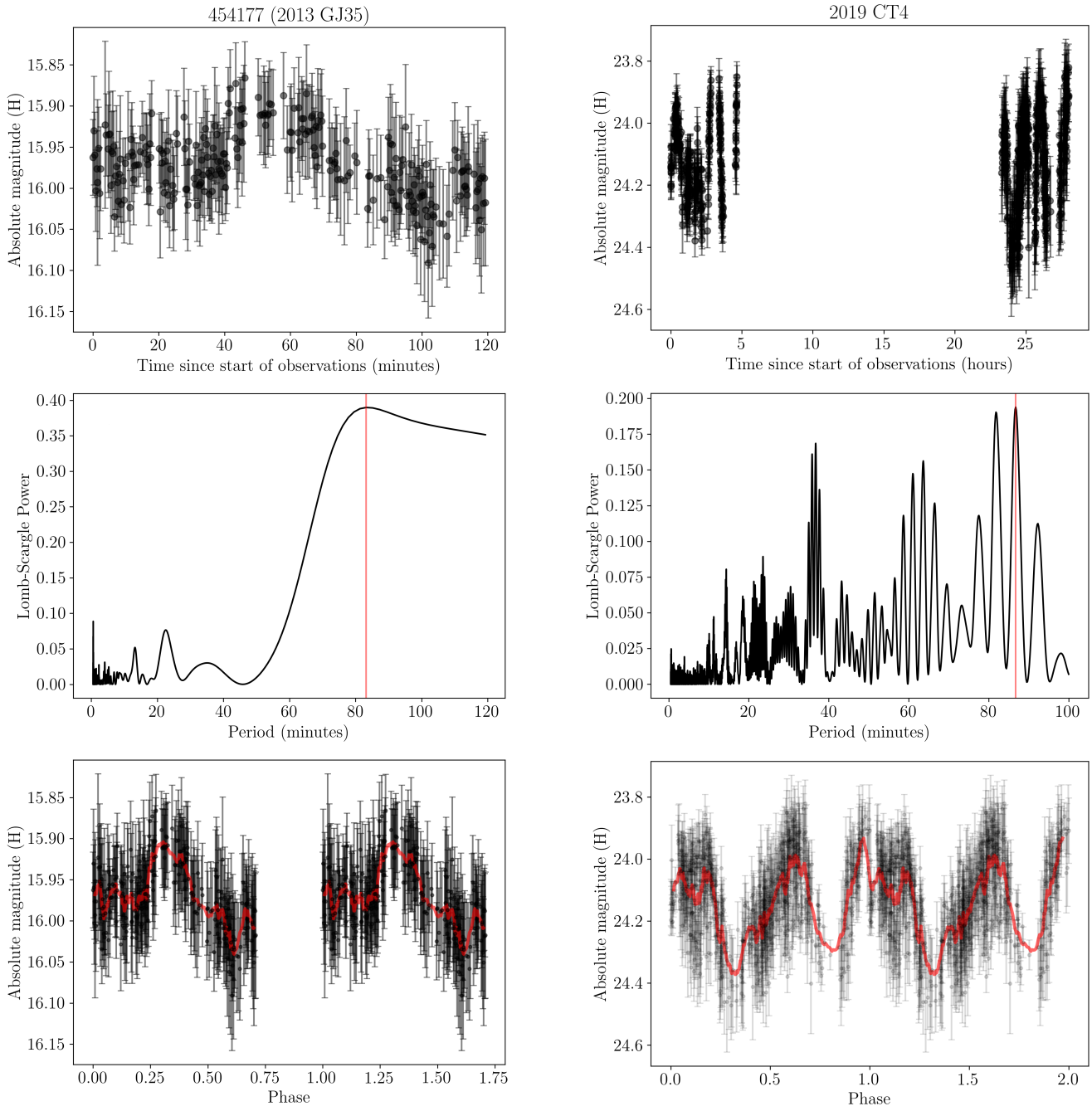

(c) 454177 (2013 GJ35)

(d) 2019 CT4

Figure C.1: Continued.

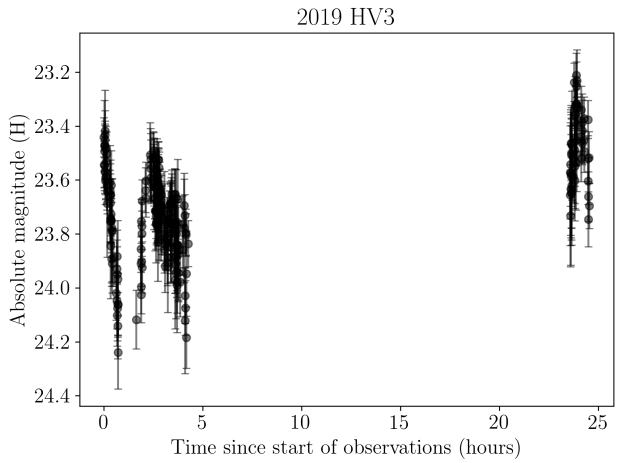

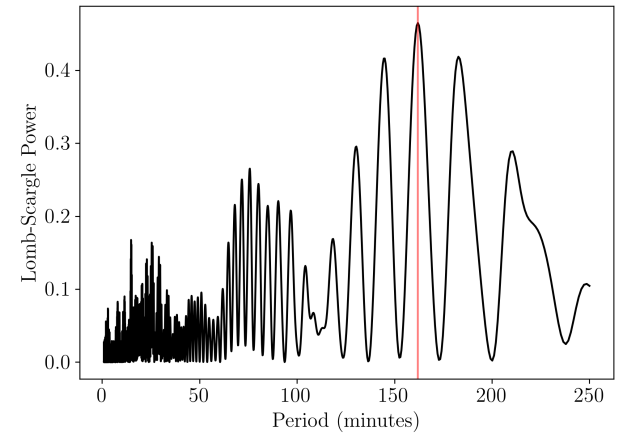

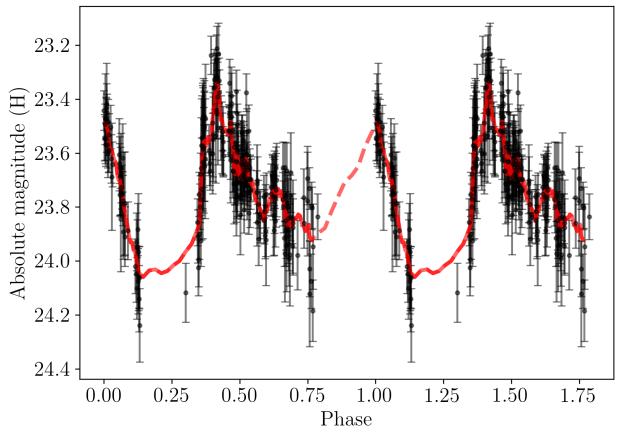

(e) 2019 HV3

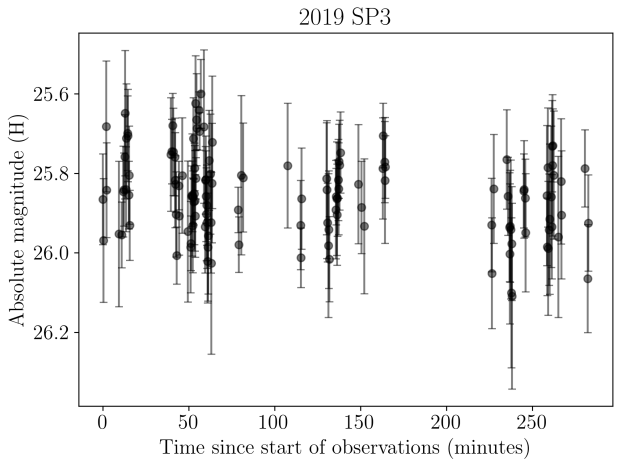

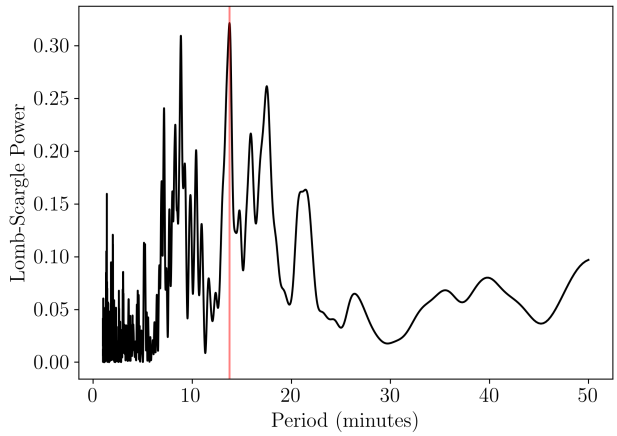

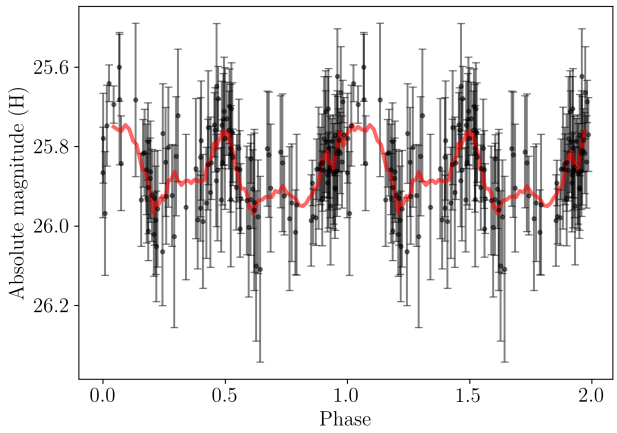

(f) 2019 SP3

Figure C.1: Continued.

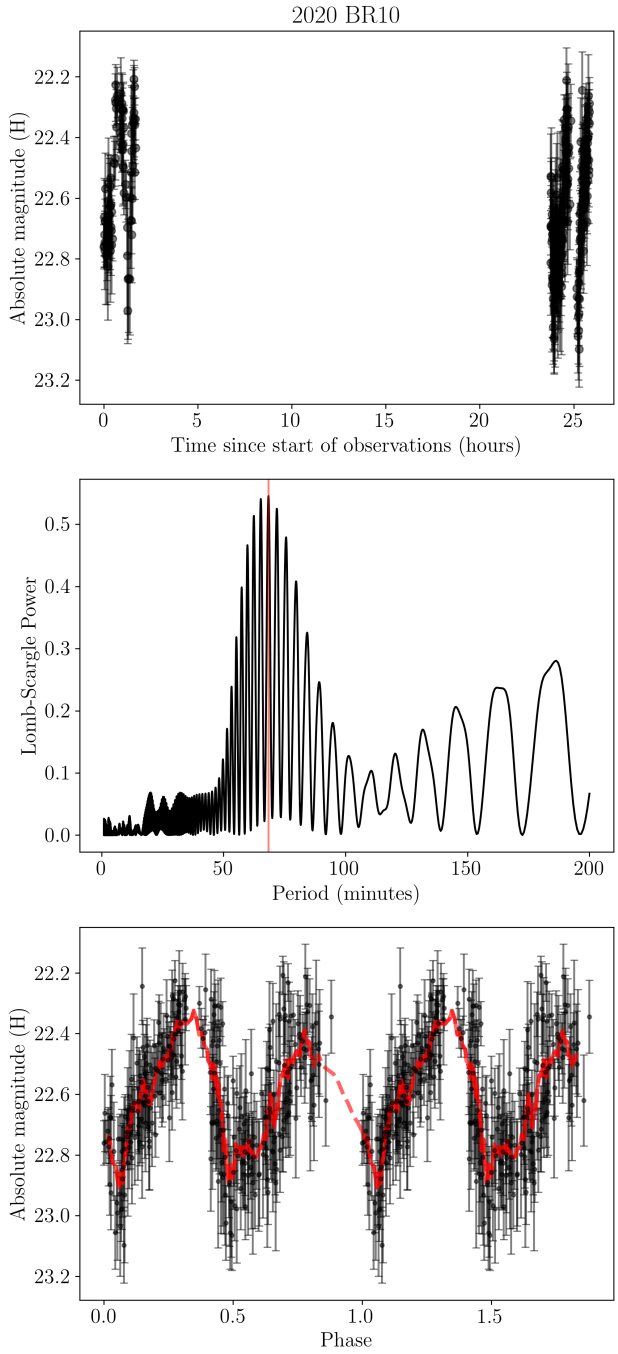

(g) 2020 BR10

Figure C.1: Continued.